Hard proton nucleus interactions and production of heavy flavours at HERA-*B*

DISSERTATION

zur Erlangung des akademischen Grades
doctor rerum naturalium
(dr. rer. nat.)
im Fach Physik

eingereicht an der
Mathematisch-Naturwissenschaftlichen Fakultät I
Humboldt-Universität zu Berlin

von
Herrn Dipl.-Phys. Alexandre Somov
geboren am 17.06.1969 in Moskau

Präsident der Humboldt-Universität zu Berlin:
Prof. Dr. J. Mlynek

Dekan der Mathematisch-Naturwissenschaftlichen Fakultät I:
Prof. Dr. B. Ronacher

Gutachter:

1. Prof. Dr. T. Lohse
2. Prof. Dr. H. Kolanoski
3. Prof. Dr. P. Buchholz

eingereicht am:	26. Juli 2000
Tag der mündlichen Prüfung:	29. November 2000

Abstract

A first attempt to measure the cross section of inclusive production of π^0 mesons decaying into two photons using the HERA-B detector in the spring of '99 configuration is presented. The π^0 cross section is determined using data from the inner part of the electromagnetic calorimeter for two types of target material, carbon and titanium, in the transverse momentum range of $2.75 < p_T < 5.0$ GeV/c and the center of mass rapidity range of $-0.05 < y_{C.M.} < 0.55$. From the data on C and Ti the nuclear dependence of π^0 production, parameterized as A^α, was extracted.

Various approaches for the luminosity determination at HERA-B are investigated. The average number of interactions in the target can be determined from the energy deposition in the electromagnetic calorimeter. This method provides a high accuracy in the luminosity determination.

The feasibility to study hadronic production of dileptons in the high-mass region at HERA-B is investigated with a Monte Carlo simulation. The predicted Υ mass resolution will allow the clear observation of the Υ mass peak above the background, and to separate the $\Upsilon(1S)$ and $\Upsilon(2S)$ states.

The possibility to perform an accurate measurement of Υ polarization is demonstrated. This measurement provides an excellent opportunity to test different mechanisms of heavy quarkonium production.

Keywords:
HERA-B experiment, luminosity determination, production of π^0 mesons, Υ polarization

Zusammenfassung

In dieser Arbeit wird ein erster Versuch vorgestellt, die inklusive Produktion von π^0 Mesonen durch ihren Zerfall in zwei Photonen mit dem HERA-B-Detektor in der Konfiguration des Frühjahrs ‘99 zu messen. Für die Bestimmung des Wirkungsquerschnittes der π^0-Produktion werden die Daten aus dem inneren Bereich des elektromagnetischen Kalorimeters verwendet. Die Messung wurde mit zwei verschiedene Target-Materialien, Kohlenstoff und Titan, durchgeführt und erstreckt sich über einen Bereich des Transversalimpulses von $2.75 < p_T < 5.0$ GeV/c und ein Rapiditätsintervall von $-0.05 < y_{C.M.} < 0.55$. Aus den mit Kohlenstoff und Titan gewonnenen Daten wird die Abhängigkeit der π^0-Produktion vom Target-Material, parametrisiert durch A^α, ermittelt.

Mehrere Methoden zur Bestimmung der Luminosität bei HERA-B werden untersucht. Es wird gezeigt, dass die durchschnittliche Anzahl von Wechselwirkungen mit Hilfe der im elektromagnetischen Kalorimeter deponierten Energie gemessen werden kann. Diese Methode bietet eine Möglichkeit zur Luminositätsbestimmung mit hoher Genauigkeit.

Die Durchführbarkeit, die hadronische Produktion von Leptonpaaren in hohen Massenbereichen mit HERA-B zu messen, wird in Monte-Carlo-Simulationen untersucht. Diese zeigen, dass die erwartete Massenauflösung eine Beobachtung des Υ-Signals über dem Untergrund und eine Trennung der Zustände $\Upsilon(1S)$ und $\Upsilon(2S)$ erlaubt.

Es wird gezeigt, dass eine genaue Messung der Υ-Polarisation möglich ist. Diese Messung bietet eine sehr gute Möglichkeit, die verschiedenen Mechanismen für die Produktion schwerer Quarkonium-Zustände zu testen.

Schlagwörter:
HERA-B-Experiment, Bestimmung der Luminosität, Production von π^0-Mesonen, Υ Polarisation

Acknowledgments

I want to place on record a deep sense of gratitude to my supervisor, Thomas Lohse, for his inspiring guidance, scholarly advice, and valuable suggestions while carrying out these investigations.

I am indebted to Rainer Mankel for constructive discussions and invaluable assistance during this work.

I am thankful for the hospitality of the DESY Zeuthen group, especially to Hermann Kolanoski and Michael Walter who created a pleasant and creative working atmosphere.

A lot of thanks to you, Avto. Your acrid comments and criticism always helped me to concentrate. I learned a lot working with you.

I am very much thankful to people from the target group, especially to Klaus Ehret and Youri Vassiliev, whom working with was really a pleasure.

It is my pleasure to acknowledge members of the HERA-B collaboration who assisted and encouraged me: Antonio Zoccoli, Avtandil Kharchilava, Dmitrii Emelianov, Gregor Wagner, Ivan Kisel, Jenny Ivarsson, Mauro Villa, Michael Medinnis, Olya Igonkina, Peter Kreuzer, Siegmund Nowak, Sergey Shuvalov, Ullrich Schwanke and many others.

I would like to thank Peter Buchholz for supporting the final stage of work on my thesis and giving me a chance to become acquaintance with the fruitful working atmosphere at Dortmund University.

I would like to thank Kendall Reeves, Mark Buchler, and Jenny Ivarsson, who read through all this stuff and have considerably improved my English.

I am grateful to the DFG, Germany, for the award of a Research Fellowship.

Last but not least I would like to thank my parents and brother, who have been very supportive during what must have been a trying period for them. Indeed, their pride in this endeavor has done much to make this thesis a complete one.

Contents

List of Figures

List of Tables

Introduction

The main goal of the HERA-B experiment is the study of CP-violation in the B-meson system. Being optimized for the detection of the CP asymmetry in the "Gold-Plated Channel" $B^0 \rightarrow J/\psi K^0_S$, the detector is well suited to perform the study of various processes which give an opportunity to probe perturbative quantum chromodynamics and study the mechanisms of heavy quarkonium production. The goals of this thesis are to demonstrate the HERA-B potential for the measurement of the inclusive π^0 production cross section and the possibility to perform accurate polarization measurements of the Υ mesons, both prime examples of QCD tests.

In the first part of Chapter 1, a brief description of the hard proton nucleus interaction is given. The discrepancies between theoretical calculations and available experimental data on the production of inclusive direct-photons and π^0 mesons are shown. The mechanisms of heavy quarkonium production are reviewed in the second part of this chapter. Special emphasis is put on the production and decay dynamics of Υ mesons. The results presented in this chapter are published in [8], where the degree of Υ polarization has been calculated for HERA-B energies. It is shown that Υ polarization provides an excellent opportunity to distinguish between different mechanisms of heavy quarkonium production.

The description of the HERA-B detector components, trigger system and detector simulation procedure is given in Chapter 2.

During the spring of 1999, HERA-B was in a stage of rapid detector assembly. In parallel to the detector commissioning, several runs with high p_T electron triggers have been performed with the spectrometer magnet switched off. In these runs the electromagnetic calorimeter (ECAL) has been used to select candidates for electrons and photons of high transverse momentum. The spring 1999 detector configuration and run conditions are described in the first section of Chapter 4. An attempt to measure the cross-section for the inclusive production of π^0 mesons with two photons in the final state is presented in the second section of Chapter 4. The aim of this study is to estimate the physics capabilities of the HERA-B detector and to evaluate the detector performance. The analysis is based on a data sample of about $1.5{\cdot}10^6$ events which have been acquired for two types of target material, carbon and titanium.

The physics interest in the cross section measurements makes the precise luminosity determination a task of vital importance. HERA-B is operating with several wires made of different materials inserted as target into the halo of the proton beam. Multiple interactions may appear per bunch crossing. Interaction rates have to be stabilized and equally distributed among wires. The precise determination of the interaction rate (i.e. the average number of interactions per bunch crossing) and the rate sharing among wires are very important for the luminosity calculation. In Chapter 3, the principle of the interaction rate measurement is discussed. Special emphasis is put on the description of the "Energy Sum" method which was proposed and is presently used for the interaction rate calibration. The feasibility to perform a cross check of the interaction rate calibration by counting the number of reconstructed tracks in the Vertex Detector System is demonstrated. Various approaches for the determination of the rate sharing among wires, in particular, the direct counting of primary vertices, are presented.

Chapter 5 contains the study of the observability of Υ resonances in the dilepton final state. The feasibility of an accurate polarization measurement is demonstrated. The expected statistical errors for the measurement of the polarization in one year of running of the HERA-B experiment are given.

Chapter 1

Theoretical models

1.1 Hard proton-nucleus interactions

1.1.1 Production mechanism

In the early days of the parton model [9, 10, 11] it was realized that the study of the constituents within nucleons is possible in deep inelastic interactions. Hadron-hadron collisions can provide important information about the constituent nature of nucleons. In the cases of hadron-hadron interactions when final state particles are produced with large transverse momenta the parton approach is applicable and QCD perturbation theory can be employed and tested. A hard scattering process between two hadrons is described as the result of an interaction between quarks and gluons which are the constituents of the colliding hadrons. A schematic diagram for large transverse momentum production of hadrons in the process $A + B \rightarrow h + X$ is shown in Fig. 1.1.

The interaction matrix element can be separated into *long* and *short*-distance parts. The hard-scattering process is characterized by the short-distance cross section $d\hat{\sigma}/dt$, which is entirely determined by the parton level and does not depend on the type of incoming hadron. The short-distance cross section can be calculated within perturbative quantum chromodynamics (pQCD) as a series in the running coupling constant α_S.

There are two nonperturbative components, or long distance parts, which can be parameterized by the parton distribution function (PDF) and the fragmentation function. The PDF $F(x_i, Q^2)$ is defined as the density of partons of type i within the hadron carrying a fraction x_i of the hadron

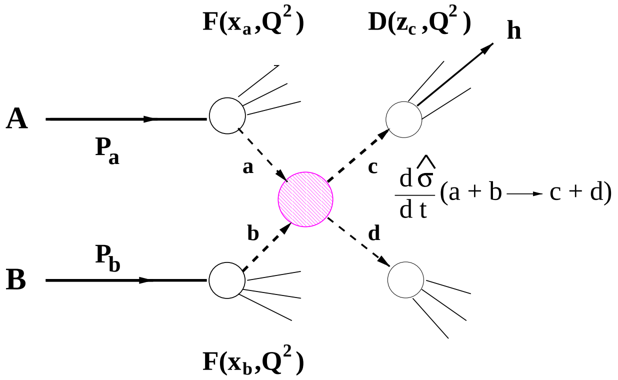

Figure 1.1: *Illustration of the inclusive process* $A+B \to h+X$ *resulting from the 2 to 2 hard scattering constituent subprocess* $a+b \to c+d$*.* $F(x_{a,b}, Q^2)$ *are the parton distribution functions.* $D(z_c, Q^2)$ *is the fragmentation function.*

momentum. PDFs are extracted from experiment; they can be measured, for example, in deep inelastic scattering or Drell-Yan pair production. The factorization ansatz assumes that PDFs characterize the nucleon structure and that they are universal, i.e. do not depend on the particular reaction.

The separation of matrix elements into two parts introduces the factorization scale Q^2, which distinguishes between the perturbative and nonperturbative pieces. A parton emitted with a squared transverse momentum larger than the value Q^2, is considered to be a part of the short distance cross section. On the contrary, a parton emitted with a squared momentum less then Q^2 is supposed to be part of the hadron structure and is absorbed into the parton distribution. Therefore, the hard part of the reaction involves squared momenta larger than Q^2 whereas all soft scales are hidden in the PDF.

The value of Q^2 is typically selected according to the experimental observable such as the transverse momentum of the outgoing particle, the mass of the pair of produced particles or the center of mass energy. Ideally the value of Q^2 has to be taken in order to minimize the dependence of the theoretical cross section on the factorization scale. Sometimes, factorization and renormalization scales are chosen to be equal. This scale usually is chosen to minimize the contribution from the higher order QCD terms (beyond the leading order), and thereby may lead to an accurate approximation.

In the final stage, the scattered colored partons are fragmented into the colorless hadrons by the process in which the $q\bar{q}$ pairs and gluons are created out of the vacuum to combine with the partons to form outgoing particles. This process is characterized by the fragmentation function $D(z_c, Q^2)$ which is defined as the probability density for hadrons h produced with a fraction z_c of the original longitudinal momentum of the parton. The fragmentation is associated with the scale Q_F^2 which is typically assumed to be a square of the transverse momentum of produced hadron. In the reactions with high p_T hadron production, the factorization scale can also be defined by the hadron momentum so that both scales can be chosen to be identical.

The cross section for a hadron scattering process produced by two hadrons with four momenta P_1 and P_2 can be written in the general form

$$\sigma(P_1, P_2) = \sum_{i,j} \int dx_1 dx_2 F_i(x_1, Q^2) F_j(x_2, Q^2) \hat{\sigma}_{i,j}(p_1, p_2, \mu^2/Q^2, \alpha_S(\mu^2)).$$

Here $\hat{\sigma}_{i,j}$ is the cross section for the scattering of partons of types i and j carrying the fractions of the hadron momentum $p_i = x_i P_i$. $F(x, Q^2)$ are the distribution functions of partons, defined at a factorization scale, Q^2, and μ^2 denotes the renormalization scale.

1.1.2 Inclusive production of direct-photons and mesons

A direct way to study parton-parton scattering is the investigation of large-p_T production of direct photons since the photon couples directly to the quark. In leading order (LO) real photons are produced by the quark-gluon Compton scattering or by quark antiquark annihilation subprocesses:

$$\begin{aligned} g + q &\rightarrow \gamma + q, \\ q + \bar{q} &\rightarrow \gamma + g. \end{aligned}$$

The presence of the gluon in the initial state in the Compton scattering subprocess provides an opportunity to determine the gluon distribution function in hadrons. This is especially important at large longitudinal momentum fractions ($x > 0.1$) where the gluon distribution function is not well constrained by deep-inelastic scattering and Drell-Yan data.

High p_T mesons appear as leading fragments of scattered partons in the hard interaction. At leading order in α_S the mesons can be produced via various $2 \rightarrow 2$ hard-scattering subprocesses:

$$\begin{aligned} q+q &\rightarrow q+q, & q+g &\rightarrow q+g, \\ q+\bar{q} &\rightarrow q+\bar{q}, & g+g &\rightarrow q+\bar{q}, \\ q+\bar{q} &\rightarrow g+g, & g+g &\rightarrow g+g. \end{aligned}$$

Therefore, the study of inclusive high p_T meson production allows us to test a different mix of the hard scattering processes and provides an insight into parton fragmentation.

1.1.3 Parton transverse momentum

The cross sections for inclusive direct photon and π^0 meson production have been measured in many experiments operating at different energies and with various beams and targets [1]. When the experimental results are compared with the theoretical calculations, which are performed to next-to-leading order, large deviations between data and theoretical predictions are observed for both direct-photon and inclusive π^0 cross sections. The origin of these disagreements is suspected to be due to initial state soft-gluon radiation. The emission of multiple soft gluons by the partons prior to the hard-scattering process can generate a significant mean transverse momentum $\langle k_T \rangle$ of the parton with respect to the incoming proton.

Evidence for large values of $\langle k_T \rangle$ has long been observed in measurements of dimuons, diphotons and dijets. The average transverse momentum of the pairs $\langle p_T \rangle_{pair}$ measured for various center of mass energies is shown in Fig. 1.2. The value of $\langle k_T \rangle$ per parton can be estimated as $\sim \langle p_T \rangle_{pair}/\sqrt{2}$. As can be seen, the $\langle k_T \rangle$ is increasing with the center of mass energy from about 1 GeV/c at fixed target energies up to $\sim$ 4 GeV/c at the Tevatron collider. These values of $\langle k_T \rangle$ can not be explained by primordial parton transverse momentum related to the confinement of the parton inside the finite size of the hadron. In this case, the expected value of $\langle k_T \rangle$ would be only 0.3-0.5 GeV/c. Similar effects of k_T smearing are expected in all hard-scattering processes, particularly in inclusive production of direct photons and mesons.

The precise calculation of the soft gluon contributions is difficult to perform analytically. This effect is often treated in the Monte Carlo framework. Usually parton motions are smeared in the transverse direction by a Gaussian distribution with an average transverse momentum $\langle k_T \rangle$. This smearing modifies the shape of the inclusive p_T spectrum and also increases the production cross section. As an example, direct-photon and π^0 meson cross sections measured by the E706 and WA70 experiments at $\sqrt{s}$ = 38.8 and

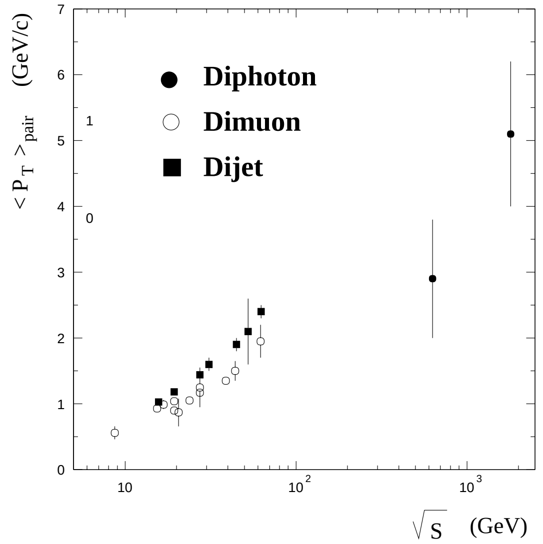

Figure 1.2: *Mean transverse momentum $\langle p_T \rangle$ of pairs of muons, photons and jets produced in hadronic collisions as a function of $\sqrt{s}$[1].*

$\sqrt{s} = 23.0$ GeV respectively are presented in Fig. 1.3. The cross sections are compared to k_T-enhanced next-to-leading order (NLO) calculations[1]. As can be seen, in the case of the Fermilab E706 experiment both direct photon and π^0 meson cross sections lie above the NLO calculations ($\langle k_T \rangle = 0$ GeV/c). The cross sections are found to be in a good agreement with Monte Carlo simulations for $\langle k_T \rangle \sim 1.4$ GeV/c. For the WA70 experiment, the π^0 cross section matches the Monte Carlo simulation for $\langle k_T \rangle \sim 1.1$ GeV/c, while the photon data do not seem to require k_T corrections. A detailed overview of the k_T effects and its application to the available direct-photon and π^0 data can be found in [1].

From everything mentioned above, it is clear that more complete theoretical calculations are needed to understand the nature of k_T smearing effects. A new generation of inclusive direct-photon and π^0 meson measurements are necessary to test the theoretical predictions and improve our knowledge of the gluon distribution function and the parton fragmentation mechanism.

---

[1] Monte Carlo programs that include k_T smearing are available for the LO calculations. The effect of k_T smearing is extended to the NLO calculations by multiplying the NLO cross section by the leading order k_T enhancement.

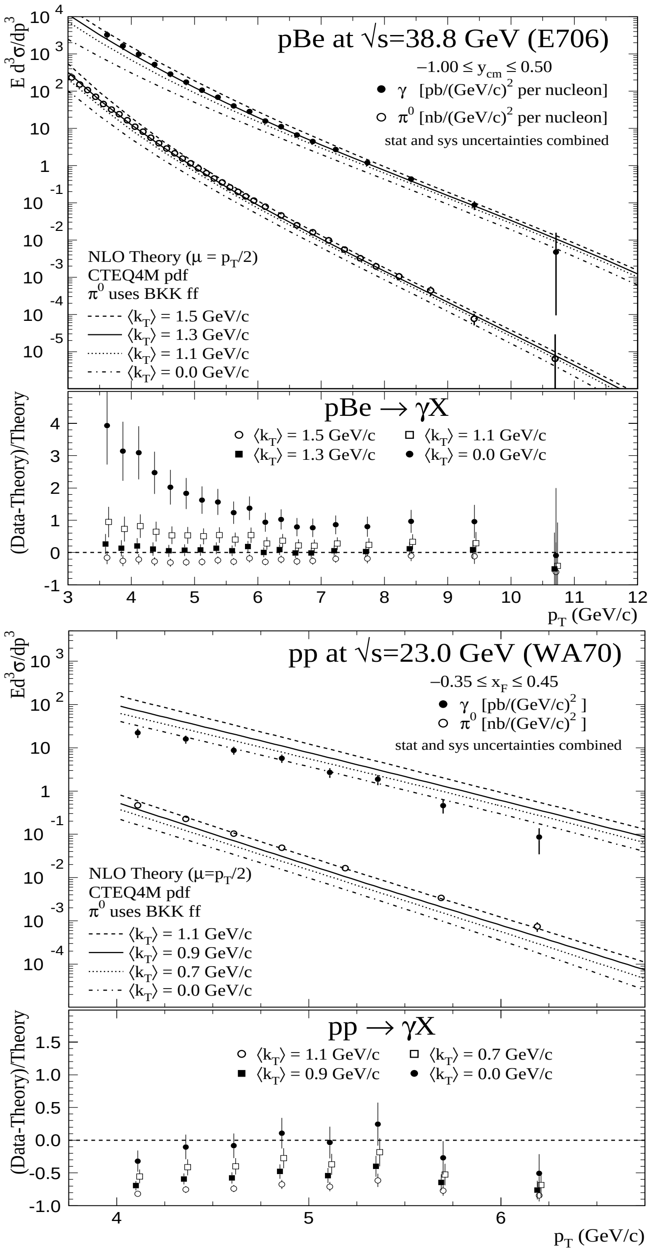

Figure 1.3: *The photon and* π^0 *meson cross sections measured by E706(top) and WA70(bottom) experiments at* $\sqrt{s} = 38.8$ *and* $\sqrt{s} = 23.0$ *GeV respectively. The cross sections are compared to* k_T*-enhanced next-to-leading order calculations. The quantity (Data-Theory)/Theory for direct-photons for various* k_T *values is presented for both experiments [1].*

1.2 Bottomonium production at HERA-B

1.2.1 The mechanisms of heavy quarkonium production

Heavy quarkonia, i.e. bound states of heavy quark-antiquark pairs, are thought to provide a useful testing ground for perturbative quantum chromodynamics. The reason being that the charm and bottom quark masses provide a large scale which makes the short distance behavior calculable using a perturbative approach whereas the nonpeturbative contributions can be factorized into a wave function. In the color singlet model (CSM), pQCD is used to calculate the production of a $Q\bar{Q}$ pair in a color singlet state [12, 13]. This forms a quarkonium state with the same angular momentum quantum numbers ${}^{2S+1}L_J$ by coupling to the nonperturbative wave functions at the origin. It is worth mentioning that the CSM provides a recipe for calculating not only the inclusive production rate for a quarkonium state, but also its inclusive decay rate into light hadrons and its decay rate into leptons or photons. For example, the formula for the decay rate of the J/ψ into light hadrons in the CSM can be written as

$$\Gamma(J/\psi) \;\simeq\; \tilde{\Gamma}(c\bar{c}({}^3S_1))\,|R_{J/\psi}(0)|^2, \tag{1.1}$$

where $\tilde{\Gamma}$ is proportional to the annihilation rate of a $c\bar{c}$ pair in the state $({}^3S_1)$. The last factor in Eq.(1.1) is the square of the wave function at the origin, which gives the probability for the $c\bar{c}$ pair in the J/ψ to be close enough to annihilate. Therefore, the wave function at the origin can be extracted from the quarkonium decay rate into the light hadrons or from the leptonic decay width and used in the calculations of inclusive production cross sections.

Recently, several discrepancies between color singlet model predictions and experimental data were observed. For example, the CSM gives definite predictions for the ratios $\sigma(H(c\bar{c}))/\sigma(J/\psi)$ of inclusive production cross sections for quarkonium states H to J/ψ. The ratio of χ_c production cross sections and the J/ψ production cross section is expected to be rather different for the two states χ_{c1} and χ_{c2}. There is no diagram in the framework of the CSM for χ_{c1} production in lowest order of the QCD coupling constant. Nevertheless, no strong variations in the ratios $\sigma(H(c\bar{c}))/\sigma(J/\psi)$ have been observed experimentally. The color singlet model also predicts large transverse polarizations of J/ψ mesons at fixed target energies, $\sqrt{s} \simeq 30 - 60$ GeV, however, no polarization for this state has been observed so far.

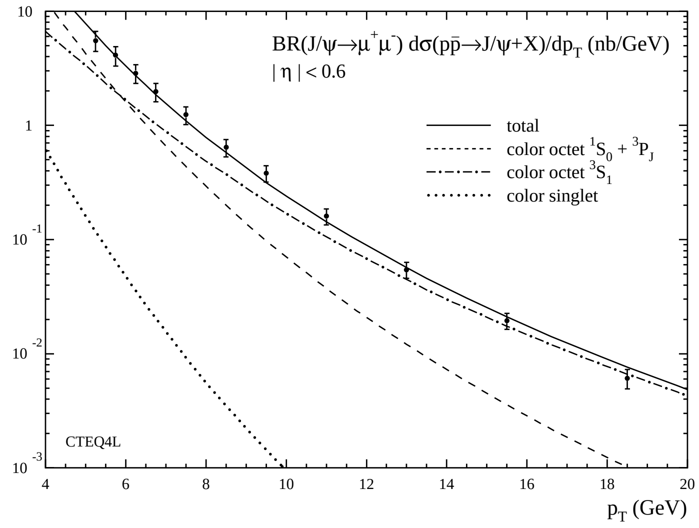

Figure 1.4: *Comparison of theoretical prediction to the CDF data of direct* J/ψ *production.*

The most dramatic discrepancy between the CSM prediction and experimental data was discovered, when the CDF collaboration measured the production cross sections for charmonium states at the Tevatron $p\bar{p}$ collider [14, 15]. They found that the cross sections for the direct production of J/ψ and ψ' mesons at large transverse momentum were larger than the predictions of the color singlet model by about a factor of 30. This can be seen in Fig. 1.4, taken from reference [16].

In the last few years, a rigorous theoretical framework for treating heavy quarkonium production and decays has been developed. The factorization approach (FA) based on non-relativistic QCD (NRQCD) is used as a reliable starting point to study heavy quarkonium production and decay processes [17]. Because the heavy quarkonium is a non-relativistic bound state, there are several different scales which play an important role in quarkonium physics. In general one can define four such scales:

- m_Q, the mass of the heavy quark, which defines the scale of heavy quark pair production and annihilation processes.
- $m_Q v$, the typical momentum of heavy constituents in a quarkonium, connected to the size of the bound system via the Heisenberg uncertainty relation. Here, v is the typical velocity of heavy quarks in the non-relativistic bound state.

- $m_Q v^2$, the kinetic energy of heavy quarks in the bound state, which defines the scale of interaction in the hadronization phase.
- Λ_{QCD}, the scale of nonperturbative effects associated with light quarks and gluons.

For heavy quark masses, the velocity v is small enough (for the charmonium system $v^2 \simeq 0.3$ and for the bottomonium system $v^2 \simeq 0.1$) so that the scales are well separated:

$$m_Q v^2 < m_Q v < m_Q. \tag{1.2}$$

According to the factorization approach the inclusive production cross section for a quarkonium state H in the process

$$A + B \rightarrow H + X \tag{1.3}$$

can be factorized as:

$$\sigma(A + B \rightarrow H) = \sum_n \frac{F_n}{m_Q^{d_n - 4}} \langle 0 | \mathcal{O}_n^H | 0 \rangle, \tag{1.4}$$

where the short-distance coefficients, F_n, are associated with the production of a heavy quark pair in the color and angular momentum state n. This part of the cross section involves only momenta of at least the order of the heavy quark mass, m_Q, and can be calculated perturbatively. The factors of $m_Q^{d_n-4}$ are introduced so as to make the coefficients F_n dimensionless. In the production process two distinct scales are introduced: the heavy quark-antiquark pair production process occurs at small distances, $1/m_Q$, and is factorized from the hadronization phase which takes place at large distances, $1/(m_Q v^2)$. The vacuum matrix elements of NRQCD operators, $\langle 0 | \mathcal{O}_n^H | 0 \rangle$, describe the evolution of the quark-antiquark state n into the final hadronic state H [17]. These long distance matrix elements cannot be calculated perturbatively, but their relative importance in powers of velocity v can be estimated using the NRQCD velocity scaling rules [18]. The important feature of this formalism is that the cross section of heavy quarkonium production can be organized as a double expansion in powers of v and $\alpha_S(m_Q)$. At higher order in v the factorization approach implies that the quark-antiquark color octet intermediate states are allowed to contribute to heavy quarkonium production and decay processes.

Unlike the color singlet long distance matrix elements, where each matrix element is connected with the subsequent non-relativistic wave function at the origin, the color octet long distance matrix elements are unknown and have to be extracted from the experimental data. The NRQCD factorization approach implies universality, i.e. the values of long distance matrix elements extracted from different experimental data sets must be the same. However, due to the presently rather large theoretical uncertainties [19, 20, 21, 22, 16] and the unknown size of higher twist process contributions [23] the existing experimental data is insufficient to check the factorization approach universality.

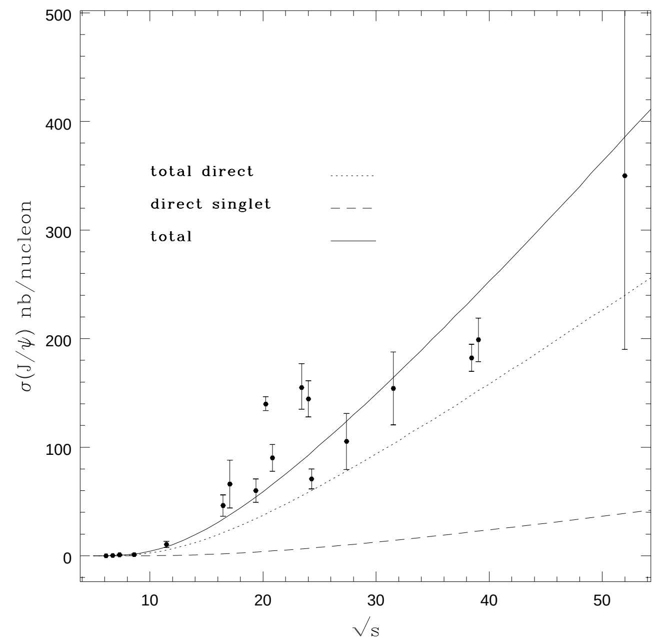

Figure 1.5: *J/ψ production cross sections in proton-nucleon collisions for $x_F > 0$. The dashed line is the direct J/ψ production rate in the CSM and the dotted line includes the contribution from the color-octet process. The total cross section (solid line) includes radiative feed-down from the χ_{cJ} and ψ' states [2, 3].*

The data on direct J/ψ and ψ' production at large transverse momenta at the Tevatron indicates that the color octet contribution dominates. The S state charmonia are produced through the gluon fragmentation into the ${}^3S_1^{(8)}$ octet state [24, 25, 26]. Recent investigations have shown that the contribution of color octet states to the charmonium (Fig. 1.5) and bottomonium (Fig. 1.6) production cross sections is very important at fixed target energies, $\sqrt{s} \simeq 30 - 60$ GeV, and reduces existing discrepancies between experimental data and predictions of the color singlet model [27, 28, 29].

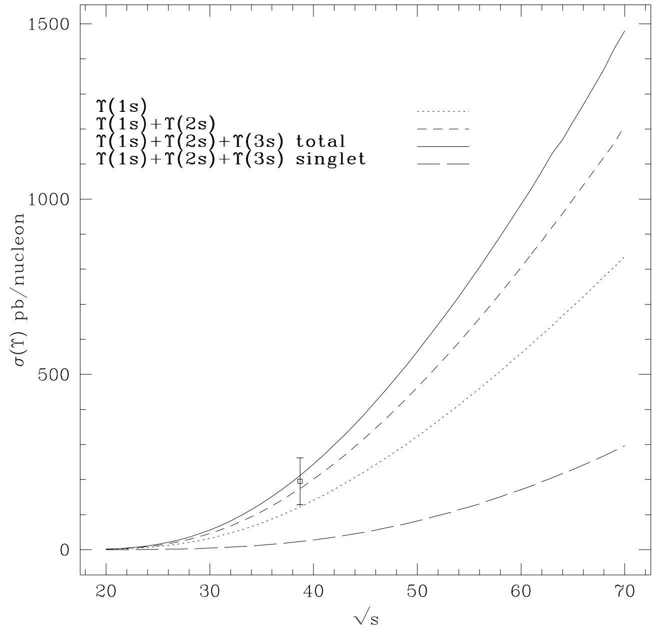

Figure 1.6: *Total* $\Upsilon(nS)$ *production cross sections (for* $x_F > 0$*), consecutively summed over* n*. The data point refers to the sum of* $n = 1, 2, 3$ *[2, 3].*

However, some experimental data contradicts the color octet model (COM) predictions. In particular, theoretical predictions disagree with measurements of the polarization of J/ψ and ψ' particles produced at fixed target energies [2, 3]. The color octet model predicts a too low relative yield of the χ_{c1} state compared to the χ_{c2} [2, 3]. One possible solution of these discrepancies was proposed in [23], suggesting that higher twist processes, when more than one parton from projectile or target participate in the reaction, might give a significant contribution to low p_T production of J/ψ and χ_{c1} states. Problems exist also in charmonium photoproduction at HERA. The color octet contribution overestimates the inelastic J/ψ photoproduction cross section at large values of z ($z = E_{J/\psi}/E_\gamma$ in the laboratory frame)

[30].

Other models which can describe the heavy flavour production are the color evaporation model (CEM) and the related 'soft color interaction' (SCI) model [31]. In these models the cross section for a specific quarkonium state is given as a fraction of the inclusive $Q\bar{Q}$ production cross section integrated up to the open heavy flavour production, D meson pairs in the case of charmonium production and B meson pairs for the bottomonium. For example, in the CEM, the formula for the inclusive cross section for producing a J/ψ is conventionally written in the form

$$\sigma(J/\psi) \quad = \quad \hat{\sigma}(c\bar{c} : 4m_c^2 < s < 4m_D^2)F_{J/\psi}, \tag{1.5}$$

where $\hat{\sigma}$ is the cross section for producing a $c\bar{c}$ pair with invariant mass below the $D\bar{D}$ threshold. The cross section is summed over all color and spin states of the heavy quark pair. The factor $F_{J/\psi}$ is a phenomenological parameter that defines the fraction of $c\bar{c}$ pairs that form a J/ψ meson. The production fraction is assumed to be universal in the CEM, while in the SCI model it depends somewhat on the partonic state and the possible string configurations. In both models the color and spin quantum numbers of the intermediate $Q\bar{Q}$ state are irrelevant, and gluon emission during the hadronization is assumed to be unsuppressed. This leads to unpolarized quarkonium production. Multiple soft gluon exchange in the hadronization phase destroys the initial polarization of the heavy quark pair and, therefore, the heavy quarkonium is produced unpolarized [32, 33].

It is worth mentioning that predictions for the polarization of direct ψ's produced at large p_T at the Tevatron are free from theoretical uncertainties connected with higher twist effects and corresponding measurements will provide an excellent possibility to test the NRQCD factorization approach. Recently such a measurement was done at the CDF experiment. In Fig. 1.7 the experimental data and theoretical predictions are shown for J/ψ polarization at the Tevatron [4]. The data includes the sum of both contributions, direct J/ψ production and production from P-wave quark-antiquark states. As can be seen from Fig. 1.7, the data is rather different from the theoretical predictions at large p_T.

At the same time it is not excluded that the mass of the charm quark is not large enough to apply the NRQCD factorization approach to charmonium production and decay processes. Due to the rather large value of v^2, about 0.3 for the charmonium system, the Fock states at higher order in v^2 may give

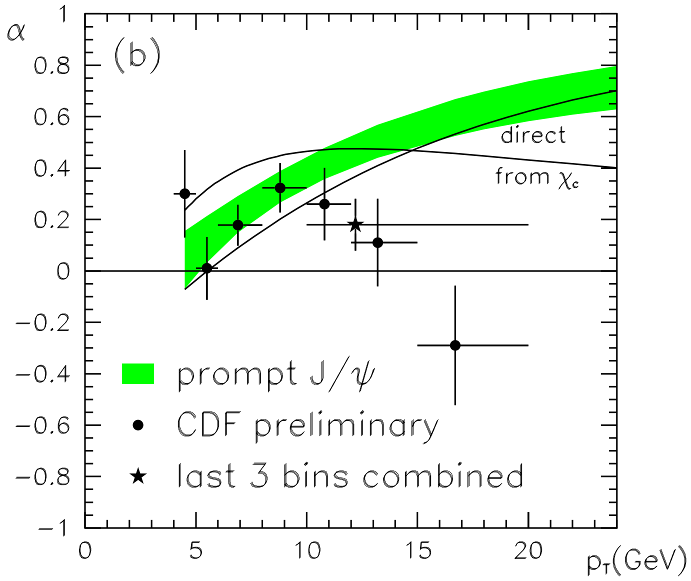

Figure 1.7: *Comparison of the theoretical prediction to the CDF data of direct* J/ψ *production. The polarization parameter* η *is shown as a function of the transverse momentum of the* J/ψ *meson [4].*

the essential contribution and can then not be neglected. In contrast, the NRQCD factorization approach predictions for the bottomonium system are more reliable, since the expansion parameter v^2 is much smaller (around 0.1), than for the charmonium system. Higher twist processes are also expected to be suppressed by $\Lambda/m_b \simeq 0.1$ (compared with $\Lambda/m_c \simeq 0.3$). Also the QCD coupling constant is smaller for bottomonium system. Therefore, the characteristics of Υ meson production are more appropriate for a stringent test of the NRQCD factorization approach.

1.2.2 Υ production subprocesses and matrix elements.

At leading order in α_S the different S- and P-wave quark-antiquark states can be produced in the following $2 \to 2$ and $2 \to 3$ subprocesses:

- gluon-gluon fusion

$$\begin{array}{ll} gg \to \ {}^1S_0^{(8)} \ , & gg \to \ {}^1S_0^{(8)} + g \ , \\ gg \to \ {}^3S_1^{(1,8)} + g \ , & \\ gg \to \ {}^3P_{0,2}^{(1,8)} \ , & gg \to \ {}^3P_J^{(1,8)} + g \ ; \end{array}$$

- gluon-quark scattering

$$\begin{array}{ll} gq \to {}^3S_1^{(8)} + q \ , & gq \to {}^1S_0^{(8)} + q \ , \\ gq \to {}^3P_J^{(1,8)} + q \ ; & \end{array}$$

- quark-antiquark annihilation

$$\begin{array}{ll} q\bar{q} \to {}^3S_1^{(8)} \ , & q\bar{q} \to {}^1S_0^{(8)} + g \ , \\ q\bar{q} \to {}^3P_J^{(1,8)} + g \ ; & \end{array}$$

where the superscripts (1,8) denote the color singlet and color octet states, respectively.

The total cross section of Υ production is given by the sum of the direct production cross section and the cross section of χ_{bJ} states decaying through Υ mesons,

$$\begin{aligned} \sigma_\Upsilon &= \sigma(\Upsilon)_{dir} + \sum_{J=0,1,2} Br(\chi_{bJ} \to \Upsilon X)\sigma(\chi_{bJ}) \\ &\quad + \sum_{n=2,3} Br(\Upsilon(n) \to \Upsilon X)\sigma(\Upsilon(n)). \end{aligned} \tag{1.6}$$

The production of each quarkonium state receives contributions from both color octet and color singlet states (with the exception of the ${}^1S_0^{(1)}$ state). The relative velocity for the bottomonium system is small, $v^2 \simeq 0.1$, and hence the production cross sections can be calculated with only the leading order color octet contribution taken into account.

In Table 1.1 the color singlet and color octet long distance matrix elements for the production of χ_{bJ} states are presented. The values for the matrix elements are taken from [2, 3]. The color singlet matrix elements are computed from the wave functions of the Buchmüller-Tye potential tabulated in [34]. The matrix elements $\langle 0|\mathcal{O}_8^H({}^3S_1)|0\rangle$ are obtained from fit to Tevatron data [25, 26]. For the $3P$ bottomonium state the value of this matrix element is obtained by extrapolation from the $1P$ and $2P$ states [2, 3].

The characteristics of Υ production at fixed target energies ($\sqrt{s} \simeq 40$ GeV) differ from charmonium production, as was mentioned in [2, 3]. The $\Upsilon(nS)$ states are mainly produced in the quark-antiquark annihilation subprocess through decays of P wave states of bottomonia. Unlike J/ψ production, the color octet contribution to the Υ production in the gluon-gluon fusion subprocesses is less important. At leading order in perturbative QCD

Matrix Elements	$\chi_{b0}(1P)$	$\chi_{b0}(2P)$	$\chi_{b0}(3P)$
$\langle\mathcal{O}_1^H(^3P_0)\rangle/m_b^2$	$8.5\cdot 10^{-2}$	$9.9\cdot 10^{-2}$	0.11
$\langle\mathcal{O}_8^H(^3S_1)\rangle$	0.42	0.32	0.25

Table 1.1: *Matrix elements for the production of P-wave bottomonia in units of GeV^3.*

only $^1S_0^{(8)}$ and $^3P_J^{(8)}$ color octet states contribute to Υ production. They are suppressed as v^4 and v^2 compared to Υ production through color singlet $^3S_1$ and ^3P_J states, respectively. Hence, due to the small value of $v^2 \simeq 0.1$, it turns out that in the gluon-gluon fusion subprocesses the main contribution to Υ production comes from the color singlet states. The P-wave bottomonium states are produced at lowest order in the pQCD expansion, $\mathcal{O}(\alpha_S^2)$. The subprocesses for direct production of S states ($\Upsilon(nS)$) are suppressed by the factor α_S/π compared to those for χ_{b0} and χ_{b2} production. Consequently, the indirect Υ meson fraction from the decay of χ_{bJ} states is expected to be large in the gluon-gluon fusion subprocesses.

The main contribution to P-wave bottomonia production comes from the quark-antiquark annihilation subprocess. First of all, the leading color octet and color singlet contributions to P-wave quarkonium production scale equally in v^2, $O(v^5)$, the subleading corrections being only of the order $O(v^9)$. At leading order in v^2, one color octet state contributes to the production of χ_{bJ} states, namely $^3S_1^{(8)}$. Moreover, at leading order in pQCD this state is only produced in the quark-antiquark annihilation subprocesses. The values of the matrix elements $\langle 0|\mathcal{O}_8^{\chi_{bJ}}(^3S_1)|0\rangle$ are large compared to the color singlet matrix elements for the corresponding P states, connected to the quarkonium wave functions derivatives at the origin (see Table 1.1) [25, 26]. Furthermore, at fixed target energies the $q\bar{q}$ luminosity effectively increases compared to the gg luminosity due to the large mass of the $(b\bar{b})$ system.

The Υ production cross sections in gluon-gluon fusion and quark-antiquark annihilation subprocesses at different energies are presented in Table 1.2. The contributions of all leading order subprocesses in double expansion in powers of v and α_S are taken into account. The b-quark mass of $m_b = 4.9$ GeV is chosen as in ref. [25, 26] in order to extract the values of color octet long distance parameters from the Tevatron data for the Υ production. The cross sections are calculated using the GRV LO parton distribution functions [35] evaluated at the factorization scale $Q^2 = 4m_b^2$. The long distance color octet parameters for direct $\Upsilon(nS)$ production are taken from [2, 3]. For the decays of $\chi_{bJ}(3n)$ states[2] to $\Upsilon(3S)$ the same branching ratios are assumed as for the corresponding $n = 2$ states [2, 3].

$\sqrt{s}$	40 GeV	200 GeV	300 GeV	500 GeV
$gg \to \Upsilon g$	0.002 nb	0.9 nb	2.44 nb	6.8 nb
$gg \to {}^1S_0^{(8)}, {}^3P_{0,2}^{(8)} \to \Upsilon$	0.01 nb	1.9 nb	4.3 nb	11.4 nb
$gg \to \chi_{b2} \to \Upsilon\gamma$	0.016 nb	2.7 nb	6.3 nb	16.4 nb
$q\bar{q} \to {}^3S_1^{(8)} \to \chi_{b2} \to \Upsilon\gamma$	0.24 nb	6.82 nb	10.6 nb	17.8 nb

Table 1.2: *Cross sections for Υ production through different subprocesses at HERA-B and RHIC energies in the NRQCD FA.*

All cross sections depend strongly on the mass of b-quark and the factorization scale, but the relative yield of Υ from different subprocesses is practically insensitive to these parameters.

From Table 1.2 one finds that the direct Υ production cross section for the adopted values of the long distance parameters is more than one order of magnitude smaller than the total cross section. Even in the color singlet model the Υ mesons are mainly produced through decays of χ_{bJ} states. On the other hand, the color octet contribution seems to be dominant in χ_{bJ} production. The main contribution comes from the ${}^3S_1^{(8)}$ state, produced in quark-antiquark annihilation.

As was already shown in [2, 3], the color octet contribution reduces the large discrepancy between the CSM prediction for the total Υ production cross section and experimental data at fixed target energies, $\sqrt{s} \simeq 30 \div 60$ GeV, [36, 37, 38, 39]. Nevertheless, there remain large uncertainties due to contradictory experimental results. The cross sections obtained by integration of x_F distributions for $\Upsilon(1S)$ production presented in [36] and [37, 38] are three and four times smaller, respectively, than the central value quoted in [39], 270 pb/nucleon. In addition, the theoretical value of the cross section strongly depends on the assumed mass of the b-quark. It is therefore impossible to extract the color octet matrix elements with reasonable accuracy from the fixed target bottomonia production data.

---

[2] As was suggested in [2, 3], the large yield of the $\Upsilon(3S)$ state at the E772 experiment at FNAL [36] could be explained by assuming the unobserved $\chi_{bJ}(3P)$ states to lie below the open beauty threshold.

1.2.3 Υ polarization

As already mentioned in [2, 3], the measurement of the cross section for direct and indirect production of Υ's would provide crucial information about the color octet mechanism, e.g., new constraints on the long distance color octet parameters would emerge. Such a measurement requires the reconstruction of χ_{bJ} states in the $\Upsilon + \gamma$ decay mode which is not a trivial task at fixed target experiments due to the small transverse momentum of the emitted photon.

Another possibility to check the NRQCD factorization approach is to measure the Υ polarization. In $H \to \ell^+\ell^-$ decays the polarization of a S-state quarkonium is determined by the polar-angle distribution of its decay leptons with respect to the beam direction in the meson rest frame. Integrating over the azimuthal angle the distribution has the form

$$\frac{d\sigma}{d\cos\theta} \propto 1 + \eta\cos^2\theta, \tag{1.7}$$

where θ is the angle between the positively charged lepton, ℓ^+ ($\ell =$ e, μ), and the beam axis in the quarkonium rest frame. The parameter η in the angular distribution can be related to ξ, the fraction of longitudinally polarized Υ mesons:

$$\eta = \frac{1-3\xi}{1+\xi} = \begin{cases} 1 \text{ for } \xi = 0 \\ -1 \text{ for } \xi = 1 \end{cases} \tag{1.8}$$

The calculation of J/ψ and ψ' polarization at fixed target energies and Tevatron collider energies was performed in [16, 2, 3, 40, 41]. The most general method to calculate the cross sections for heavy quarkonium production with definite polarization within the NRQCD factorization approach was proposed by Braaten and Chen [42]. Tang and Vänttinen used the covariant projection method to calculate cross sections for polarized J/ψ and ψ' production [41]. The $\chi_{bJ}(nP)$ states are produced in quark-antiquark annihilation through only one color octet state, ${}^3S_1^{(8)}$. For this particular case both methods give the same result. As an example we present the formulae derived in [41] to obtain the polarization of $\Upsilon(nS)$ states produced in the cascade $q\bar{q} \to {}^3S_1^{(8)} \to \chi_{bJ} \to \Upsilon(nS) + \gamma$:

$$\begin{aligned} &\sigma(q\bar{q} \to b\bar{b}({}^3S_1^{(8)}) \to \chi_{b1} + g \to \Upsilon + \gamma + g) \\ &= \frac{16\pi^3\alpha_S^2}{27M^5}\delta(1 - M^2/\hat{s})Br(\chi_{1b} \to \Upsilon + \gamma)\langle\mathcal{O}_8^{\chi_{b1}}({}^3S_1)\rangle\frac{3-\delta_{\lambda 0}}{8}, \end{aligned} \tag{1.9}$$

$$\sigma(q\bar{q} \to b\bar{b}(^3S_1^{(8)}) \to \chi_{b2} + g \to \Upsilon + \gamma + g)$$
$$= \frac{16\pi^3\alpha_S^2}{27M^5}\delta(1 - M^2/\hat{s})Br(\chi_{b2} \to \Upsilon + \gamma)\langle \mathcal{O}_8^{\chi_{b2}}(^3S_1)\rangle \frac{47 - 21\delta_{\lambda 0}}{120} \quad (1.10)$$

The scalar χ_{b0} state yields unpolarized bottomonium S-wave states. From Eq.(1.9) and Eq.(1.10) the values of η for χ_{b1} and χ_{b2} intermediate states are found to be 0.2 and 0.29 respectively.

Taking into account all transitions from $\chi_{bJ}(1P)$ and $\chi_{bJ}(2P)$ states to $\Upsilon(1S)$ the polarization parameter in quark-antiquark annihilation subprocesses is found to be

$$\eta \simeq 0.24. \quad (1.11)$$

In general the fraction ξ depends on the mechanism and the particular subprocess of Υ production. Channels with dominating contributions to Υ hadroproduction at small p_T (with the corresponding values of η and ξ) are:

i) Direct Υ production through the color singlet state, $gg \to \Upsilon g$; the ratio of longitudinally and transversely polarized quarkonia $\xi = 0.23$ and $\eta \simeq 0.25$ [23].

ii) Direct Υ production through color octet states, $gg \to ^1S_0^{(8)}, ^3P_{0,2}^{(8)} \to \Upsilon$. For the intermediate scalar state, $^1S_0^{(8)}$, $\xi = 1/3$ and $\eta = 0$; for intermediate P-wave states $\xi = 1/7$ and $\eta = 0.75$ [2, 3].

iii) Υ production from χ_{b2} decay, the CSM, $gg \to \chi_{b2} \to \Upsilon\gamma$. The χ_{b2} at small p_T are produced with spin projection $J_z = \pm 2$ and Υ coming from χ_{b2} is purely transversely polarized, $\eta = 1$ [23].

iv) Υ production from χ_{b2} decay through the color octet state, $q\bar{q} \to ^3S_1^{(8)} \to \chi_{b2} \to \Upsilon\gamma$. In this case Υ mesons are produced with sizeable transverse polarization, $\eta = 0.24$ [8].

In Table 1.3 the expected polarizations of Υ mesons are presented at different energies. These values are obtained by weighting all subprocesses with their partial cross sections, see Table 1.2.

$\sqrt{s}$	40 GeV	200 GeV	300 GeV	500 GeV
η	$0.28 \div 0.31$	$0.37 \div 0.49$	$0.4 \div 0.54$	$0.43 \div 0.59$

Table 1.3: *Parameter η for the Υ polarization at different energies.*

The range of the parameter η in Table 1.3 is due to different possible choices of the parameters for the long distance color octet matrix elements, $\langle 0|\mathcal{O}_8^{J/\psi}(^1S_0)|0\rangle$

and $\langle 0|\mathcal{O}_8^{J/\psi}(^3P_0)|0\rangle$. Only a combination of these matrix elements can be obtained from fits to the experimental data [2, 3]. The lower bound of η corresponds to the extreme assumption that only the octet S-state contributes, the upper bound is derived from the other extreme in which the octet P-wave state dominates. The results for Υ polarization are in agreement with the predictions of Ref. [43]. This result remains practically unchanged if the contribution from $\chi_{bJ}(3P)$ states with the same branching ratios as for the corresponding $2P$ states is added.

The value $\eta \simeq 0.24$ as derived above represents a lower theoretical limit for the polarization since it is calculated taking into account only the quark-antiquark annihilation subprocesses. In gluon-gluon fusion subprocesses the polarization of Υ mesons is larger due to the dominant contribution from χ_{b2} decays which yield pure transverse polarization [23]. For the values of octet long distance parameters (Table 1.1) the size of the polarization is $\eta \simeq 0.3$ and hence also exceeds 0.24. However, large uncertainties in color octet long distance parameters for P-wave bottomonia do not allow to compute the relative importance of the various subprocesses, so that the lower bound of $\eta = 0.24$ remains as the only firm prediction.

In contrast to charmonium production the higher twist effects for the bottomonium system are expected to be small. In particular, the higher twist effect suggested in [23], when more than one parton from the projectile or target is involved in the production of heavy quarkonium states, is expected to be negligible for Υ production. Two partons should be within a transverse distance of $O(1/m_Q)$ in order to interact with the other parton and to produce a heavy quark-antiquark bound state. Consequently, such a higher twist process is suppressed by a factor of $O(\Lambda_{QCD}^2/m_Q^2)$ [23]. To explain the discrepancies between the CSM predictions and the measured relative production rate χ_{c1}/χ_{c2} it has been suggested that the above suppression can be compensated by a kinematical enhancement [23]. Thus the χ_{c1} production cross section in the higher twist process is expected to be at the same level as the χ_{c2} production cross section from gluon-gluon fusion subprocesses. In bottomonium production such a mechanism is suppressed by the mass of the bottom quark $O(\Lambda_{QCD}^2/m_b^2)$, i.e. the corresponding cross section should be one order of magnitude smaller than in the charmonium case. The effect of the kinematical enhancement is also smaller due to the larger mass of the bottomonium system. Moreover, as can be seen from Table 1.2, the gluon-gluon fusion subprocesses give small contributions to Υ production at fixed target energies compared to J/ψ production. Therefore, the measurement of Υ polarization at fixed target energies will allow one to distinguish between the NRQCD approach and the CEM, which predicts unpolarized production of all bottomonium states.

The photon recoil in the decays of χ_{bJ} states and any intrinsic momentum of colliding partons are neglected in this consideration. The intrinsic k_T-smearing reduces the polarization parameter in the case of J/ψ production about 15% [23]. Both effects are expected to be small for the Υ production due to the large mass of the botomonium system.

1.2.4 χ_{b2} production.

In Ref. [44] it is shown that the contribution of color octet states is negligible in P-wave charmonium production and hence the measurement of the χ_{c2} polarization can not provide valuable information about the color octet mechanism. The reasons are that the color octet matrix elements parameterizing the transition ${}^3S_1^{(8)} \to \chi_{cJ}$ are small compared to the corresponding color singlet matrix elements of P-wave states [2, 3, 25, 26]. As has been mentioned above, in leading order of α_S, the ${}^3S_1^{(8)}$ octet state is produced in the quark-antiquark annihilation subprocess. For charmonium production the quark-antiquark luminosity is small compared to the gluon-gluon luminosity at fixed target energies ($\sqrt{s} \simeq 40$ GeV). Consequently, the contribution of color octet states to χ_{c2} production is negligible and the photon angular distribution parameter η_γ in Eq.(1.12) is determined only by the color singlet mechanism, i.e. $\eta_\gamma \simeq 1$.

The situation for bottomonium states is more subtle. The main contribution in the production of the bottomonium P-wave states is expected from the ${}^3S_1^{(8)}$ color octet state [2, 3]. Therefore, as a test of different mechanisms of heavy quarkonium production, the polarized production of χ_{b2}-states can be considered. The photon angular distribution (after integration over the azimuthal angle was carried out) can be expressed in the χ_J-meson rest frame as

$$\frac{d\sigma}{d\cos\theta} \propto 1 + \eta_\gamma \cos^2\theta, \qquad (1.12)$$

where θ is the polar angle relative to the hadron beam axis.

Angular distributions for the decay of χ_{b2} and χ_{c2} states with the different spin projections, J_z, have been calculated in Ref. [45]:

$$\begin{aligned} W(J_z = \pm 2) &\propto 1 + \cos^2\theta, \\ W(J_z = \pm 1) &\propto 1 - \frac{1}{3}\cos^2\theta, \\ W(J_z = \ \ 0) &\propto 1 - \frac{3}{5}\cos^2\theta. \end{aligned} \tag{1.13}$$

The polarization of χ_{b2} can be calculated using the spin orientation of the intermediate quark-antiquark pair. The color singlet ${}^3P_2$ state produced in the gluon-gluon fusion subprocess has the spin projection $J_z = \pm 2$ [23]. Therefore, the color singlet model predicts the value of η_γ to be equal to unity.

In the color octet model, in leading order of v only one color octet state, ${}^3S_1^{(8)}$, contributes to χ_2 production. In lowest order of α_S, the state ${}^3S_1^{(8)}$ can only be produced in the quark-antiquark annihilation subprocess[3].

In Table 1.4 the χ_{b2} production cross sections in gluon-gluon fusion and quark-antiquark annihilation subprocesses at different energies are presented.

$\sqrt{s}$	40 GeV	200 GeV	300 GeV	500 GeV
$\sigma(q\bar{q} \to {}^3S_1^{(8)} \to \chi_{b2})$	0.4 nb	11 nb	18 nb	30 nb
$\sigma(gg \to \chi_{b2})$	0.033 nb	5.5 nb	13 nb	33 nb

Table 1.4: *Cross sections for χ_{b2} production through different subprocesses at HERA-B and RHIC energies in NRQCD FA.*

As is obvious from Table 1.4, the main contribution to the χ_{b2} production cross section at HERA-B energy ($\sqrt{s} \simeq 40$ GeV) is due to the quark-antiquark annihilation subprocess. In Ref. [44] angular distributions from Eq.(1.13) have been averaged according to the relative yield of χ_{b2} with the corresponding spin projections J_z. This gives the value of the angular distribution parameter $\eta_\gamma \simeq 0.44$. The relative contribution of the gluon-gluon fusion subprocess in the total cross section increases for RHIC collider energies and correspondingly increases the value of η_γ. At $\sqrt{s} = 500$ GeV the value of η_γ is found to be 0.7 (Ref. [44]).

---

[3] As was mentioned in [25, 26], the process $gg \to {}^3S_1^{(8)}$ is also allowed by conservation laws but it vanishes in leading order in α_S.

In the color evaporation model [32, 33] spin-orbital and color quantum numbers of intermediate quark-antiquark states are irrelevant, and gluon emission during the hadronization phase is assumed to be unsuppressed. This model predicts that all the quarkonium states are produced unpolarized. Averaging the values of the angular distribution parameter in Eq.(1.13), one obtains $\eta_\gamma \simeq 0.15$ for unpolarized χ_2 production. This value does not depend on the energy and is the same for charmonium and bottomonium states.

In conclusion, the differences between the predictions of different mechanisms of heavy quarkonium production for the parameter η_γ, which describes the polarization of χ_{b2}, are large. Therefore, measurement of the polarization of χ_{b2} can be used as a test of NRQCD FA and can extract information about the color octet intermediate state.

Although the color octet contribution is negligible in the production of P-wave charmonium, the measurement of the χ_{c2} polarization provides a possibility to distinguish between the color singlet mechanism and the CEM. On the other hand, care has to be taken in the interpretation of the χ_{c2} polarization data. It is not excluded that the mass of the charm quark is not large enough to apply the NRQCD factorization approach to charmonium production and decay processes. Because of the rather large value of v^2, about 0.3 for the charmonium system, the Fock states at high order of v^2 may contribute significantly and thus can not be neglected.

1.3 Conclusion

A direct way to study parton-parton scattering is to investigate the production of high-p_T direct photons and π^0 mesons. More complete theoretical calculations are needed to understand the nature of the k_T smearing effects. A new generation of inclusive direct-photon and meson measurements is needed to test the theoretical predictions and to improve our knowledge of the gluon distribution function and parton fragmentation mechanism.

In the non-relativistic QCD factorization approach Υ mesons are expected to be produced transversely polarized; the parameter η for the polar angle distribution of quarkonium decay products is about $0.24 \div 0.3$. In contrast, the color evaporation model postulates that multiple soft gluon exchange in the hadronization phase destroys the initial polarization of the heavy quark pair and quarkonium is produced unpolarized. Therefore, the measurement of Υ polarization provides an excellent opportunity to test different models of heavy quarkonium production. In particular, it allows one to distinguish between the NRQCD FA and the color evaporation model. On the other hand, the observation of an extremely large polarization would indicate that Υ mesons are mainly produced through color singlet states and that the color octet parameters for χ_{bJ} production extracted from the Tevatron data should be much smaller than presently assumed.

Chapter 2

The HERA-B experiment

HERA-B is one of the four experiments located at the DESY electron-proton storage ring HERA. HERA-B is a forward spectrometer which uses a 920 GeV proton beam incident on various nuclear targets. The top and side view of the detector are shown in Fig. 2.1. The main physics goal of the experiment is a measurement of CP violation in the "golden-plated" decay channel $B_d^0 \to J/\psi K_S^0$, with subsequent decays of J/ψ into two leptons and K_S^0 into two charged pions [46]. The spectrometer configuration is optimized in order to meet the following physics requirements:

• Due to the small $b\bar{b}$ production cross section, $\sigma_{b\bar{b}}/\sigma_{total} \sim 10^{-6}$ and the small value of the branching fraction of the "golden" decay, the detector has to operate at high interaction rates of about 40 MHz to produce a sufficient number of B mesons. This rate leads to multiple interactions per bunch crossing and high particle multiplicity ($\approx$ 100-200 tracks) per event. Therefore, the detector has to operate in a harsh radiation environment and has to be able to reconstruct multiple interactions per event.

• The trigger has to provide a background suppression of almost a factor of 10^6 while keeping an efficiency of order unity for the B decay channels under investigation. The trigger should also not introduce any dead time in the data acquisition system.

• A high efficiency of the reconstruction of the B decay modes of interest is needed. Good lepton and kaon identification is required.

• In order to provide the necessary time resolution for CP violation, lifetime, and flavour mixing measurements, secondary vertices from B decays must be reconstructed with high efficiency and good resolution.

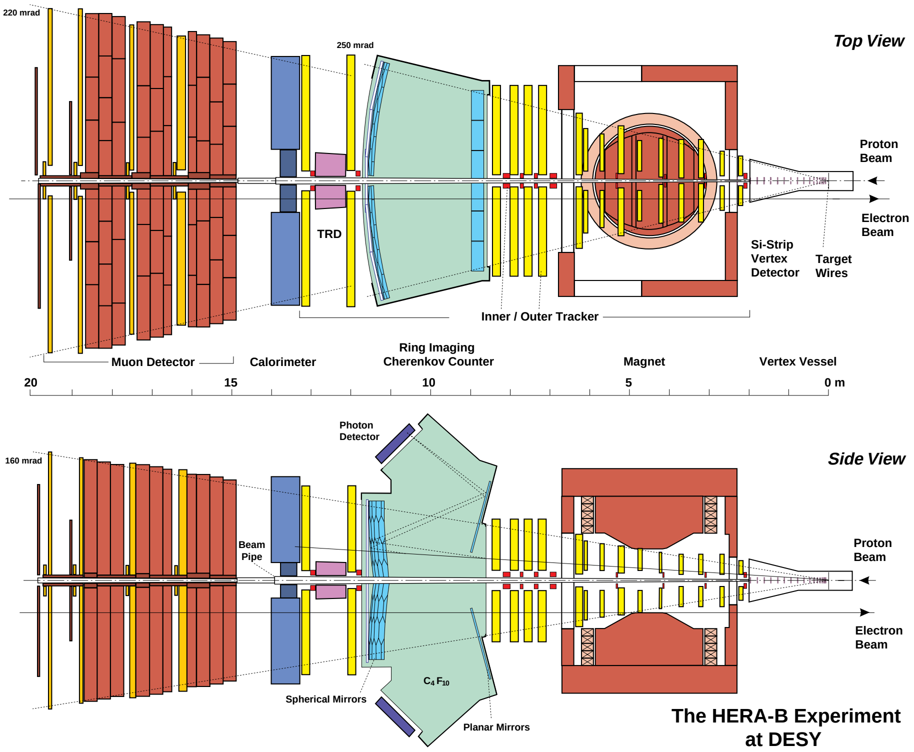

Figure 2.1: *Configuration of the HERA-B detector. The detector components are: a Silicon vertex detector, main tracking system with a dipole magnet, TRD, RICH, electromagnetic calorimeter and a muon system.*

2.1 The internal target

In order to achieve a desirable precision in the CP violation measurement, HERA-B has to operate with an average of 4-5 interactions per event. In order to provide good reconstruction of secondary vertices from the B decays, the interaction points have to be well separated. This is realized by introducing two sets of wires into the halo of the proton beam, approaching it simultaneously from all sides. The wires are positioned at about 4 r.m.s. beam widths ($\approx$2.5 mm) from the beam center and are organized into two stations 5 cm apart along the beam, as shown in Fig. 2.2. The size of a wire is 50 μm in the transverse direction and 500 μm along the beam. The dimensions are chosen such that they are comparable with the resolution of the

Vertex Detector System. The wires are made of different types of material, Al, C, Fe, Ti, which opens the possibility to perform, in parallel, measurements of the dependence of various cross sections on the atomic number.

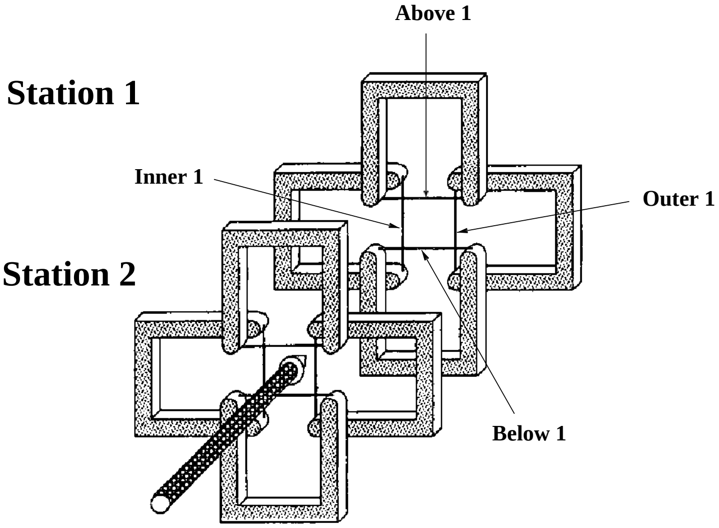

Figure 2.2: *Schematic view of the halo target, consisting of 8 wires on independently movable forks. Wires are organized into two stations with four wires (inner, outer, below, above) in each.*

The quality of the wire target may be characterized by a mean target efficiency ε_T, which is defined as the ratio of the number of protons interacting in the target to the total number of protons which are lost from the beam. It can be calculated from the beam lifetime τ, the total number of stored protons N, and the interaction rate R by

$$\varepsilon_T = R\frac{\tau}{N}.$$

The target efficiency of 70% reached at HERA-*B* is fully sufficient to reach the interaction rates of 40 MHz if beam lifetimes of 100 h are not exceeded.

2.2 Tracking system

The main purposes of the tracking system are to perform efficient track reconstruction in the multi-particle environment, to allow a high precision momentum measurement and to provide fast trigger signals for the first level trigger. The detector has to operate at a very high particle density. The particle flux is increasing with the decrease of the radial distance R from the beam like $\sim 1/R^2$. The required high precision in the reconstruction of the secondary vertices forces the detector elements to be as close to the beam as 1 cm. In order to limit the occupancy of each detector cell, three different types of technology are used in the tracking system:

• **Vertex Detector System (VDS).** The VDS consists of eight superlayers of micro-strip detectors positioned close to the target and 1 - 6 cm from the beam. Each superlayer provides four views: $\pm 2.5°$ and $(90 \pm 2.5°)$. The strip pitch is 25μm which amounts to the spatial resolution of about 12μm. The expected resolution of secondary vertices from the B decay is about 500μm along the beam and between 20 - 30 μm in the transverse direction.

• **Inner tracker (IT).** Micro-Strip Gaseous Chambers (MSGC) with Gas Electron Multipliers (GEM) are chosen for the intermediate region. The IT is placed between 6 and 25 cm from the beam. Each IT superlayer contains two or more layers with strip orientations of 0° or ±5°. The expected space resolution is $\sim 80\mu$m.

• **Outer tracker (OT)**. The outer region is using drift tubes in a honeycomb structure. The OT covers almost the whole geometrical acceptance of the detector down to a radius of 20 cm from the beam. Two types of tubes, having 5 mm and 10 mm diameter depending on the distance from the beam, are used. Each OT superlayer consists of several layers with 0° and ±5° stereo angles. The designed spatial resolution is 200μm.

For the momentum measurements, a dipole magnet with a field integral of 2.2 Tm is used. The expected momentum resolution obtained with the tracking system is about $dp/p \sim 5 \cdot 10^{-3} \oplus 5 \cdot 10^{-5} p$ [47]. The resolution shows a multiple scattering dominated regime below momenta of $\sim$ 50 GeV, and a transition into a linear rise at high momenta. This momentum resolution provides a mass resolution for the B^0 from the “golden decay” of about 6 MeV.

2.3 Particle identification detectors

For particle identification, the following detector components are used:

- The Ring Imaging Čerenkov Counter **(RICH)** is designed to perform identification of kaons in the large momentum range of $3 - 50$ GeV/c.
- The electromagnetic calorimeter **(ECAL)** is used for the electron/hadron discrimination and measurements of the energy of photons in the range from 5 GeV to 200 GeV.
- The Muon detector with absorbers **(MUON)** performs the separation of muons from hadrons and registration of muons with momentum between 5 GeV/c and 200 GeV/c.
- The transition radiation detector **(TRD)** provides additional electron/hadron separation from about 5 GeV to 150 GeV in the region close to the beam, where the track density is very high.

2.4 Trigger

The HERA bunch crossing rate, i.e. the rate of primary interactions, is about 10 MHz. The rate with which the data can be written to tape is limited by 50 Hz. Therefore a rejection of almost a factor of 10^6 has to be achieved by the HERA-B trigger system. The trigger is mainly concentrated on $B^0 \rightarrow J/\psi + X \rightarrow l^+l^- + X$ channels, having two leptons in the final state. It also allows for additional channels accepting different combinations of dileptons like l^+l^- $(l = e, \mu)$ and involves the possibility to trigger on high-p_T hadrons. The trigger system is organized into several levels and has the following structure:

- The pretrigger identifies the lepton or high-p_T hadron candidates. Electrons are identified as the high-E_T clusters in the ECAL; muons as coincidence in the muon pads; and hadrons as combinations of pads in the high-p_T chambers. The candidates define the fields for the track search in the tracking chambers behind the magnet. These fields are called regions of interest, (ROI)'s.
- The first level trigger **(FLT)** uses the ROI defined by the pretrigger and performs the hit search in the next tracking chambers as shown by Fig. 2.3. The algorithm is based on Kalman filtering techniques. The chambers MU4, MU3, MU1, TC2, TC1, PC4, and PC1 are used on this level. The transverse momentum of the track is estimated from the visible deflection of the track

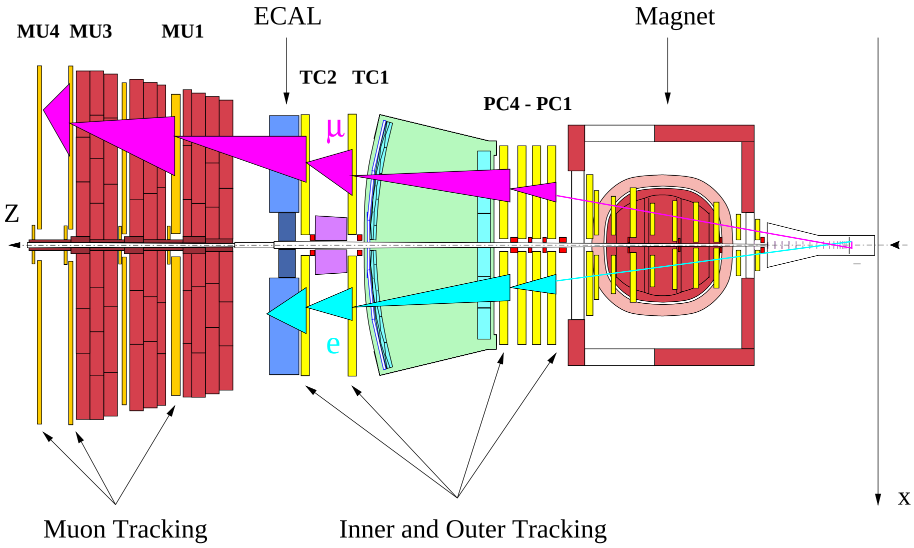

Figure 2.3: *The detector components used in the First Level Trigger.*

in the magnetic field, assuming that the track originates at the target, $p_T = f(\delta x|_{z=0})$. To make event processing faster, look-up tables are used. The invariant mass for each pair of lepton candidates is calculated, and cuts on the invariant mass and on the transverse momentum of the tracks are applied on this level.

- The second level trigger **(SLT)** performs a refit of track parameters involving more superlayers of the tracking chambers, PC2, PC3, and also more layers of PC1 and PC4. Additionally the drift-time information of the chambers is used. The tracks are extrapolated through the magnet to the vertex detector where the reconstruction of primary and secondary vertices is performed. A cut on the vertex separation is applied on this level. When event is accepted by the SLT, readout of data from the second level trigger buffer and event building are performed.

- The third level trigger **(TLT)**. In the case of $B \rightarrow J/\psi + X$ channels, the cut on the vertex separation is sufficient to suppress the background and reduce the trigger rate to a level acceptable for the full event reconstruction. The third level trigger was designed to extend the physics interest to the channels where the tracks are produced with a high impact parameter. The TLT can, for example, perform the search of candidates for semileptonic decays.

• Finally the full event reconstruction and classification is done on the fourth level trigger. The data quality monitoring and preparation of data for calibration and alignment is also performed on this level. The output of the last level trigger is stored on tape.

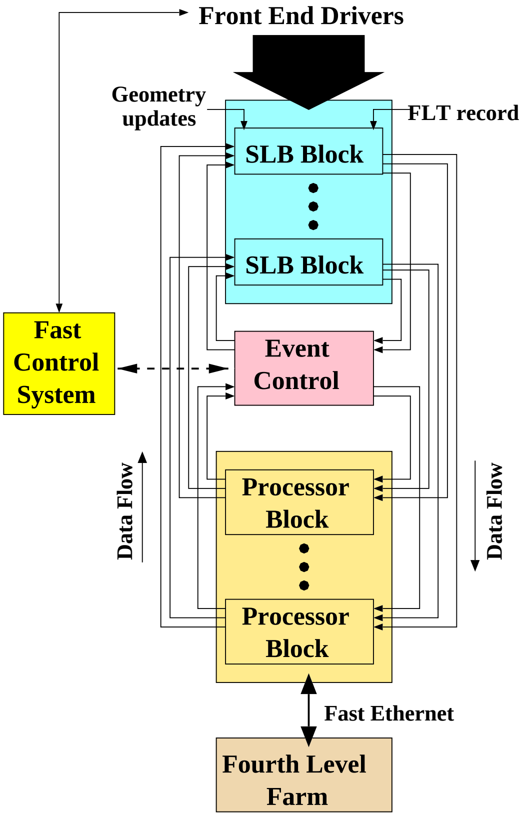

Figure 2.4: *The topology of the HERA-B higher level triggering system. The SLBs are organized into blocks as are the second and third level processor nodes. Event control connects to the input and output of each block. The fast control system triggers event transfer into the SLBs on receipt of a first level trigger.*

The FLT is based on a parallel and pipelined hardware processor system. The system consists of track finding units, track parameter units, and trigger decision unit [48]. While awaiting the FLT decision, data is stored in pipelines

Trigger level	Pretrigger	FLT	SLT	TLT	4LT
Input	10 MHz	10MHz	50 KHz	500 Hz	50 Hz
Latency	1μs	10μs	7ms	100ms	4 s
Reduction	1	200	100	10	2.5

Table 2.1: *Overview of the HERA-B trigger levels.*

in the front end electronics. When event is accepted by the FLT, data is sent to the second level memory buffers (SLB).

The second and third level triggering system is based on the following components:

- The SHARC cluster boards for buffering and switching. The SHARC cluster board carries six ADSP21060(SHARC) processors which can communicate via a global memory bus. The SHARCs have 6 parallel link ports which are used to bring data from the detector into processor memory. The links are also used to connect the SLBs to the switch and for switch interconnections.
- Pentium II PCs (240 nodes) used as trigger processors.

During second and third level processing, event data resides in the SLB, which is built from the SHARC cluster boards. The same cluster board is used to implement a switch as well as to run the event controller. A switching network is needed to route data requests from second level trigger processing farms to SLB nodes, and event data from the buffers back to the second level trigger processors.

The fourth level trigger consists of 200 CPUs in 100 dual-CPU PCs which are integrated in Fast-Ethernet network. Each PC are equipped with 256 MB of memory to allow for the buffering of a few tens of events. A scheme of the HERA-*B* trigger architecture is presented in Fig. 2.4.

The performance of the trigger levels can be characterized by the rejection factor and the latency, i.e. the time which is allocated to trigger for making the decision. The requirements for the HERA-*B* trigger system are presented in Table 2.1.

2.5 Detector simulation

The event generation is performed by the PYTHIA [49] and FRITIOF [50] packages. The usage of these two programs is motivated by the fact that

PYTHIA generates heavy quark production but can only handle nucleon-nucleon interactions. FRITIOF simulates the proton-nucleus collisions including nuclear effects such as energy loss or multiple scattering of partons crossing the target nucleus. The Rutherford parton-parton scattering and soft gluon radiation processes are also integrated into this package.

Generally the simulation of the events like $c\bar{c}$ and $b\bar{b}$ is performed in two steps. The heavy quarks are generated with PYTHIA, and the remaining energy is passed to FRITIOF to complement the event with low p_T particles. Detailed information about the event generation at HERA-B can be found in [6].

The generated particles are subjected to a full GEANT detector simulation, handled by the HBGEAN program [51]. The simulation is based on a realistic description of detector geometry and detector materials and employs all available physics processes such as multiple scattering, photon conversion, and so on. The output of the program is the digitized information which can be reconstructed using the same software reconstruction programs as used for real data.

Chapter 3

Cross section measurement technique and luminosity determination

3.1 Principle of cross section measurement

Many of the physics topics accessible by HERA-B require absolute cross section measurements. The invariant inclusive cross section for the production of a particle of momentum p and energy E can be expressed in terms of the rapidity y, the momentum p_T transverse to the beam direction, and the angle ϕ as

$$E\frac{d^3\sigma}{dp^3} = \frac{d^3\sigma}{d\phi\; dy\; p_T\; dp_T}.$$

In nucleon-nucleus interactions the cross-section is typically calculated per target nucleon using the parameterization of its dependence on the atomic-weight A in the form $\sigma_A = \sigma_N A^\alpha$. For the given number of reconstructed particles, N_{part}, in the rapidity and the transverse momentum bin $\triangle y$ and $\triangle p_T$, the cross section can be determined from the following formula

$$E\frac{d^3\sigma}{dp^3} = \frac{N_{part}}{2\;\pi\;\triangle y\; p_T\;\triangle p_T\;\varepsilon_{DAQ}\;\varepsilon_{Trig}\;\varepsilon_{Rec}\;A^\alpha}\frac{1}{L}, \tag{3.1}$$

where ε_{DAQ}, ε_{Trig} and ε_{Rec} are the data acquisition, trigger, and reconstruction efficiencies respectively, L is the integrated luminosity per target nucleon, and A^α describes the cross section A-dependence.

In the HERA-B experiment, the value of ε_{DAQ} is expected to be of order unity. This is achieved by implementation of the multi-level trigger system which was described in Section 2.1. The ε_{DAQ} can be calculated from the number of lost trigger candidates. The number of lost trigger candidates is counted on each trigger level and is written into the Data Base.

The trigger and reconstruction efficiencies for each sort of particle under investigation are calculated with the Monte Carlo simulations.

As follows from Eq.(3.1), for precise cross-section calculation, reliable estimates of the integrated luminosity L are necessary. Different approaches for the luminosity determination will be discussed in this chapter.

3.2 Definition of luminosity

The time integrated luminosity is defined according to the formula

$$L = \frac{N_{proc}}{\sigma_{proc}}, \tag{3.2}$$

where N_{proc} are the number of interactions of a process of a specific type in a given time interval and σ_{proc} is the process cross section. Since the cross section of inelastic processes σ_{inel} dominates the total pN cross section for HERA-B energies, it is suitable to use σ_{inel} as σ_{proc} in Eq.(3.2). The inelastic cross section can be written in the form

$$\sigma_{inel} = \sigma_{total} - \sigma_{coherent-nucleus} - \sigma_{quasi-elastic},$$

where "coherent-nucleus" and "quasi-elastic" are small corrections for the coherent scattering on the whole nucleus and elastic scattering on individual nucleons in the nucleus respectively.

Another reason to use σ_{inel} is that it is known with a good accuracy. The measurement of the inelastic cross section is a topic of many experiments. As a reference one can take experimental results from [52] where the cross section was measured for a large variety of target materials and different beam energies (60, 200 and 280 GeV). It was found that the cross sections are almost independent of beam energy and can be well fitted by the expression $\sigma_{inel}(A) = \sigma_0 A^{\alpha}$, where A is the atomic weight of the target nucleus, $\alpha \approx 0.7$, and $\sigma_0 \approx 38mb$. HERA-B is operating with several wires made of different materials simultaneously. As the inelastic cross section is material dependent, one can rewrite equation (3.2), introducing the luminosity L^i for each wire "i" (or each type of material), as

$$L^i = \frac{\beta^i N_{inel}^{total}}{\sigma_{inel}^i},$$

where β^i is defined as the fraction of interactions per wire i. For the purpose of luminosity determination in HERA-B the following values of inelastic cross sections have been used:

$$\sigma_{inel}^i = \begin{cases} 225 \pm 7\text{mb} & \text{Carbon} \\ 409 \pm 12\text{mb} & \text{Aluminium} \\ 665 \pm 15\text{mb} & \text{Titanium.} \end{cases}$$

Taking into account the HERA-p bunch structure as shown in Fig. 3.1, the luminosity can be expressed as

$$L^i = \frac{N_{BX}^{total} \beta^i}{\sigma_{inel}^i} \lambda, \tag{3.3}$$

where N_{BX}^{total} denotes how many times filled bunches have passed the target region during the run and λ is the mean number of interactions for filled bunches. The trigger and reconstruction efficiencies are functions of the number of superimposed interactions. Therefore, in the case when some bunches have abnormally high or low number of interactions, the luminosity should be calculated separately for each individual bunch. From formula (3.3) it is obvious that accurate measurements of λ and β^i are of particular importance for the precise luminosity determination. In this chapter the principle of interaction rate measurement will be discussed. A special emphasis will be put on the ECAL Energy Sum method proposed for the interaction rate measurement and monitoring. The feasibility to use the VDS as a cross check of the interaction rate measurement will be demonstrated. Also, the aspects of the determination of rate sharing among wires will be discussed. Finally, the feasibility to use reconstructed primary vertex distribution over wires for calculation of the relative rate sharing will be presented.

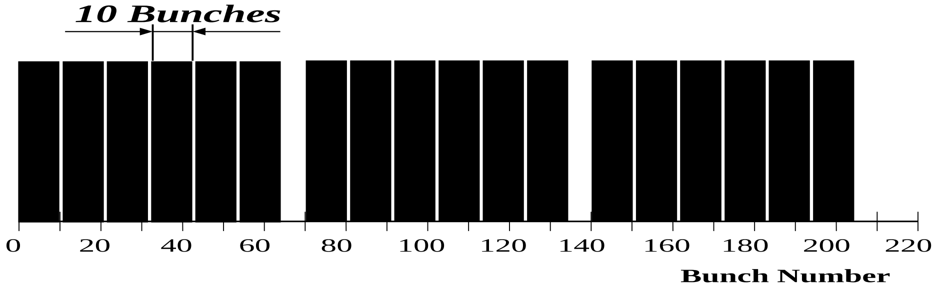

Figure 3.1: *The HERA-p bunch structure. The proton beam is filled in 180 out of a total of 220 bunches, each of which is 1.3 ns length. The bunch spacing corresponds to 96 ns.*

3.3 Interaction rate measurement

3.3.1 Principle of interaction rate calculation

Assuming that the number of interactions N of a particular bunch i obeys Poisson statistics

$$P(N) = \sum_N \frac{{\lambda_i}^N e^{-\lambda_i}}{N!},$$

the average number of interactions λ_i can be determined by simply counting the fraction of "empty" events using some sort of luminosity counter (for the hardware implementation in HERA-B see below). Taking the acceptance A of the luminosity counters into account, the probability of having no interactions can be expressed as

$$P(0) = e^{-A\lambda_i}.$$

Then, the counting rate for each bunch can be written as

$$R_t^i = \frac{R_0}{220}(1 - e^{-A\lambda_i}) = \frac{1}{220}\left\{ \begin{array}{lll} R_0 A\lambda_i & \text{for} & A\lambda_i \ll 1 \\ R_0 & \text{for} & A\lambda_i \gg 1, \end{array} \right.$$

where $R_0 = 1/96\text{ns}$ is the bunch crossing rate. Therefore, in the case of small acceptance, the overall averaged counting rate for 180 filled bunches can be expressed in the form

$$R_t = \frac{180}{220} R_0 A\lambda = R_{BX} A\lambda.$$

Here λ is defined as the average number of interactions in filled bunches and $R_{BX} = 180R_0/220$ is the mean rate with which the filled bunches pass the target region. Consequently, the mean interaction rate can be calculated as

$$R \equiv \lambda R_{BX} = \frac{R_t}{A}. \tag{3.4}$$

3.3.2 Hodoscope counters

In the HERA-*B* '99 setup, the interaction rate was measured by means of four pairs of scintillators mounted in front of the ECAL, arranged symmetrically with respect to the proton beam[1]. The small value of the acceptance of the counters, 0.15% each, guaranteed good linearity between the rate and the mean number of interactions. On the other hand, when the acceptance is small, it is difficult to determine acceptance from simulation because of the necessary large statistics and because of the systematic sensitivity to subtleties in the event generator. Therefore, the scintillator acceptance was calibrated relative to a large acceptance hodoscope (54%), which has been temporarily installed inside the magnet, at moderate rate. The acceptance of the large hodoscopes could be determined reliably on the basis of simulation [6] of inelastic interactions and the detector response. Due to easy handling, the hodoscopes remained the only tool providing the interaction rate determination at HERA-*B*. However, there are several reasons to introduce additional sources for rate monitoring and calibration:

- The large-acceptance hodoscope had to be removed in December '98 because the space was required for installation of tracking devices. Since that time, there was no possibility for absolute interaction rate calibration any more.
- The acceptance changes with changes in the detector setup, since it depends on the amount of material leading to additional particles through secondary interactions.
- The possible instability of the power supply for the counter photomultipliers. When the HV power supply fails or is replaced the calibration could not be precisely retained This happened once during the spring '99 run.

---

[1] In the present setup, these scintillators are installed at the RICH vessel.

- The sensitivity of the hodoscopes to the non-interaction related background.

As one of the alternative tools of interaction rate measurement the ECAL Energy Sum method has been proposed. This method is presently used in HERA-B for the absolute rate calibration. In this chapter a description of this method is given. The analysis is based on the information obtained from the inner part of the electromagnetic calorimeter (see Fig 4.3) and considers data from the interaction rate scan performed in November '99. In these runs, events have been selected without any trigger requirements.

The possibility to use tracks reconstructed in the VDS as a cross check of the interaction rate calibration will also be discussed.

3.3.3 ECAL Energy Sum method

Method overview

The basic idea of the method is to make use of the fact that the mean total energy deposited in the ECAL is proportional to the average number of superimposed interactions.

Let us consider a data sample consisting of N_{total} events. For each event i let us introduce the number of interactions n_i and the total energy deposited in the calorimeter

$$E_i = \sum_{cell=1}^{N_{cell}} E_{cell}\, I(E_{cell} > E_{cut}), \tag{3.5}$$

where N_{cell} is the total number of cells in the inner part of the ECAL, E_{cell} is energy deposited in an individual cell, E_{cut} is the given cell energy threshold, and $I(\cdot)$ is an indicator function defined as

$$I(x) = \begin{cases} 1, & \text{if} \quad x = \text{true} \\ 0, & \text{if} \quad x = \text{false}. \end{cases} \tag{3.6}$$

By definition, the average energy $E^{(N)}$ released for events with exactly N interactions is

$$E^{(N)} = \frac{\sum_{i=1}^{N_{total}} E_i\, I(n_i = N)}{\sum_{i=1}^{N_{total}} I(n_i = N)}. \tag{3.7}$$

Let $P(N)$ be the distribution function for the number of interactions N with the mean value λ. Then, the average energy can be expressed in the form

$$\bar{E} = \sum_{N=1}^{\infty} E^{(N)} P(N).$$

Assuming that the energy scales linearly with the number of interactions, i.e. $E^{(N)} \simeq NE^{(1)}$, the mean number of interactions can be simply determined by dividing the average energy by the energy deposition in one interaction

$$\lambda = \frac{\bar{E}}{E^{(1)}}. \tag{3.8}$$

The assumed linearity of the ECAL energy with respect to the number of interactions will be tested below.

From Eq.(3.8) it is obvious that only $E^{(1)}$ is needed for calibration of this method. Various approaches for the determination of $E^{(1)}$ will be presented in this section.

The energy cell cut in Eq.(3.5) is introduced in order to suppress possible background contribution. On the other hand, increasing the cell cut energy decreases the reconstruction efficiency, as will be discussed in the next section. Therefore, the influence of the different energy cell cuts on the performance of this method has to be tested, and value of the E_{cut} has to be optimized.

Linearity check

The linearity of the ECAL energy has been tested with Monte Carlo simulation based on the FRITIOF event generator and the subsequent full detector simulation. The ECAL reconstruction is performed with the CARE software package [53]. Fig. 3.2 represents the average ECAL energy, summed over all cells with $E_{cell} \geq E_{cut}$ as a function of the number of superimposed interactions. It is observed that Monte Carlo simulation predicts a good linearity of the ECAL response, independent of the cell cut up to E_{cell} of at least 5 GeV. A very good linearity is also observed using real data, when the average energy is plotted versus the interaction rate as determined by the hodoscopes (see Section 3.3.1). A typical example of the average energy dependence on the interaction rate for two types of target materials carbon (wire inner 2) and titanium (wire inner 1) is presented in Fig. 3.3 for an E_{cell} cut of 5 GeV.

The results of straight line fits are also displayed. As is expected, the energy deposition for titanium is larger than for carbon. This can be explained by the fact that the track multiplicity increases with the atomic number, i.e. by the A-dependence of the track multiplicity.

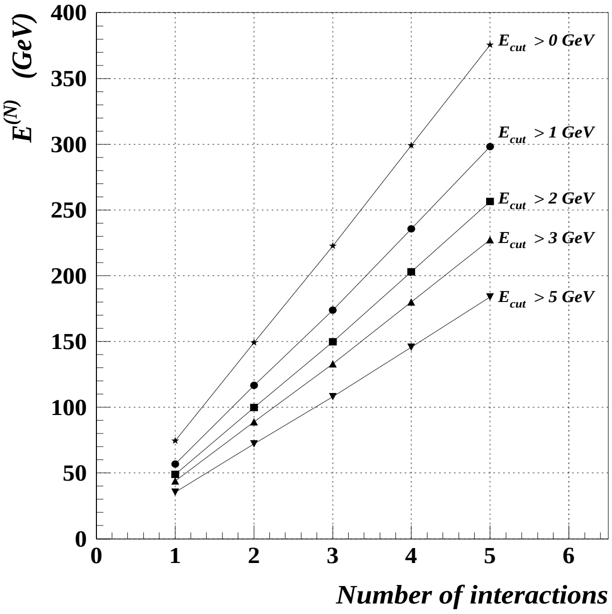

Figure 3.2: *Monte Carlo simulation. The ECAL energy, summed over the cells with $E_{cell} \geq E_{cut}$, is displayed as function of the number of superimposed interactions.*

Energy of a single interaction

There are several approaches to obtain the energy deposition in one interaction:

- Determine $E^{(1)}$ from the data. Single interactions can be tagged at very small rates (so that multiple interactions are highly unlikely), requiring at least one cell in the ECAL with the energy deposition above E_{cut}
- Determine $E^{(1)}$ from the Monte Carlo simulation.

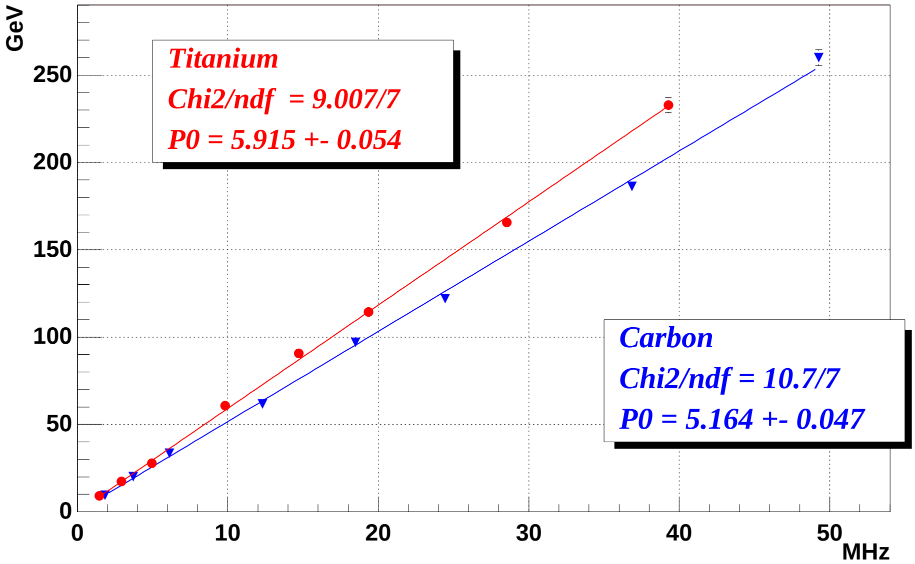

Figure 3.3: *ECAL energy, summed over cells with* $E_{cell} \geq 5GeV$ *for a carbon (inner 2) and a titanium (inner 1) wire, as function of the interaction rate. Also shown are fits using a linear function (3.14).*

The Zero-Rate-Limit

The selection of events which contain only one interaction can be performed at low interaction rates, taking into account the fact that the fraction of events with multiple interactions decreases when the interaction rate tends to zero, i.e. $\lambda \to 0$. For Poisson statistics one can write

$$\frac{P(N>1)}{P(N=1)} \sim \lambda \to 0. \tag{3.9}$$

On the other hand, requiring the total energy deposition in the ECAL $E_i > 0$, one selects only "non-empty" or "tagged" events which contain at least one interaction.

Let us define the efficiency for tagging events with exactly N interactions by requiring the total energy deposited in the ECAL $E_i > 0$ (i.e., at least one cell above E_{cut}, see Eq.(3.5)) as

$$\varepsilon^{(N)} = \frac{\sum\limits_{i=1}^{N_{total}} I(n_i = N)\; I(E_i > 0)}{\sum\limits_{i=1}^{N_{total}} I(n_i = N)}. \tag{3.10}$$

The efficiency dependence on the applied cell energy cut and the number of superimposed interactions was studied with Monte Carlo simulations for two types of target materials, carbon and titanium. The efficiency for tagging single interactions as function of the cell energy cut is presented in Fig. 3.4. One sees that the efficiency is slightly decreasing with the increase of the cell energy cut, but is still high, about 80%, up to $E_{cut} = 5$ GeV. Due to the A-dependence of the track multiplicity, the efficiency for the heavier target material is slightly larger than for the lighter target material. The efficiency for tagging an event with N interactions, $\varepsilon^{(N)}$, is shown in Fig. 3.5 as function of N for a cell energy cut of 5 GeV. As can be seen, the efficiency increases

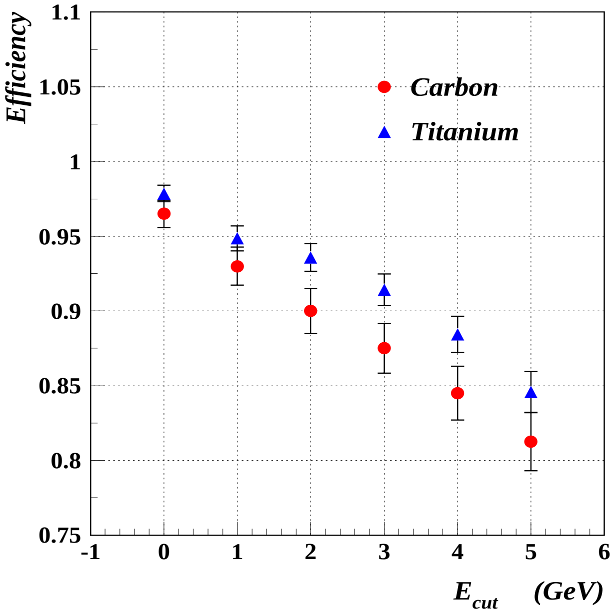

Figure 3.4: *The efficiency for tagging single interactions as function of the cell energy cut for carbon and titanium wires.*

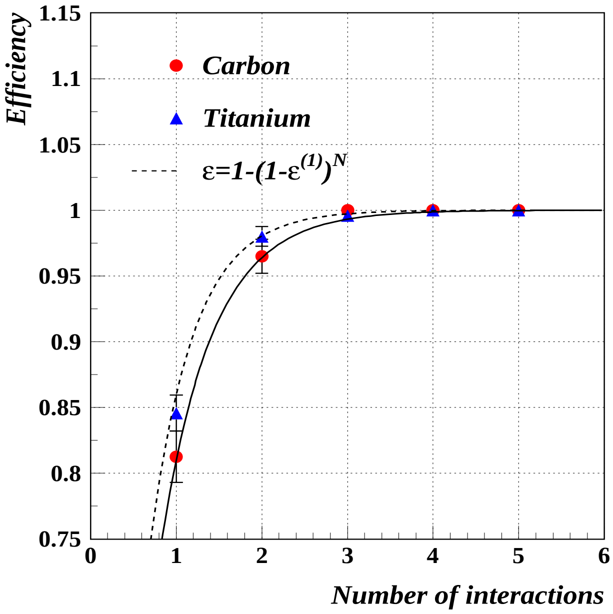

Figure 3.5: *The tagging efficiency as function of the number of superimposed interactions for a cell energy cut of 5 GeV. Lines show fits of the analytic parameterization (3.11).*

rapidly with the number of superimposed interactions. Due to the statistical independence of interactions, the efficiency can be parameterized according to a binomial distribution (see Fig. 3.5)

$$1 - \varepsilon^{(N)} = (1 - \varepsilon^{(1)})^N. \tag{3.11}$$

The parameterization (3.11) is valid as long as the total cell energy in overlapping clusters from different interactions only rarely exceeds E_{cut}. In the simulation of the HERA-B ECAL, such higher order correlations between different interactions were found to be negligible.

Let us define the mean energy for tagged events with exactly N interactions as

$$\langle E \rangle_{tagged}^{(N)} = \frac{\sum_{i=1}^{N_{total}} E_i \; I(n_i = N) \; I(E_i > 0)}{\sum_{i=1}^{N_{total}} I(n_i = N) \; I(E_i > 0)}. \tag{3.12}$$

As follows from Eq.(3.7) and Eq.(3.10) $\langle E\rangle^{(N)}_{tagged}$ can be related to the average energy $E^{(N)}$ as

$$\langle E\rangle^{(N)}_{tagged} = \frac{\sum\limits_{i=1}^{N_{total}} E_i\, I(n_i = N)\, I(E_i > 0)}{\sum\limits_{i=1}^{N_{total}} I(n_i = N)} \cdot \frac{\sum\limits_{i=1}^{N_{total}} I(n_i = N)}{\sum\limits_{i=1}^{N_{total}} I(n_i = N)\, I(E_i > 0)} = E^{(N)} \cdot \frac{1}{\varepsilon^{(N)}}. \tag{3.13}$$

Taking Eq.(3.13) into account, and making assumptions about the Poisson statistics for the number of interactions, and N-dependence of $E^{(N)}$ and $\varepsilon^{(N)}$, the mean energy per tagged event can be expressed as a function of the parameter λ as

$$\langle E\rangle_{tagged} = \frac{\sum\limits_{N=1}^{\infty} E^{(N)} \frac{1}{\varepsilon^{(N)}} P(N)\varepsilon^{(N)}}{\sum\limits_{N=1}^{\infty} P(N)\varepsilon^{(N)}} = \frac{\lambda E^{(1)}}{1 - e^{-\lambda\varepsilon^{(1)}}}, \tag{3.14}$$

with the following asymptotic behavior:

$$\begin{aligned} \langle E\rangle_{tagged} &\to \frac{E^{(1)}}{\varepsilon^{(1)}} && \lambda \to 0 \\ \langle E\rangle_{tagged} &\to \lambda E^{(1)} && \lambda \to \infty. \end{aligned}$$

This means that the mean energy for tagged events is tending to ratio of $E^{(1)}$ and efficiency $\varepsilon^{(1)}$ in the zero rate limit. The mean energy for tagged events as a function of the interaction rate for the titanium (inner 1) wire and different cell energy cuts is shown in Fig. 3.6. Also shown are fits using the function (3.14).

The interaction rate determined with the ECAL method R_{ECAL} was compared with the rate obtained with the hodoscope counters R_{HOD} . The average energy $\bar{E}$ per unit of the the hodoscope rate was taken from the fit of the dependence of the average energy on the interaction rate shown in Fig. 3.3, to a linear function. The mean number of interactions λ was calculated according to Eq.(3.8). In this equation, the energy $E^{(1)}$ was obtained from the fit of the mean energy for tagged events shown in Fig. 3.6, to the function (3.14). The interaction rate R_{ECAL} was calculated using the obtained

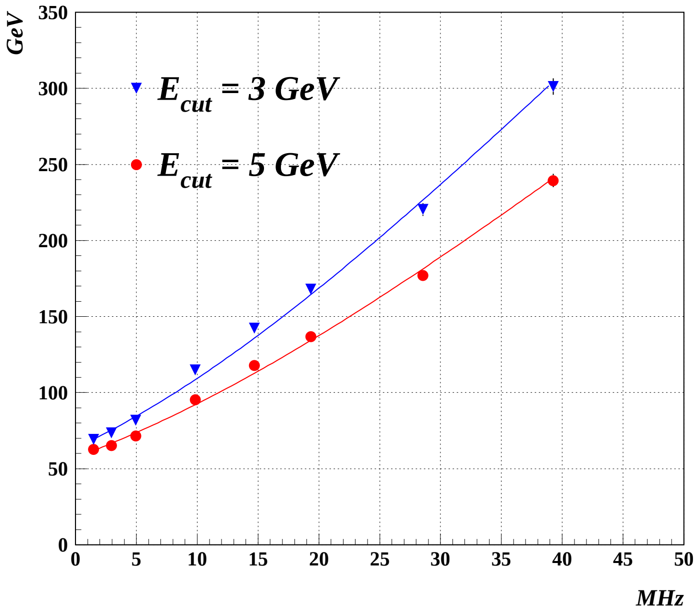

Figure 3.6: *Tagged energy versus interaction rate for various* E_{cell} *cuts for the titanium (inner 1) wire. Also shown are fits using the function (3.14).*

value of the mean number of interactions according to Eq.(3.4). The ratio of interaction rates determined with the ECAL method using different cell energy cuts relative to the rate determined with the hodoscope counters for the titanium (inner 1) wire is presented below

$$\frac{R_{ECAL}}{R_{HOD}} = \begin{cases} 1.05 \pm 0.05 & E_{cell} > 3\ GeV \\ 1.07 \pm 0.05 & E_{cell} > 4\ GeV \\ 1.06 \pm 0.05 & E_{cell} > 5\ GeV. \end{cases} \tag{3.15}$$

From Eq.(3.15), it is clear that the interaction rate determined with the ECAL method is not very sensitive to the cell energy cuts. However, as will be discussed later, it is preferable to use E_{cell} cuts because of possible background contributions. The efficiency $\varepsilon^{(1)}$ is also determined in the fit using function (3.14) and can, therefore, be directly compared with the predictions from Monte Carlo simulation (see Table 3.1).

From Eq.(3.15) one can conclude that the rate determined with the ECAL method is almost equal to the rate determined with the hodoscope counters;

the hodoscope rate is about 6% higher for the titanium wire. This value was used for the correction for the hodoscope acceptance for the titanium wire[2].

After applying corrections for the hodoscope acceptances, the rate determined with the ECAL method versus the rate determined with the hodoscope counters for carbon and titanium wires and $E_{cut} = 5$ GeV is displayed in Fig. 3.7.

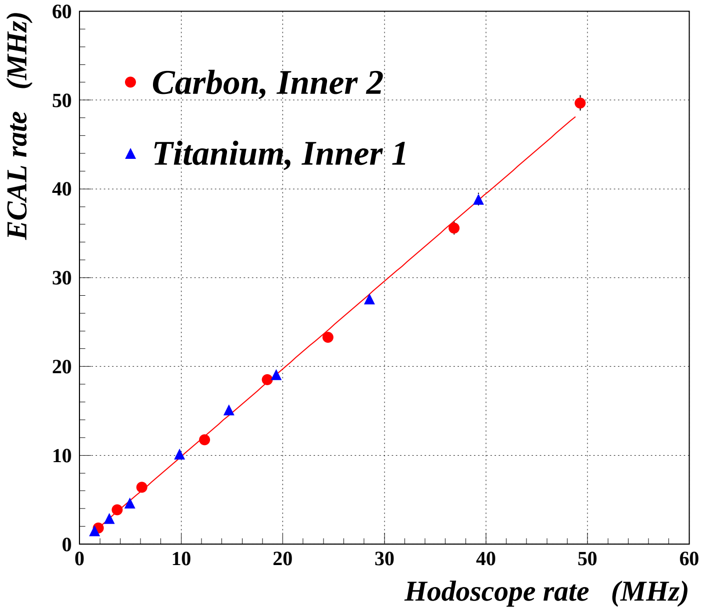

Figure 3.7: *ECAL rate versus the hodoscope rate for the carbon (inner 2) and titanium (inner 1) wires. An energy cut of* E_{cut}=5 *GeV is applied.*

Correlation with the Vertex Detector System

Another approach for tagging single interactions is to use correlations with other detectors, for instance with the Vertex Detector System. In this case events with the single interaction can be determined as discussed above at

---

[2] For the carbon wire the value of the hodoscope acceptance was corrected down by about 20%. The different values of the acceptance corrections for carbon and titanium materials can be explained by the fact that no corrections to the acceptance of the hodoscope counters due to the A-dependence of the track multiplicity were applied at the time when this analysis has been performed.

low rate, by requiring a track coming from a target region. The advantage of this method is a suppression of a possible non-target related background. On the other hand, stringent target constraints can increase the fraction of events with more interactions than one and, therefore, exaggerate the mean energy.

For the VDS analysis, the CATS reconstruction program [54] has been used. As a target constraint, a track has been required to originate from a box shaped region around the wire. The box length and width have been chosen as 3σs of distributions of X and Y track coordinates at $Z = Z_{wire}$.

The results of the mean energy for tagged events with one interaction and efficiency of tagging single interactions, determined with the Zero-Rate-Limit method and by means of Monte Carlo simulation are presented in Table 3.1. In the case, when single interactions were tagged by requiring a reconstructed track in the VDS, $E^{(1)}$ was calculated according to Eq.(3.10), where the efficiency $\varepsilon^{(1)}$ was taken from the Monte Carlo simulations. As can be seen from Table 3.1, both methods give consistent results, although the values of the mean energy $E^{(1)}$ obtained from the Monte Carlo simulation for both titanium and carbon wires are slightly lower. The errors on the $E^{(1)}$ determination, obtained from the fit to the function (3.14) amount to about 5% for both carbon and titanium materials.

Parameters	**MC**	**Zero Rate Limit**	
		Fit	**VDS Correlation**
Carbon			
$E^{(1)}$ ($E_{cell} > 5$ GeV) GeV	37.3	44.6 ± 2.4	44.1 ± 1.8
$\varepsilon^{(1)}$ %	82	82.5 ± 5.5	-
Titanium			
$E^{(1)}$ ($E_{cell} > 5$ GeV) GeV	43.8	47.57 ±2.5	49.4 ±2.0
$\varepsilon^{(1)}$ %	85	83.9 ± 4.8	-

Table 3.1: *Average energy in one interaction and efficiency for tagging single interactions obtained with Monte Carlo simulation and the Zero-Rate-Limit method.*

For a qualitative check of the agreement between Monte Carlo simulation and data a direct comparison of the energy spectra has been made. As an example, the 16 MHz interaction rate run from a rate scan taken in December '98 has been analyzed. In the simulation, events have been generated with poissonian distribution adopted for the number of superimposed interactions, the mean number of interactions being chosen according to the interaction rate, see Eq.(3.4). Two Monte Carlo data samples have been produced corresponding to 16 MHz and 30 MHz interaction rates. The energy spectra for the data and for simulated events are shown in Fig. 3.8. As can be seen, the shapes of the spectra are similar for the data and for events simulated according to the 16 MHz interaction rate. As is expected, Monte Carlo events simulated for the double interaction rate does not fit the data.

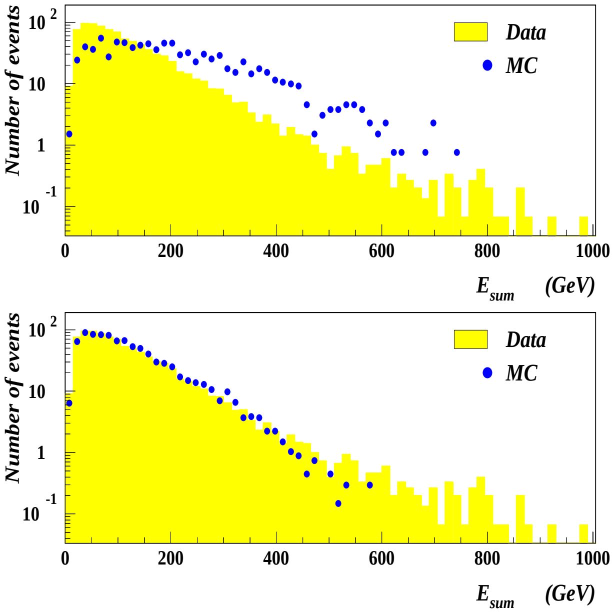

Figure 3.8: *Energy sum spectra for a 16 MHz interaction rate run together with expectations from Monte Carlo simulation corresponding to the 30 MHz (top) and 16 MHz (bottom) interaction rates.*

Estimation of the background contribution

One of the most important aspects of the rate calculation is the estimation of the contribution of possible non-target related background. There are several sources of background such as hot channels in the ECAL, and particles coming from the beam pipe originating from interactions in the beam collimators. The background can increase the hodoscope counter rate and, therefore, can lead to an overestimation of the interaction rate. The background can also affect the ECAL rate by increasing the average energy deposition. The background contribution can be taken into account by introducing an additional term in Eq.(3.8) so that it can be written as

$$\bar{E} = E^{(1)}\lambda + \sum_{N=1}^{\infty} P(N) E_{BG}^{(N)},$$

where $E_{BG}^{(N)}$ denotes an average background energy deposition in the ECAL for events with N superimposed interactions.

The background estimation is performed using runs with target fully retracted from the beam. For these runs about 1% of events have been registered with total energy deposition above $E_{cut} > 5$ GeV. The average background energy is about 0.09 GeV. In Table 3.2 the average background energy is compared with the mean energy observed for interaction rates 1 MHz, 5 MHz, and 10 MHz. It can be concluded that the background level is small.

Rate (MHz)	λ	$\bar{E}_{target}$ (GeV)	$\bar{E}_{BG}$ (GeV)	BG fraction (%)
1	0.12	5.92	0.09	1.52
5	0.59	29.58	0.09	0.3
10	1.18	59.15	0.09	0.15

Table 3.2: *Background energy contribution estimated from runs with the target fully retracted from the beam.*

The background estimate has been been performed with bunches which are not filled with protons, see Fig. 3.1[3]. The average background energy, summed over the cells with $E_{cell} > 2.5$ GeV and 5 GeV, within empty bunches as a function of interaction rate is shown in the upper plot of Fig. 3.9. The ratio of the average background energy to the average energy $\bar{E}$ determined for the bunches which are filled with protons is presented in the lower plot. The inspection of these distributions shows that the average background energy is independent of the interaction rate and its contribution to the $\bar{E}$ is negligible, less than 1%, even at low rate.

---

[3] As it was described in [55], besides the interactions due to the bunched protons, a background from bunch uncorrelated interactions may appear, due to the so called coasting beam.

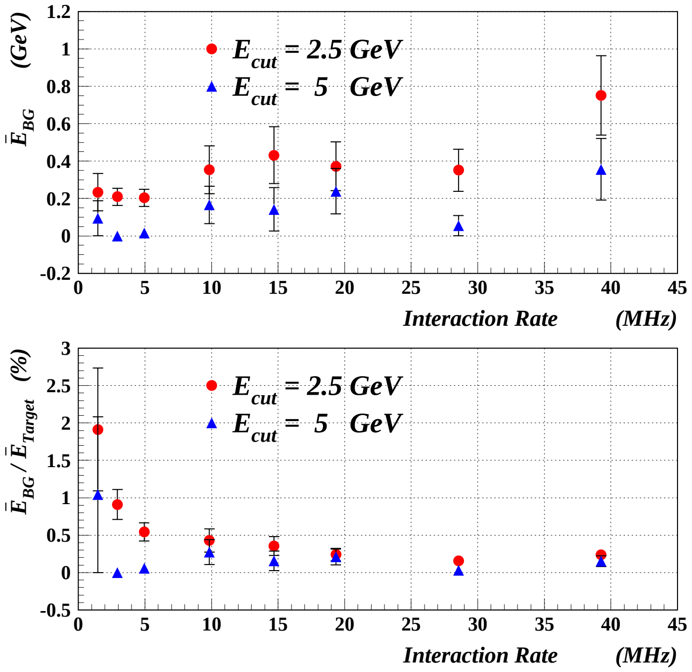

Figure 3.9: *Top: ECAL background energy, summed over the cells with* $E_{cell} > 2.5$ *GeV and 5 GeV, in bunches which are not filled with protons as function of the interaction rate. Bottom: Ratio of the background energy to the total energy versus the interaction rate.*

3.3.4 Interaction rate measurement with the Vertex Detector System

As a cross-check of the interaction rate calibration performed with the ECAL Energy Sum method one can use information from the Vertex Detector System, exploiting the fact that a "linear response" method, discussed in Section 3.3.2, can be applied to any quantity which scales linearly with the interaction rate. Such quantities can, for instance, be reconstructed space points, tracks, primary vertices [54], and so on. On the other hand, each step of the reconstruction involves additional uncertainties, which may break the linearity and make the rate calibration a difficult task. In this section, the possibility of using reconstructed VDS tracks as an additional rate calibration method is demonstrated. The present analysis is based on the same rate scan used for the analysis in the previous section.

Assuming that the reconstructed track multiplicity scales linearly with the number of superimposed interactions N, i.e. $\langle n\rangle^{(N)}_{tracks} \simeq N\langle n\rangle^{(1)}_{tracks}$, the mean number of interactions λ (for an arbitrary distribution function $P(N)$) can be determined using the following expressions:

$$\langle n\rangle_{tracks} = \sum_N P(N)N\langle n\rangle^{(1)}_{tracks} = \lambda\langle n\rangle^{(1)}_{tracks}$$

$$\lambda = \frac{\langle n\rangle_{tracks}}{\langle n\rangle^{(1)}_{tracks}}. \tag{3.16}$$

Here $\langle n\rangle_{tracks}$ is the average number of reconstructed tracks and $\langle n\rangle^{(1)}_{tracks}$ is the average number of reconstructed tracks in single interactions.

The linear scaling of the track multiplicity with the number of superimposed interactions has been checked by Monte Carlo simulation for inelastic events, generated for two types of target materials, titanium and carbon. Generated events have been passed through the full HERA-B detector simulation. For the VDS analysis, the CATS reconstruction program has been used. As a target constraint, a track has been required to originate from a box shaped region around the wire. The box length and width have been chosen as a 3σs of distributions of X and Y coordinates of the reconstructed tracks at $Z = Z_{wire}$. The simulated X and Y coordinates of reconstructed tracks for the carbon (inner 2) wire are shown in Fig. 3.10.

The relative deviation of the reconstructed track multiplicity from the linear function for the cases with no target constraint and a 3σ target constraint applied are presented in Fig. 3.11 as a function of the number of superimposed interactions. A small deviation from the linear dependence, increasing with the number of interactions, is observed for both cases. This can be explained by the interplay of two effects, an increase of the number of ghost tracks and a drop of reconstruction efficiency (a more detailed study of these effects can be found in [56]). In the case when a 3σ target constraint is applied the average number of reconstructed tracks is smaller than that expected for strictly linear scaling of track multiplicity versus the number of superimposed interactions. The difference of the track multiplicity increases with the number of interactions (and, therefore, increases with the interaction rate, see Eq.(3.4)) and amounts to about 5% in the interaction rate range of [30-40] MHz.

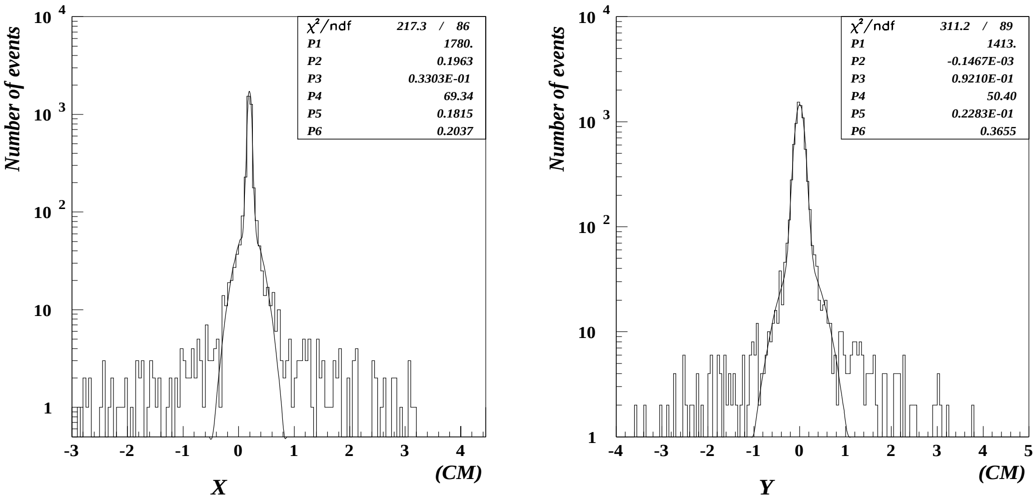

Figure 3.10: *Monte Carlo simulation. Distributions of X and Y track coordinates at* $Z = Z_{wire}$ *for the inner 2 wire.*

The average number of reconstructed tracks for a carbon and a titanium wire is shown in Fig. 3.12 as a function of the interaction rate. Also shown are fits to a linear function. As can be seen, the track multiplicity scales almost linearly with the interaction rate. Some saturation at 30-40 MHz is observed.

To determine the number of tracks in one interaction, the Zero-Rate-Limit method described in previous section has been used. Events with single interactions have been tagged, by requiring at least one reconstructed track in the VDS. The average number of tracks in tagged events is shown in Fig. 3.13 as a function of the interaction rate. This dependence is fit with the function (see Eq.(3.14))

$$\langle n\rangle^{tagged}_{tracks} = \frac{\lambda\langle n\rangle^{(1)}_{tracks}}{1-\exp^{-\lambda\epsilon^{(1)}}}, \tag{3.17}$$

where $\epsilon^{(1)}$ is the efficiency of tagging single interactions. The track multiplicity per tagged single interaction $\langle n\rangle^{(1)}_{tracks}$ is found to be 7.72 ± 0.19 and 5.80 ± 0.16 for titanium and carbon, respectively. As is expected, the obtained multiplicity for titanium is higher than for carbon due to the A-dependence of the track multiplicity. The efficiencies for tagging single interactions $\varepsilon^{(1)}$ are estimated from Monte Carlo simulations and are found to be 95.5% and 94.8% for titanium (inner 1) and carbon (inner 2) wires respectively.

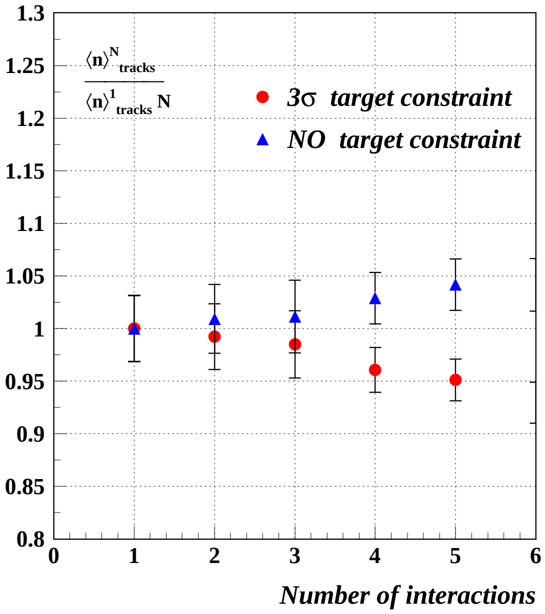

Figure 3.11: *Ratio of mean reconstructed track multiplicity and the expectation for strictly linear scaling of track multiplicity versus the number of superimposed interactions.*

The interaction rate obtained by the VDS tracks R_{VDS} was compared to the rate determined with the hodoscope counters R_{HOD}. The average number of reconstructed tracks $\langle n \rangle_{tracks}$ per unit of the hodoscope rate in this formula was obtained from the fit of the dependence of the average tracks multiplicity on the interaction rate shown in Fig. 3.12, to a linear function. The fit was performed in the interaction rate range of [0-25] MHz, where a good linearity of the track multiplicity versus the interaction rate has been observed. The mean number of interactions λ was calculated according to Eq.(3.16). The interaction rate R_{VDS} was calculated using the obtained value of λ according to Eq.(3.4). The ratio of the interaction rate determined with the VDS method to the rate given by the hodoscope counters for the titanium wire is

$$\frac{R_{VDS}}{R_{HOD}} = 1.01 \pm 0.03. \tag{3.18}$$

As can be seen, this ration is in a good agreement with results obtained

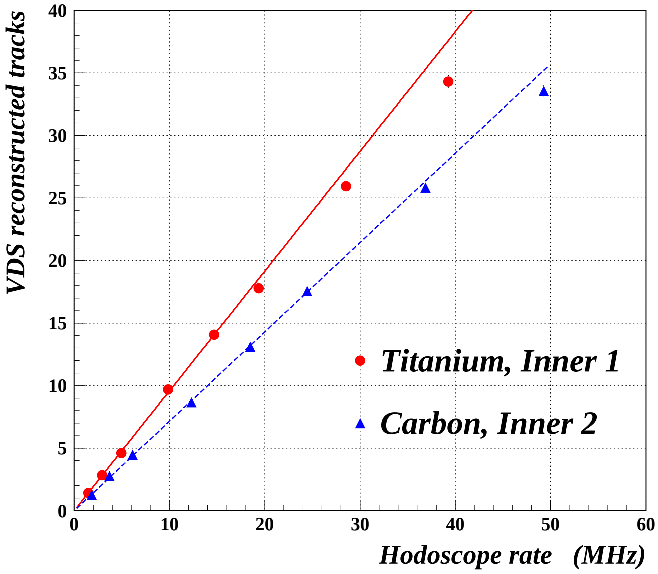

Figure 3.12: *Average track multiplicity versus the interaction rate for the carbon wire (inner 2) and the titanium wire (inner 1). Also shown are fits using a linear function in the interaction rate range of [0,25] MHz (the fit functions are extrapolated to the interaction rate region above 25 MHz).*

with the ECAL method presented in Eq.(3.15). Comparing interaction rates obtained with the ECAL method and using reconstructed VDS tracks indicates an uncertainty of about 5%. This uncertainty can be considered as the systematic error on the interaction rate calibration.

Fig. 3.14 shows the rate determined by the VDS tracks versus the rate determined with the hodoscope counters for carbon and titanium wires. As can be seen, both rates are in a good agreement.

As a qualitative check of the rate calibration and the agreement between simulation and real data a direct comparison of the reconstructed track spectra has been performed. For this, Monte Carlo events have been generated with a poissonian distribution adopted for the number of superimposed interactions, the mean number of interactions being chosen according to the interaction rate. An example of a multiplicity spectrum for a 12 MHz interaction rate run with a titanium wire is shown in Fig. 3.15. The integral of the distribution from simulated data is normalized to the total number of real events. As can be seen a very good agreement between simulation and real data is observed.

3.4 Rate sharing among wires

3.4.1 Charge integrators

HERA-B is operating with multiple interactions per event. In order to provide a good vertex separation and perform a precise luminosity measurement these interactions should be as equally as possible distributed among the wires as possible. This is currently achieved by a feedback system, based on the output of charge integrators [57]. Charge integrator devices measure the charge induced by protons passing through the target. This charge is then converted into an output frequency which is proportional to the interaction rate and constitutes 10-30 Hz per MHz of interaction rate. For calibration reasons, there is a constant current flowing through the targets from 'long life' batteries which contribute an additional baseline frequency of about 500 Hz. One charge integrator is connected to each wire. The system automatically controls the total interaction rate and equalizes the rate sharing among the wires by moving the target wires with respect to the beam.

An example from a multiwire run (RUN#136) is shown in Fig. 3.16. Four titanium wires, all in the first target station, have been operated simultaneously. The rate contributions from the individual wires are shown in the lower plot. The sum of four rates measured by the charge integrators and the hodoscope rate is presented in the upper plot (to see the difference between these rates, the charge integrator rate is scaled up by a factor of 1.1). One can see that the charge integrator measurements are in a very good agreement with the hodoscopes. The rate sharing among wires for the 30 MHz interaction rate part of this run is plotted in Fig. 3.17. As can be seen, the charge integrator based target steering program provides an almost equal rate contribution for all operating wires.

Charge integrator devices appear to be a powerful tool for rate monitoring and target steering. They are easy in construction and operation and are independent of any acceptance. Drawbacks of charge integrator are:

- Relatively small sensitivity to the interaction rate, 10-30 Hz per one MHz with respect to the baseline frequency 500 Hz require a high baseline stability[4]. There is a "long term" drift of the baseline due to the slow discharge of the batteries. Sources of possible "short term" baseline fluctuations are also being intensively studied.

---

[4] New charge integrators with higher sensitivity, 5-8 kHz/MHz were installed in December 1999.

- An absolute rate calibration is needed for each charge integrator. This can be performed with the aid of the ECAL Energy Sum method.

3.4.2 Reconstruction of primary vertices

In addition to the charge integrator method the rate sharing among wires can be determined with the VDS by direct counting of the interaction points for each wire. The track reconstruction in the VDS is performed with the CATS program. The vertex fitting is done by the ROVER [58] package. The spatial distribution of reconstructed vertices for the 30 MHz interaction rate run is shown in Fig. 3.18. As was mentioned in the previous section, the determination of the absolute number of reconstructed vertices requires the knowledge of the vertex reconstruction efficiencies. Here, we concentrate on the relative vertex sharing among wires defined by

$$K^i = \frac{R_i}{\sum\limits_{N_{wires}} R_i}, \tag{3.19}$$

where R_i is the mean number of reconstructed vertices for an individual wire i. Assuming that the vertex reconstruction efficiency is the same for all wires within one target station, one can cancel it out in Eq.(3.19). It should be noted that all four wires of the first station are made of the same material, titanium. Therefore, no correction for the A-dependence of the track multiplicity is needed. The results of the relative rate sharing for the 30 MHz interaction rate run determined with the charge integrators and vertex counting are presented in Table 3.3.

It can be seen that the interaction rate is almost equally shared among the four wires. Both methods, charge integrator and vertex counting, are in good agreement, giving practically the same fractional contributions of individual wires the interaction rate.

In Fig. 3.19, the number of wires where vertices have been found is plotted versus the number of reconstructed vertices. In order to perform a qualitative check of the vertex sharing among wires, a Monte Carlo simulation has been performed for the same wire configurations. Events have been generated for the mean number of superimposed interactions as calculated from the interaction rate. The results of the Monte Carlo simulation are shown in the upper plot of Fig. 3.19. The lower plot shows the result from real data. As can be seen, the distribution patterns are similar for both simulation and

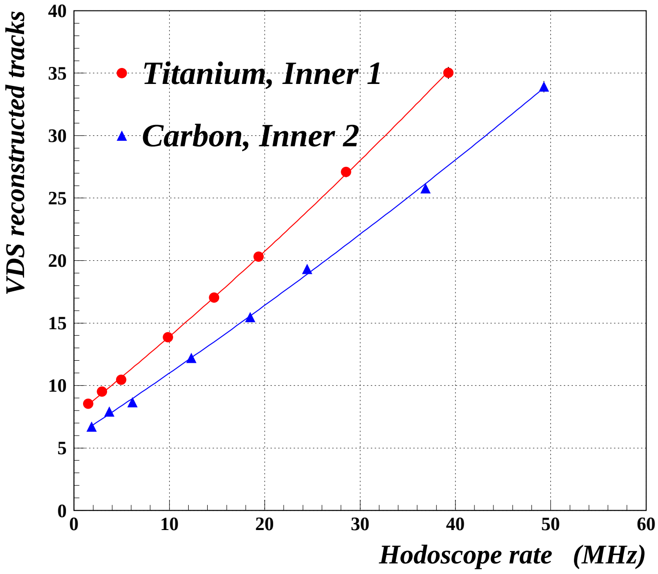

Figure 3.13: *Track multiplicity for tagged events as a function of the interaction rate. Also shown are fits using the function (3.17).*

Wire	**Charge Integrators** %	**Vertices** %
Above	26.06 ±0.08	26.6 ±0.7
Below	24.26 ±0.10	25.9 ±0.7
Inner	23.49 ±0.06	21.4 ±0.7
Outer	26.20 ±0.07	26.1 ±0.7

Table 3.3: *Relative rate sharing among wires obtained with the charge integrators and from counting of primary vertices.*

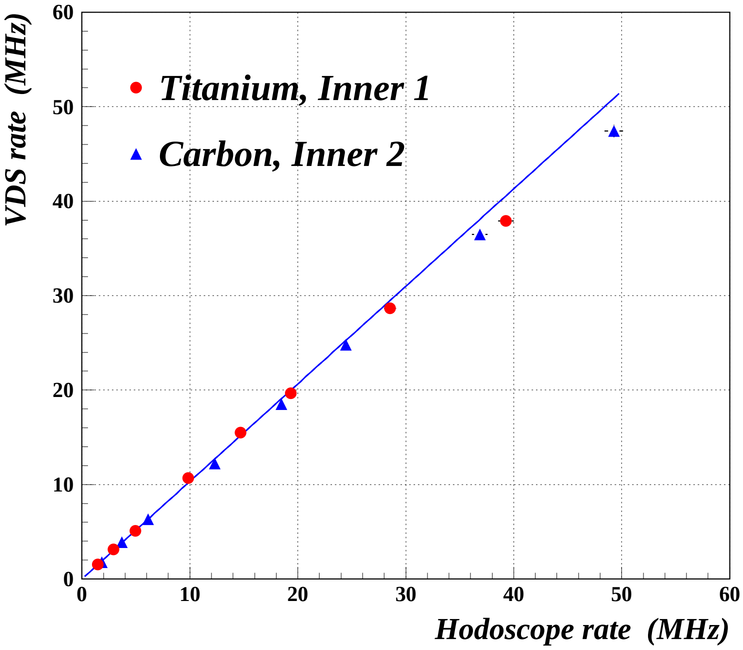

Figure 3.14: *Rate determined by VDS tracks versus the rate determined using the hodoscope counters for the carbon wire (inner 2) and the titanium wire (inner 1).*

real data. The observed diagonal structure indicates that the interactions are uniformly distributed among wires. The distribution of the number of reconstructed vertices summed over all four wires for data and Monte Carlo simulation is shown in Fig. 3.20. Again, fair agreement between simulation and real data is achieved.

3.5 Conclusion

It has been shown that the ECAL Energy Sum method is a powerful tool for the interaction rate measurement at the HERA-B experiment. The main features of the proposed method are:

- It is easy to use. Only $E^{(1)}$ is needed for the calibration of the method.
- It is almost independent of any Monte Carlo simulations. Due to the large acceptance of the calorimeter, only a small correction of the reconstruc-

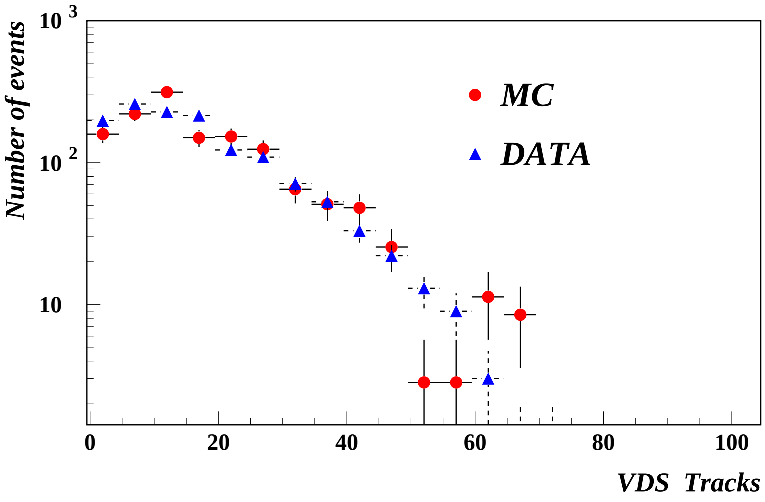

Figure 3.15: *Reconstructed track multiplicity for a 12 MHz interaction rate run with a titanium wire.*

tion efficiency based on the Monte Carlo simulation is needed.

• There is a possibility to perform a cross check of the rate determination by applying different cell energy cuts.

• The contribution of a possible background can be suppressed by applying cuts on the cell energy.

• Events with abnormally high number of interactions can be distinguished by applying cuts on the total energy deposited in the ECAL.

• The method is independent of the distribution function of the number of interactions, $P(N)$.

It has been shown that the interaction rate calibration can be cross checked by counting the number of reconstructed tracks in the Vertex Detector System. This technique is based on the extension of the linear response method and needs a precise estimate of the VDS track reconstruction efficiency. However, determination of the reconstruction efficiency involves additional systematic uncertainties, which make the rate calibration with the help of the VDS a rather complex task.

It has also been demonstrated that counting of primary vertices can be used to perform a direct check of the rate sharing among wires given by charge integrators.

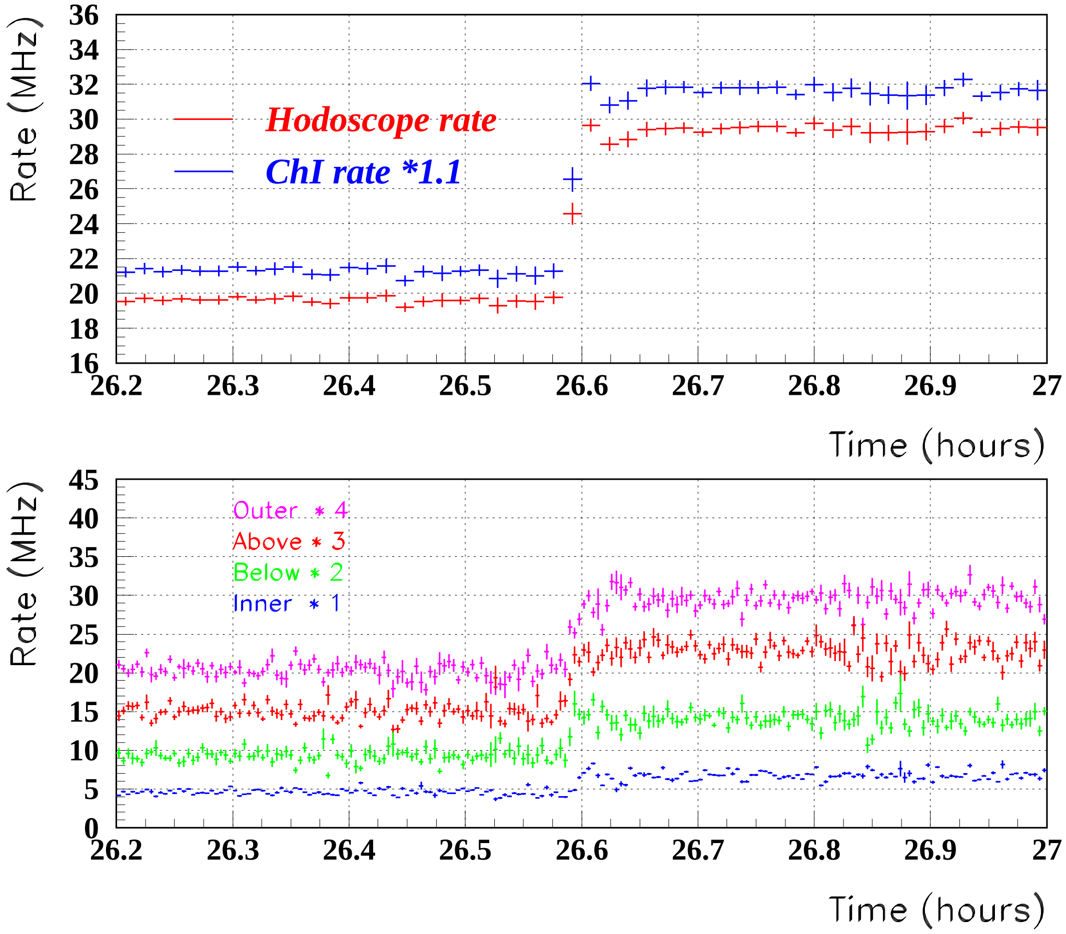

Figure 3.16: *Top: Hodoscope rate and sum of the rates from charge integrators as a function of time. Bottom: rate contribution from the individual wires.*

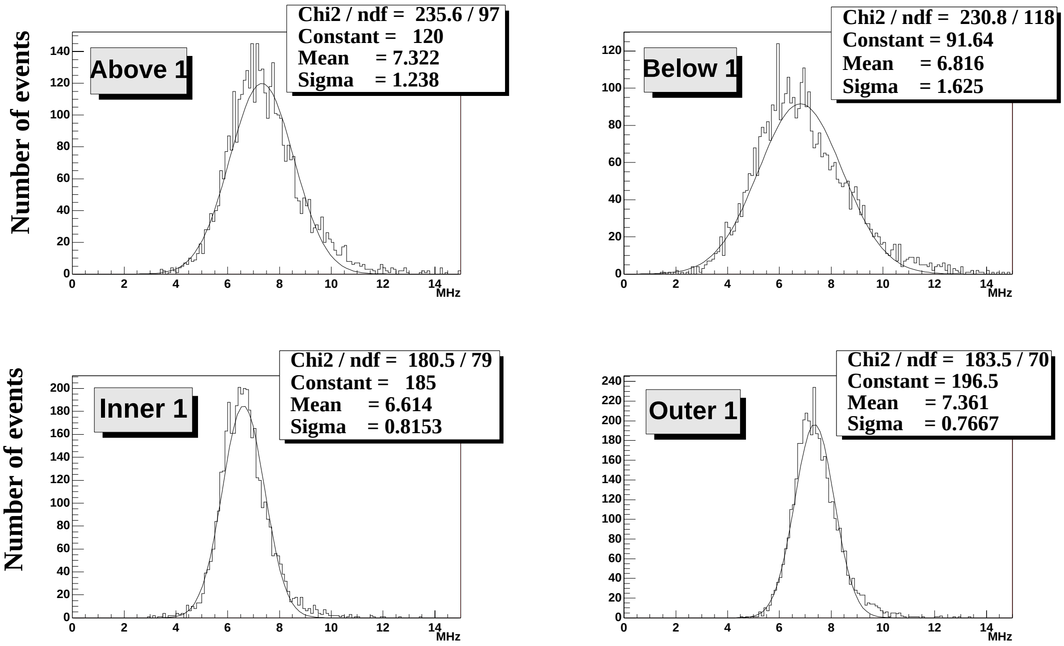

Figure 3.17: *Rate sharing among the wires in the first target station for a run of 30 MHz interaction rate.*

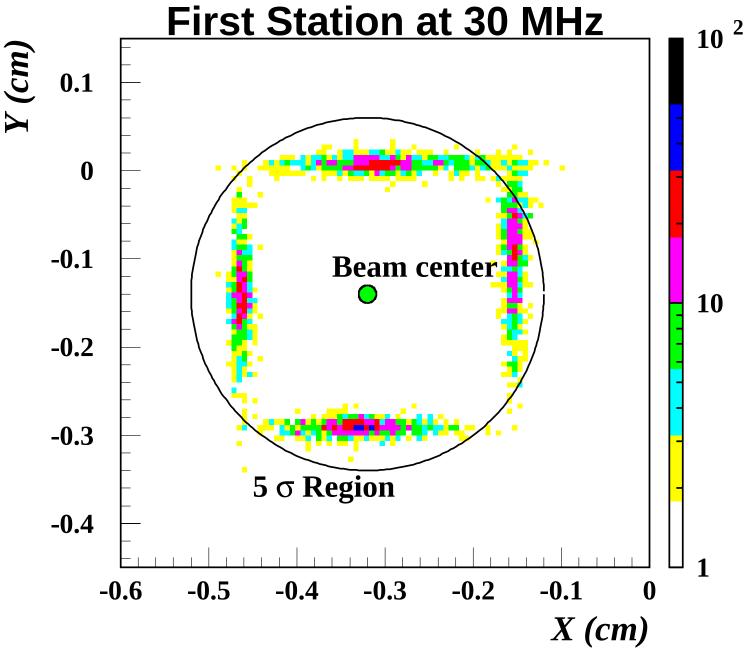

Figure 3.18: *Spatial distribution of reconstructed vertices (in the target plane) for the first target station at 30 MHz interaction rate as reconstructed using VDS tracks.*

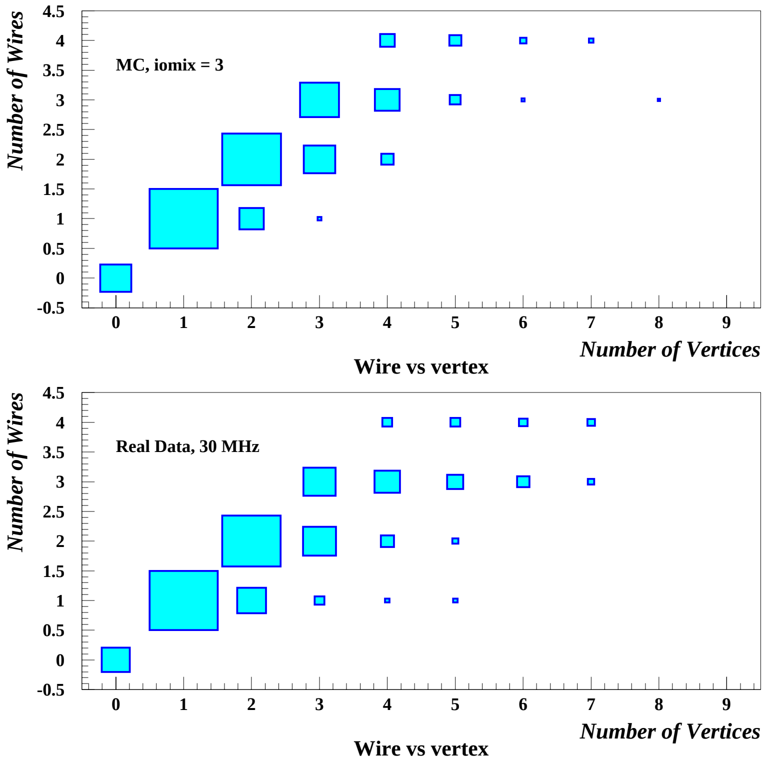

Figure 3.19: *Number of wires on which vertices are found versus the number of the reconstructed vertices for simulated events (top) and real events taken during a run at 30 MHz interaction rate (bottom).*

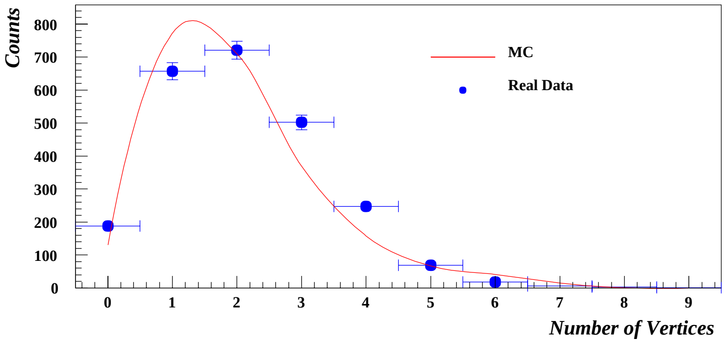

Figure 3.20: *Distribution of the multiplicity of reconstructed vertices, summed over all four wires of the first station, for a run at 30 MHz interaction rate.*

Chapter 4

Measurement of the inclusive π^0 production cross section

4.1 The Spring 99 detector configuration

During the spring of 1999 HERA-B was in a stage of rapid detector assembly. The '99 detector configuration as simulated in the HBGEAN program is displayed in Fig. 4.1. The installation of the RICH counter, the ECAL and the MUON system was completed, although the ECAL and MUON detectors were not fully equipped with readout and pretrigger electronics. Several modules of the tracking system were installed in their final design positions and fully instrumented. The available components of the VDS were arranged as four superlayers. In order to provide maximal overlap with the ECAL area, covered with readout electronics, the quadrants were arranged to form an "L-shape" configuration as shown in Fig. 4.2. Almost all installed detector components were integrated into the common data acquisition (DAQ).

In parallel to the detector assembly, several runs with the high p_T electron trigger were taken. The aim was to test the DAQ and detector performance, take data for detector alignment and prepare for the first physics analyzes. The detector was operated without a magnetic field at small interaction rates (between 2 and 10 MHz) using only one target wire at a time. Data were collected for two types of wires - carbon (inner 2) and titanium (above 1).

The next sections concentrate on the measurement of the cross section for the inclusive π^0 meson production using the ECAL information. Therefore, the ECAL construction and performance will be described in more detail.

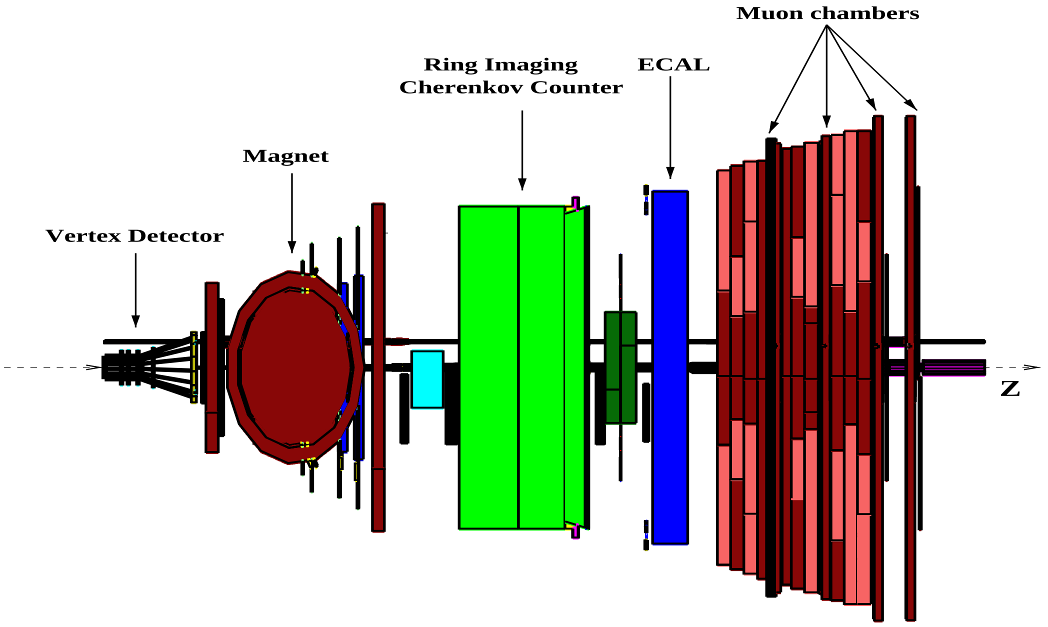

Figure 4.1: *The setup of the HERA-B detector in spring 99 as simulated with GEANT (top view).*

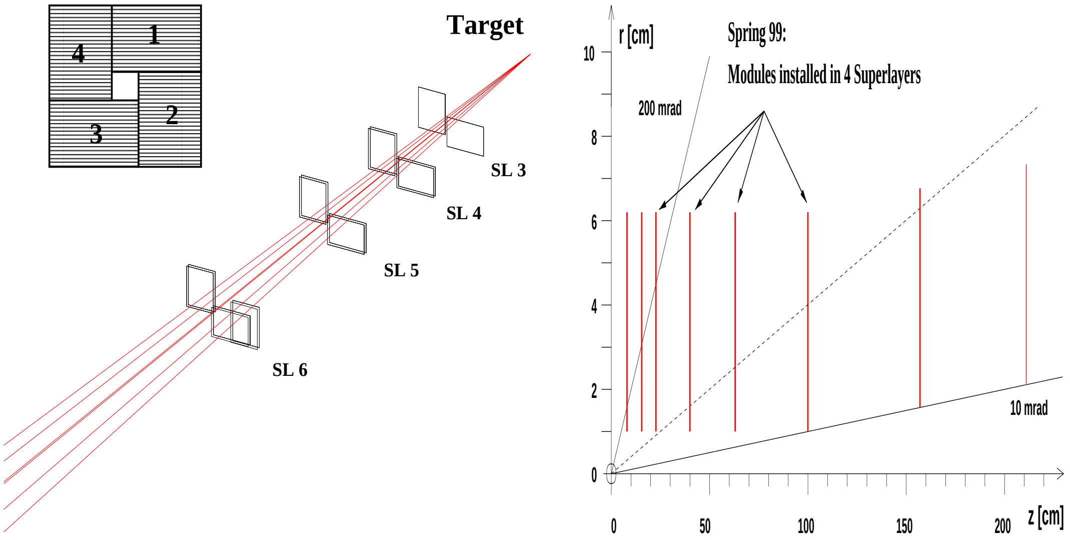

Figure 4.2: *The geometrical layout of the silicon vertex detector in spring 1999. The available quadrants are installed in the position of four superlayers (left). The Z-positions of the superlayers are indicated in the plot on the right side.*

4.1.1 Electromagnetic calorimeter

Construction

The ECAL consists of inner, middle and outer parts. The three sections have different segmentations, granularities are increasing with decreasing distance from the beam pipe. The geometrical layout is presented in Fig. 4.3. Each section is made of an alternating sequence of scintillator/absorber plates which form a sandwich structure. The light is collected by wavelength shifter fibers which run perpendicular to the planes through holes in the module ("shashlik" design), and are connected to photomultipliers as shown in Fig. 4.4. In order to keep occupancies acceptably small, cells with different size are used for each section. To achieve good shower separation and spatial resolution for the given cell sizes, two types of absorber material with different Molière radii, tungsten and lead, are used for the inner and middle/outer sections, respectively. The depth of a given section is also optimized to avoid longitudinal shower energy leakage. The parameters of the ECAL sections are listed in Table 4.1.

	Inner	Middle	Outer
Number of channels	2100	2128	1728
Absorber	Tungsten	Lead	Lead
Molière radius	1.42 cm	4.15 cm	4.15 cm
Cell size	2.24 cm	5.59 cm	11.18 cm
Depth	13 cm (23 X_0)	34 cm (20 X_0)	34 cm (20 X_0)

Table 4.1: *Parameters of the ECAL.*

Calibration

In spring 1999 the ECAL calibration was performed in two steps:

- Since there was no magnetic field, the energy flow had to be symmetric with respect to the beam axis, i.e. all cells at a radial distance R from the beam had to contain the same average energy deposition. The ECAL surface was divided into circular regions around the beam axes. The high voltages of the photomultipliers were tuned to equalize the energy flow within each region.
- The calibration was refined on the basis of the π^0 mass peak, reconstructed from $\pi^0 \to \gamma\gamma$ decays. For each cluster within one region, cell with

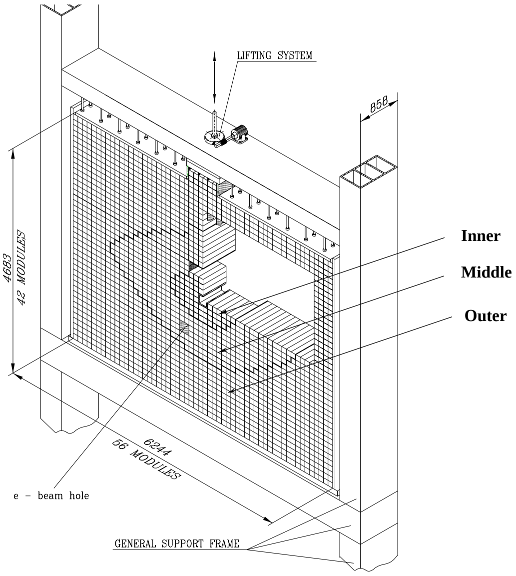

Figure 4.3: *The geometrical layout of the ECAL. There are three sections: inner, middle and outer with different granularities.*

maximal energy deposition was selected. The invariant mass was calculated for all combinations of selected cells, taken from the same region, with clusters from other regions. (Cluster usually consists of several cells. The cluster energy was calculated for a matrix of 3×3 cells with the most energetic cell placed in the center). At the end, the calibration constant for each region was chosen such that the π^0 mass peak moved to the correct position. ECAL calibration was directly done on SLT, so that no data logging was necessary. The calibration procedure was operated iteratively and provided a calibration accuracy of about 5 - 8 % [59, 60].

4.1.2 The trigger system and data acquisition

In the spring of '99 the DAQ and trigger systems were far from the designed configuration. About 25% of the DAQ system, 40 second level trigger nodes, and one PC from the fourth level trigger have been installed. In parallel to the detector installation, several runs with high p_T electron triggers were performed. In this runs the ECAL was used to select candidates for elec-

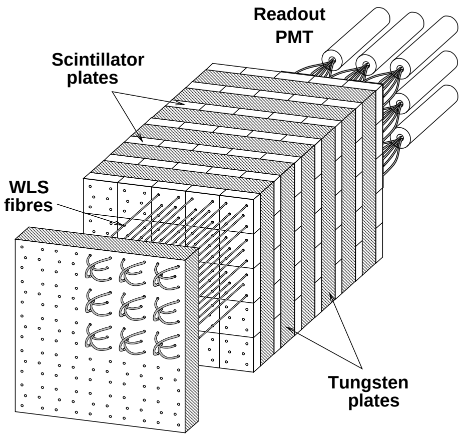

Figure 4.4: *Schematic view of a module from the inner part of the ECAL.*

trons and photons of high transverse momentum. The ECAL was equipped to almost 80 % with readout electronics and with 10 pretrigger boards instrumented in the inner section as shown in Fig. 4.5. The trigger system was organized as follows:

- The ECAL pretrigger was filtering events containing at least one cell with $p_T \geq 1$ GeV/c in the regions shown in Fig. 4.5.
- The FLT hardware was not installed. The FLT functionality was replaced by one emulator test board, the function of which was to send the pretrigger signal to the Fast-Control-System (FCS). The FCS, in turn, pushed data into the Second Level Buffer and notified the second level trigger about new events to process.
- From the SLB the data was transferred to one of the 40 nodes of the SLT PC farm, not currently "busy" with data processing. The online ECAL reconstruction program (CARE) was run on each PC node. On this trigger level the search for two clusters with $p_T \geq 1.1$ GeV/c and an invariant mass above 2.2 GeV was performed. When event was accepted, the event building was performed, and data was sent to the PC farm of the fourth level trigger.
- The accepted event was logged to tape through the fourth level trigger PC farm.

The schematic view of the trigger/DAQ architecture is shown in Fig. 4.6.

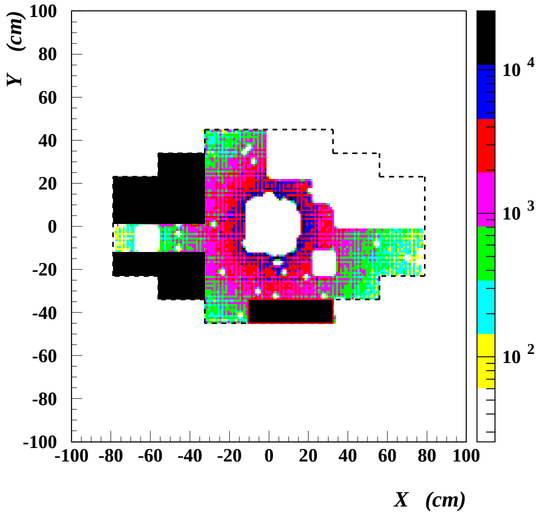

Figure 4.5: *Spatial coverage of the electronics installed in the inner part of ECAL. The dark hatched area shows the locations of the channels corresponding to the 10 pre-trigger boards.*

4.1.3 Measurement of the DAQ efficiency

The performance of the data acquisition is characterized by the efficiency ε_{DAQ}, i.e. the number of triggers acquired by the DAQ divided by the total number of triggers. In the relevant configuration there were the two reasons for losses of trigger candidates, both due to bandwidth limitations in the preliminary DAQ system:

- Limitations from processing speed of the test board. When busy, the board was not able to notify the FCS about pretrigger candidates. This led to losses of pretrigger messages.
- Limitations from data processing speed on the SLT PC farm and low data logging rate to tape. Events are lost as soon as the SLB is completely full. The main limiting factor was the low data logging speed, which amounted to about 30 Hz.

Therefore, the DAQ efficiency can be written in the form

$$\varepsilon_{DAQ} = \varepsilon_{Board}\,\varepsilon_{SLT}, \qquad (4.1)$$

where ε_{Board} is the efficiency of the test board and ε_{SLT} is the efficiency of the SLT and data logging.

The determination of ε_{SLT} was performed using random trigger events. The random triggers were generated with an average rate of about 4 Hz and were acquired in parallel to the high-p_T pretriggered data.

The random trigger events were passed directly to the SLB, therefore they were not sensitive to the dead time introduced by the test board

$$\varepsilon_{DAQ}^{Rand} = \varepsilon_{SLT}. \tag{4.2}$$

The efficiency ε_{SLT} can be calculated, taking into account that the SLT efficiency for both random and high-p_T triggers is the same. The systematic error of ε_{SLT} is estimated to be less then 1% [61].

The study of the properties of the test board, as well as the estimate of ε_{Board} can be found in [61], where, in particular, it was shown that the value of ε_{Board} is about 0.5 and that the uncertainty in ε_{Board} does not exceed 30%. The results on the ε_{Board} calculation for the runs considered for the analysis are listed in Table 4.2.

4.1.4 Luminosity determination and interaction rate calibration

The luminosity determination was performed with the ECAL Energy Sum method, described in Chapter 3. This method was applied to the random trigger events. For each random trigger event the energy deposition was summed over all active cells in the inner part of the ECAL. Then, the energy was averaged over all filled bunches of the whole run. The energy in one interaction, $E^{(1)}$, was determined from a interaction rate scan which had been performed for calibration purposes prior to the physics runs. The same map of active ECAL cells was used for both calibration runs and runs used for analyzes. The average number of interactions and the luminosity were calculated according to equations (3.8) and (3.3). The luminosity determined for further analysis is presented in Table 4.2.

In Section 3.3.4 it was shown, that the systematic uncertainty of the calibration of the ECAL Energy Sum method, i.e. the determination of the energy deposition in single interactions, is about 5%.

The luminosity determined by the ECAL Energy Sum method L_{ECAL} is compared with the luminosity determined using the hodoscope counters L_{HOD} (the average number of interactions obtained from the hodoscope counters has been used for the luminosity calculation using Eq.(3.3)). The ratios

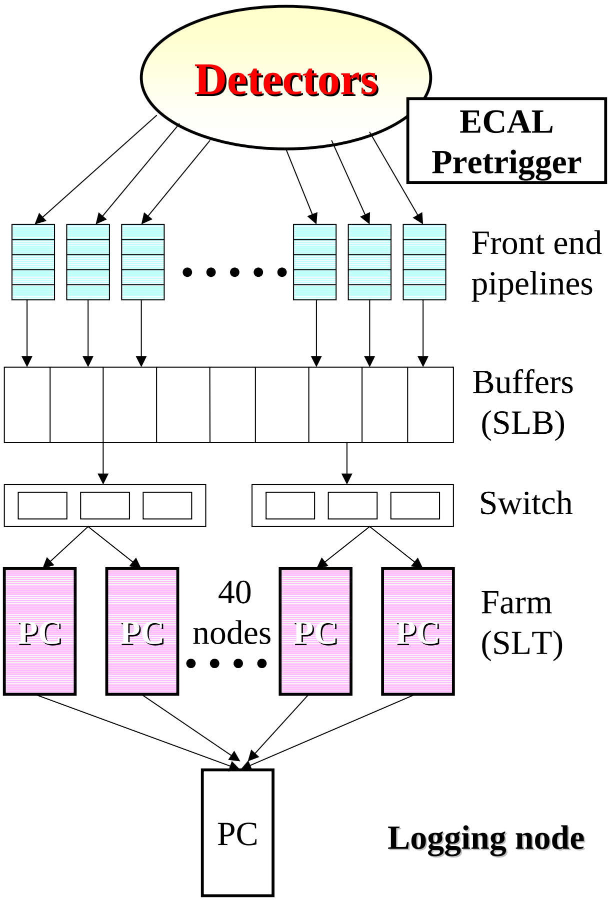

Figure 4.6: *Schematic view of the DAQ/trigger system in the spring of '99.*

of the luminosity obtained from the ECAL methods to the luminosity calculated using the hodoscope counters for runs with the carbon and titanium wires are:

$$\frac{L_{HOD}}{L_{ECAL}}(Carbon) = 1.06 \qquad \frac{L_{HOD}}{L_{ECAL}}(Titanium) = 1.15 \tag{4.3}$$

As can be seen, the L_{HOD} is larger than the L_{ECAL} for both carbon and titanium runs. It could be explained, for instance, by the presence of interactions with unbunched beam protons, so called coasting beam [55][1]. The study of

---

[1] For the interaction rate determination, the hodoscope counters register charged parti-

this effect is not included in the present analysis. Comparing the luminosity determined with the hodoscope counters and the ECAL method indicates the systematic uncertainty of the luminosity determination of about 15%.

As mentioned in Section 3.3.2, hodoscope counters are used for online interaction rate monitoring. In spring 1999 the hodoscope acceptance was, in turn, re-calibrated using the ECAL method. After calibration, acceptance corrections of about 25% had to be applied for the hodoscopes [62]. A large part of these corrections can be explained by the fact that the hodoscope acceptance had not been calibrated since December 99 when the large acceptance hodoscope which had been used for that calibration was removed[2].

---

cles in the whole bunch spacing range of 96 ns [46]. While the ECAL sensitivity is limited to 60 ns. Therefore, in the case of bunch uncorrelated interactions, the interaction rate determined with the hodoscope counters could be larger than the rate observed by the ECAL method.

[2] There was a failure of the power supply for the counter photomultipliers which also affected the value of the hodoscope acceptance.

4.2 High-p_T π^0 production

4.2.1 The data sample and data quality

In this section the measurement of the cross-section for inclusive production of π^0 mesons decaying into two photons is presented. The aim of this study is to investigate the physics capabilities of the HERA-B detector and to test the detector performance rather than to perform a high precision measurement. The analysis is based on the information obtained from the inner part of the ECAL. The experimental setup and trigger configuration are described in Section 4.1. The data sample consists of about $1.5 \cdot 10^6$ events which were acquired for two types of target material: carbon and titanium. The main characteristics of the runs considered for this study are listed in Table 4.2. Before the physics analysis a quality check of the data was performed. The aim of this check was the monitoring of possible appearance of hot (i.e. noisy) towers or failures of modules in the ECAL. For such a check, the total energy released in the inner part of the ECAL and the average number of reconstructed clusters were calculated as a function of the event number. The time evolution of these variables are shown in Fig. 4.7 for runs 4393 and 4437. From this plot, it is clear that the total energy and the number

Carbon (A=12)

Run	Event (10^3)	Overall efficiency	λ ($\bar{N}_{interactions}$)	Lumi/nucleus ($10^{-2} \cdot pb^{-1}$)
4393	212	0.325	0.45	10.4
4424	376	0.3	0.41	15.8
4486	148	0.2	0.64	10.6

Titanium (A=48)

Run	Event (10^3)	Overall efficiency	λ ($\bar{N}_{interactions}$)	Lumi/nucleus ($10^{-2} \cdot pb^{-1}$)
4434	113	0.46	0.14	0.72
4436	71	0.45	0.2	0.62
4437	225	0.46	0.19	1.92
4492	257	0.11	0.61	6.58

Table 4.2: *Overview of runs used in the analysis.*

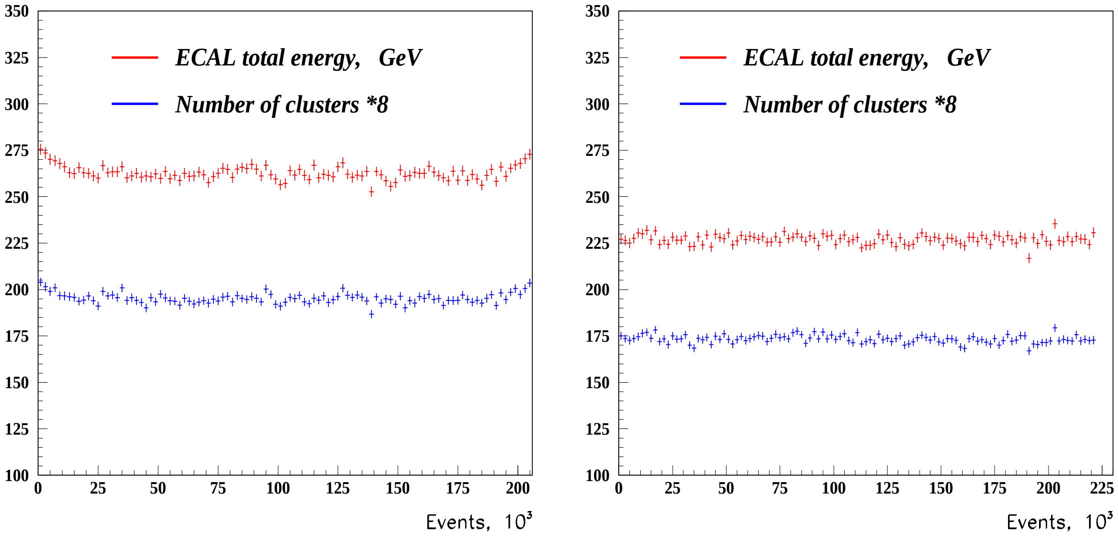

Figure 4.7: *Total energy deposited in the ECAL (upper curve) and the number of clusters (lower curve) as function of the event number for runs 4393 (left) and 4437 (right). The number of clusters is scaled up by a factor of 8.*

of clusters are both constant in time for the entire run, showing no visible signs of any ECAL performance degradation. The average energy is also well correlated with the number of reconstructed particles. Only runs with stable ECAL operation were selected for physics analysis.

4.2.2 Monte Carlo simulation

Event reconstruction

In order to estimate the π^0 trigger and reconstruction efficiencies, and to optimize kinematic cuts, which are important for π^0 background suppression, Monte Carlo simulation has been used. The simulation proceeded as follows:

• Two data samples of $46 \cdot 10^3$ and $11 \cdot 10^3$ events have been produced by the FRITIOF generator using an importance sampling algorithm [6]. The data samples contain at least one π^0 meson per event with $p_T(\pi^0) > 2$ GeV/c and $p_T(\pi^0) > 4.5$ GeV/c, respectively.

• Generated events were passed through the full GEANT detector simulation. The simulated detector geometry, corresponded to the spring 99 detector configuration.

• The ECAL high-p_T pretrigger simulation program [63] has been used to select events which contain a cell in the pretrigger region (see Fig. 4.5) with an energy deposition above a given threshold. The single cell threshold was selected to provide an effective cut $p_T^{cell} > 1.1$ GeV/c according to the map which was used for the "real" data.

• The trigger simulation was based on the online version of the CARE ECAL reconstruction package[3]. The CARE algorithm is performed in three steps [53]:

1. Selection of a cell in the ECAL with an energy deposition above the given threshold. The cell energy is set to 0.8 GeV.
2. Clustering of hit cells.
3. Search of clusters for which the maximal cell energy is above 2.5 GeV. Clusters are assumed to be separated if the energy difference between their peaks is less than 0.5 GeV.

For the trigger simulation program the same CARE parameters (for example energy thresholds) were used as in the online version. The program also applied the map of active channels and calibration parameters which were used in real data and simulated electronic noise. The calibration parameters were smeared by 8%, corresponding to the precision of the calibration as obtained from the measured mass resolution.

The trigger simulation required two ECAL clusters with $p_T \geq 1.1$ GeV/c and with invariant mass $M \geq 2.2$ GeV.

• The offline ECAL reconstruction was also performed with the help of the CARE package.

Cut optimization

In order to reduce the combinatorial background under the π^0 signal, a cut optimization based on the Monte Carlo simulation has been performed. Generated π^0 mesons have been passed through the full HERA-B detector simulation, trigger simulation, and reconstruction chains as was described above. The cuts are selected according to the kinematic distributions of the reconstructed π^0 mesons and their decay products as shown in Fig. 4.8. Due to the

---

[3] As was described in the previous section, the same program was running on one of the SLT PC node.

small trigger and reconstruction efficiencies a large Monte Carlo data sample is needed to study the efficiency dependence on the applied cuts. Therefore, conservative cuts have been used:

- Only clusters with an energy above 5 GeV are considered. The energy distribution of the low energy photons from π^0 decays is shown in Fig. 4.8(a).
- A cut of 20 GeV is applied on the energy sum of the reconstructed pairs. The π^0 energy distribution is shown in Fig. 4.8(b).
- A transverse momentum $p_T^{max} > 1.$ GeV/c of the γ candidate with the highest p_T is required. The p_T^{max} distribution of photons from the π^0 decay is shown in Fig. 4.8(c).
- A cut on the transverse momentum of the π^0 candidate is set to $p_T(\gamma\gamma) = 2$ GeV/c [4].
- The π^0 decay asymmetry, defined by $A = |E_1 - E_2|/(E_1 + E_2)$, with E_1 and E_2 being the energies of the two decay photons, is presented in Fig. 4.8(d). The cut $A \leq 0.85$ is applied.

An example of the influence of the applied cuts on the invariant mass spectra for run 4434 is shown in Fig. 4.9.

The Monte Carlo simulated invariant mass distribution of the reconstructed π^0 mesons for perfect ECAL calibration and 10% calibration accuracy is shown in Fig. 4.10. From this plot it can be concluded that the mass resolutions are about 10.3 MeV and 16.1 MeV for perfect ECAL calibration and 10% calibration accuracy respectively.

As the differential cross section has a steep π^0 transverse momentum dependence, it is very sensitive to the π^0 p_T scale. Residuals of the reconstructed transverse momenta of π^0 mesons, $p_T^{MC} - p_T^{REC}$, are presented in the upper plot of Fig. 4.11 as a function of p_T^{MC}. As can be seen, no bias in the momentum reconstruction is expected up to a p_T of at least 5.5 GeV/c. A small visible deviation between reconstructed and generated momentum in the high p_T region can be explained by overlapping ECAL clusters. This effect will be discussed later. Residuals of the energy determination of photons from the π^0 decay, $E_\gamma^{MC} - E_\gamma^{REC}$, are presented in the middle and lower plots of Fig. 4.11 as functions of the generated transverse π^0 momentum and photon energy, respectively.

The difference between the generated and reconstructed transverse momentum of π^0 mesons integrated over the p_T^{MC} range [2.5 - 6] GeV/c for perfect ECAL calibration and 10% calibration accuracy, is shown in Fig. 4.12.

---

[4] This is mainly done to save computation time.

From the Monte Carlo simulation, the uncertainty in the p_T scale is expected to be less than 2%.

The center of mass rapidity distribution for π^0 mesons on the generator level and after full reconstruction is presented in Fig. 4.13 (the rapidity distribution is arbitrarily normalized). One can see that the rapidity range of reconstructed π^0 mesons is rather narrow and covers mostly positive rapidity values. The small width of the rapidity range is explained by the small acceptance of the installed pretrigger electronics (see Fig. 4.5). In order to eliminate edge effects in the calorimeter the geometrical acceptance is restricted to a c.m.s. rapidity region from -0.05 to 0.55.

4.2.3 Trigger and reconstruction efficiencies

Trigger efficiency

The π^0 trigger and reconstruction efficiencies have been determined using Monte Carlo simulation. The kinematic cuts described in the previous section have been applied in the reconstruction. In the low p_T region, the trigger efficiency can also be measured and then compared with the Monte Carlo simulation, using the random trigger data sample which was acquired in parallel to the high-p_T data. The number of reconstructed events for the random and high p_T trigger samples of a run with an average number of interactions, λ, can be expressed as

$$\begin{aligned} N_{Rand}^{Rec} &\simeq \lambda\, N_{Rand}^{total}\, \varepsilon_{DAQ}^{Rand}\, \varepsilon_{Rec} \\ N_{trig}^{Rec} &\simeq \lambda\, N_{trig}^{total}\, \varepsilon_{DAQ}\, \varepsilon_{Rec}\, \varepsilon_{trig}, \end{aligned} \tag{4.4}$$

where N_{Rand}^{total} and N_{trig}^{total} are the total number of random and high-p_T triggers, or, more precisely, the number of bunch crossings in the random and high-p_T trigger samples. ε_{DAQ}, ε_{DAQ}^{Rand}, ε_{Rec} and ε_{trig} are DAQ, reconstruction and trigger efficiencies, respectively. Taking formula (4.1) and (4.2) for the DAQ efficiency into account, the trigger efficiency can be written in the form

$$\varepsilon_{trig} = \frac{N_{trig}^{Rec}}{N_{Rand}^{Rec}} \frac{N_{Rand}^{total}}{N_{trig}^{total}} \frac{1}{\varepsilon_{Board}}.$$

Due to the small statistics available for the random trigger data sample it is impossible to reconstruct π^0s in the p_T region above 2 GeV/c. Therefore, N_{Rand}^{Rec} and N_{trig}^{Rec} are obtained by summing the number of events within the mass region of [0.1 - 0.17] GeV, assuming that the kinematic distributions for both π^0s and the backgrounds are the same within the given mass region. The resulting trigger efficiency is shown in Fig. 4.14 as a function of the transverse momentum of the reconstructed π^0 mesons. At low p_T, the trigger efficiency is estimated with the random trigger data sample whereas at higher p_T it is obtained by the Monte Carlo simulation. As expected, the trigger efficiency increases rapidly in the p_T range of [1 - 2] GeV/c and almost reaches a plateau at higher transverse momenta. This can be explained by the fact that the p_T trigger threshold was set to 1.1 GeV/c. It can be seen that Monte Carlo simulation and data are in a good agreement in the overlap p_T region around 2 GeV/c.

Overall reconstruction efficiency

The overall trigger and reconstruction efficiency is defined as the number of π^0 mesons which pass the trigger simulation and are reconstructed, divided by the number of generated π^0 mesons. This efficiency is shown in Fig. 4.15 as a function of the transverse momentum of the π^0 mesons. As can be seen, the overall efficiency is about 1% and is almost constant in the whole p_T range up to 5 GeV/c. It decreases in the p_T region above 5 GeV/c. The decrease of the reconstruction efficiency in the high-p_T range can be explained by the fact that the opening angle between two photons from the π^0 decay is getting smaller with increasing transverse momentum of the π^0 meson. This leads to overlapping ECAL clusters and results in a drop of the efficiency. For illustration, the average distance between two ECAL clusters from photons originating from $\pi^0 \rightarrow \gamma\gamma$ decay as a function of the transverse momentum of the π^0 mesons is shown in Fig. 4.16.

Cluster overlaps also lead to overestimates of the photon energies. This can also be observed in shifts of the reconstructed π^0 mass. The effect of overlapping clusters introduces additional systematic errors on the p_T scale. For the p_T range used in this analysis this effect is negligible (as can be also seen from Fig. 4.16), but should be taken into account in the analysis of higher p_T ranges.

Trigger uncertainty

As was described in the previous section, the trigger efficiency is determined from Monte Carlo simulation, where only one interaction per event has been simulated. The ε_{trig} used in Eq.(3.1) is the mean trigger efficiency of a run with the average number of interactions λ, i.e, it should be written in the form which takes multiple interactions into account

$$\varepsilon^{\pi^0}_{trig}(\lambda) = \varepsilon(0)P(0) + \varepsilon(1)P(1) + \varepsilon(2)P(2) + \cdots + \varepsilon(N)P(N),$$

where $\varepsilon(N)$ is the efficiency in N superimposed interactions and $P(N)$ is the probability distribution for the number of interactions with mean λ. As $\varepsilon(N)$ grows with the number of interactions, the mean efficiency also increases with the interaction rate. However, for the runs under consideration, the deviation of the mean efficiency from $\varepsilon(1)$ is expected to be small due to the following reasons:

- The data has been taken at relatively small interaction rates; the value of λ varies between 0.2 and 0.6. The fraction of events with multiple interactions decreases with the decrease of the interaction rate and is proportional to λ (see formula (3.9)). For the interaction rates at which the data were taken, the fraction of events with multiple interactions varies between 10% and 30%.
- The π^0 events are superimposed on inelastic events for which the high p_T trigger efficiency $\varepsilon^{inel}_{trig}$ is several orders of magnitude smaller and is about 10^{-5}.

The study of the trigger efficiency dependence on the number of superimposed interactions, as well as the estimate of the systematic uncertainties of ε_{DAQ}, λ, and N^{Rec}_{trig}, can be done by direct comparison of the number of reconstructed π^0 mesons in runs with different interaction rates. Taking Eq.(4.4) into account, the ratio R of the trigger efficiencies of two runs acquired with the same target material and mean number of interactions λ and λ' can be written as

$$R = \frac{\varepsilon_{trig}(\lambda)}{\varepsilon_{trig}(\lambda')} = \frac{(\lambda\, N^{total}_{trig}\ \varepsilon_{DAQ})'}{\lambda\, N^{total}_{trig}\ \varepsilon_{DAQ}} \frac{N^{Rec}_{trig}}{(N^{Rec}_{trig})'}. \tag{4.5}$$

The ratio R, calculated for runs with the titanium wire, acquired at maximal and minimal interaction rates is presented in Fig. 4.17 as a function of the reconstructed transverse momentum of the π^0 mesons. As can be seen, the ratio is close to unity. This shows that the value of a possible correction to the trigger efficiency due to the multiple interaction dependence is small and lies within the systematic uncertainties of the λ, ε_{DAQ}, and $N^{Rec}_{\pi^0}$ determination.

The ratio R has also been calculated for various run combinations acquired using the same target material. The deviation of R from unity has been found to be always less than 14%.

4.2.4 Data analysis

For the data analysis, the cuts on kinematic variables of photons and π^0 candidates as described in Section 4.2.2 have been applied. The number of π^0 candidates is calculated by fitting the $\gamma\gamma$ invariant mass spectra with a sum of a Gaussian and a polynomial function of third order. π^0 candidates are selected in the invariant mass range corresponding to $\pm 3\sigma$ of the Gaussian distribution. The π^0 background is evaluated by the number of events under the polynomial function and is then subtracted from the total number of π^0 candidates.

The two-photon effective mass spectra averaged over the transverse momentum range [3.0 - 3.25] GeV/c of the reconstructed $\gamma\gamma$ pair and the fit functions for runs with a carbon target are presented in the upper plot of Fig. 4.18. The same distributions are plotted in Fig. 4.19 for different transverse momentum bins. The signal to background ratio with the background determined using the polynomial fit of the invariant mass distribution, is also shown in this plot. The π^0 invariant mass resolution is found to be about 14 MeV. This corresponds to an ECAL calibration precision of about 6% (see Fig. 4.10).

The background estimate has also been performed by using the event mixing technique. The invariant mass is calculated for all combinations of clusters belonging to pairs from different events which pass the kinematic cuts. The invariant mass distribution of mixed events is normalized in the mass region $0.19 < m < 0.3$ GeV. An example of a mixed events spectrum for run 4434 is shown in the lower plot of Fig. 4.18. It can be seen that the invariant mass spectra for non mixed and mixed events are in a good agreement in the regions below and above the π^0 peak. An alternative calculation of the π^0 background has been performed within a $\pm 3\sigma$ mass window around the π^0 peak using the shape of the mixed events spectra.

The number of reconstructed π^0 candidates for carbon and titanium runs for various p_T bins is listed in Table 4.3. In this table, the number of π^0 mesons has been calculated by subtracting the background, obtained from the polynomial fit. For carbon runs, the π^0 statistics is also shown for the case when the background is calculated using the event mixing method. The difference between the number of π^0 candidates obtained for the two types of background subtraction is less then 5% and is used as estimate of the systematic uncertainty in the background subtraction procedure.

p_T GeV/c	2.75-3.	3.-3.25	3.25-3.5	3.5-3.75	3.75-4.	4.-4.5	4.5-5.
Carbon							
π^0, Fit	8539	4716	2516	1288	718	540	124
π^0, Mixed evnt	8763	4684	2507	1323	726	-	-
Titanium							
π^0 (Fit)	6539	3755	1871	987	488	415	82

Table 4.3: *The number of reconstructed π^0 candidates for C and Ti runs for different bins of transverse momentum for the reconstructed π^0 meson. The π^0 background is calculated using the polynomial fit of the invariant mass distribution (Fit) and using the event mixing method (Mixed evnt).*

Fig. 4.20 shows the mean value of the reconstructed π^0 mass as function of the energy of the most energetic photon from the π^0 decay, E_γ^{max}, and the transverse momentum of the π^0 mesons. As can be seen, the mean value of the reconstructed π^0 mass is almost constant in the whole E_γ^{max} and p_T ranges. The measured π^0 mass is compatible with the world average to the level of $< 2\%$. This justifies the reliability of the Monte Carlo prediction on the stability of the π^0 transverse momentum scale (see Fig 4.11).

4.2.5 Cross section calculation

Taking the branching fraction $\mathrm{Br}(\pi^0 \rightarrow \gamma\gamma) = 0.988$ into account and assuming a linear dependence of the cross section on the atomic number A, the invariant cross section for π^0 meson production can be written according to Eq.(3.1) as

$$E\frac{d^3\sigma}{d^3p} = \frac{N_{\pi^0}}{2\ \pi\ A\ \triangle y\ p_T\ \triangle p_T\ \varepsilon_{DAQ}\ \varepsilon_{Overall}\ Br(\pi^0 \rightarrow \gamma\gamma)}\frac{1}{L}. \tag{4.6}$$

The number of π^0 candidates, N_{π^0}, the values of luminosity, L, and DAQ efficiency, ε_{DAQ}, used for the calculation of the cross section are listed in Table 4.3 and Table 4.2, respectively. The overall trigger and reconstruction efficiency, $\varepsilon_{Overall}$, is obtained from a fit of the distribution presented in

Fig. 4.15 by a straight line in the transverse momentum range of $2.5 < p_T < 5$ GeV/c. It is found to be equal to $(99 \pm 6) \cdot 10^{-3}$.

The cross sections per nucleon for pC and pTi interactions averaged over the rapidity range $-0.05 < y_{C.M} < 0.55$ are presented in Fig. 4.21 and listed in Table 4.4 as function of the π^0 transverse momentum. The π^0 cross section measured by the Fermilab experiment E706 [64] for 800 GeV pBe interaction is also shown in Fig. 4.21 for comparison. The error bars shown in this plot are statistical only. The systematic errors in the cross section are:

• The uncertainty in the luminosity determination. As was discussed in Section 4.1, this uncertainty amounts to about 15%.

• The error in the DAQ dead time determination. It is expected to be about 30%, due to the poor knowledge of the test board efficiency [61] (see Section 4.1). This error contributes as the main source of the systematic uncertainty in the overall normalization.

• The uncertainties in the π^0 background subtraction. They are calculated for each π^0 transverse momentum bin and are estimated to be less than 5%. written • The Monte Carlo statistical errors in the calculation of the trigger and reconstruction efficiencies. They amount to less than 10%.

• The p_T scale uncertainty of less than 2%.

p_T (GeV/c)	$p + C \to \pi^0 + X$ $nb/(GeV/c)^2$	$p + Ti \to \pi^0 + X$ $nb/(GeV/c)^2$
2.75 - 3.0	261.8 ± 2.8	234.4 ± 2.9
3.0 - 3.25	133.1 ± 1.9	123.8 ± 2.0
3.25 - 3.5	65.7 ± 1.3	57.1 ± 1.3
3.5 - 3.75	31.3 ± 0.9	28.1 ± 0.9
3.75 - 4.0	16.3 ± 0.6	12.9 ± 0.6
4.0 - 4.5	5.6 ± 0.2	5.0 ± 0.3
4.5 - 5.0	1.3 ± 0.1	1.0 ± 0.1

Table 4.4: *Invariant cross section* $E\frac{d^3\sigma}{d^3p}$ *for the inclusive reactions* $p + C \to \pi^0 + X$ *and* $p + Ti \to \pi^0 + X$ *averaged over the rapidity range* $-0.05 < y_{C.M.} < 0.55$. *The cross sections are calculated per nucleon according to Eq.(4.6). Errors are statistical only.*

A qualitative comparison of the cross sections for two beam energies, 800 and 920 GeV, has been performed using the Monte Carlo simulation. Two data samples corresponding to these energies have been generated with the

PYTHIA event generator using the $CTEQ2$ parton distribution functions [5]. The ratio of the invariant cross sections obtained for 800 GeV and 920 GeV protons as a function of transverse momentum of the π^0 mesons, is presented in Fig. 4.22. From this plot it can be seen that the ratio of cross sections is increasing with increasing transverse momentum of the π^0 mesons. This means that the shape of the cross section is expected to be steeper for the beam energy of 800 GeV. In this simulation, the default PYTHIA settings for primordial k_T distribution of partons inside hadron have been used. Two-dimensional k_T distribution has a Gaussian form with $\sigma = 0.44$ GeV and the average of the squared transverse momentum $\langle k_T^2 \rangle = (0.44\ \mathrm{GeV/c})^2$ [49]. As was described in [1], the k_T smearing was introduced in order to describe the transverse components of initial-state parton momenta, which could be initiated due to the initial-state soft-gluon radiation . This k_T smearing modifies both the shape and normalization of the inclusive cross section.

4.2.6 A - dependence

Traditionally, the cross sections are calculated per target nucleon. However, effects such as nuclear shadowing or secondary scattering in the nucleus can result in deviations of the cross sections from the linear dependence on the nucleon number [65]. The form A^α, with α being a parameter that can depend on rapidity, transverse momentum, and on the nature of the studied particle is often used to parameterize the A dependence. Taking into account that trigger and reconstruction efficiencies are the same for carbon and titanium runs, according to Eq.(3.1), the exponent α can be determined from the following equation

$$\left(\frac{A^C}{A^{Ti}}\right)^\alpha = \frac{N^C_{\pi^0}}{N^{Ti}_{\pi^0}} \cdot \frac{(L\ \varepsilon_{DAQ})_{Ti}}{(L\ \varepsilon_{DAQ})_C}, \tag{4.7}$$

where A is the atomic number, N_{π^0} is the number of pions, L is the luminosity, and $\varepsilon_{DAQ} = \varepsilon_{Board}\ \varepsilon_{SLT}$ is the DAQ efficiency (see Eq.(4.1)) for carbon and titanium runs.

The parameter α derived from Eq.(4.7) is shown in Fig. 4.23 as function of the transverse momentum of the π^0 meson. It can be seen that the value of α is almost constant in the whole p_T range and is about 0.95. The errors shown in the plot are statistical.

As was described in Section 4.2.3, the deviation from unity of ratios of the trigger efficiencies calculated according to Eq.(4.5) for runs, acquired

p_T GeV/c	α	$\alpha_{Fermilab}$[7]
2.75 - 3.0	$0.95 \pm 0.01 \pm 0.14$	–
3.0 - 3.25	$0.98 \pm 0.02 \pm 0.15$	–
3.25 - 3.5	$0.93 \pm 0.02 \pm 0.14$	–
3.5 - 3.75	$0.95 \pm 0.03 \pm 0.14$	–
3.75 - 4.0	$0.87 \pm 0.04 \pm 0.13$	–
4.0 - 4.5	$0.95 \pm 0.05 \pm 0.15$	1.07 ± 0.03
4.5 - 5.0	$0.85 \pm 0.10 \pm 0.13$	1.10 ± 0.04
2.75 - 5.0	$0.95 \pm 0.01 \pm 0.14$	

Table 4.5: *Nuclear dependence exponent α obtained from the measured inclusive π^0 cross section for pC and pTi interactions, averaged over $-0.05 < y_{C.M} < 0.55$. The measurements of the experiment E706 [7] at 800 GeV beam energy, using pBe and pCu interactions and averging over $-0.7 < y_{C.M} < 0.7$ are also shown.*

at different interaction rates using the same target material, does not exceed 14%. This deviation can be mainly explained by the dependence of the ε_{Board} on the average number of interactions λ [5]. The deviation was used for the calculation of the systematic error on α, which was found to be 11%.

As was described in Section 4.1.4 the systematic uncertainty of the luminosity determination does not exceed 15%. Therefore, the upper limit for the systematic error on α is estimated to be about 15%.

The results are directly compared with the fixed target Fermilab experiment E706 [7] which was operating with a 500 GeV proton beam incident on Be and Cu targets and spanned rapidity range $-0.7 \leq y_{C.M} \leq 0.7$. The results are presented in Table 4.5.

4.3 Summary

A first attempt to measure the cross section of inclusive production of π^0 mesons decaying into two photons using the HERA-B detector was presented. The π^0 cross section was determined using the information from the inner

---

[5] The estimation of the DAQ efficiency (see Eq.(4.1)) has been performed assuming that the test board efficiency was constant, i.e. it was independent of the interaction rate in the range where the data were taken [61]

part of the ECAL for two types of target material, carbon and titanium, in the transverse momentum range of $2.75 < p_T < 5.0$ GeV/c and the center of mass rapidity range of $-0.05 < y_{C.M.} < 0.55$.

The cross section analysis consisted of the following main steps:

- The luminosity determination was performed using the ECAL Energy Sum method.
- A detailed quality check was performed for the ECAL data for all runs considered in the analysis.
- The trigger and reconstruction efficiencies for π^0 production were estimated using Monte Carlo simulation. Due to the invariant mass cut of 2.2 GeV on the trigger level the overall efficiency was found to be small, about 1%.
- The background underneath the π^0 mass peak was subtracted using two independent methods, one based on a polynomial fit of the background spectrum, the other based on event mixing techniques.

Various sources of systematic uncertainties, such as luminosity determination, DAQ efficiency, π^0 background subtraction and stability of the π^0 p_T scale were analyzed. The systematic uncertainty of the DAQ test board efficiency of about 30% contributes as the main source of the systematic errors in the overall cross section normalization[6]

The π^0 cross sections per nucleon were fit for the two target materials using a functional dependence A^α. The exponent α was measured to be $0.95 \pm 0.01 \pm 0.14$. The value of α obtained from the measured by the Fermilab experiment E706 inclusive π^0 cross section for pBe and pCu interactions, averaged over rapidity and p_T ranges $-0.7 < y_{C.M} < 0.7$ and $4.0 < p_T < 6$ GeV/c, is 1.08. Within the systematic error it is in a good agreement with the measurement presented in this work.

The present analysis illustrates a remarkably good understanding of the detector performance during the early stage of the HERA-B commissioning. It also demonstrates the high potential for HERA-B to perform inclusive π^0 (and direct photon) cross section measurements.

---

[6] As was mentioned in Section 4.1.3, the test board was used to replace the FLT functionality in the preliminary DAQ system. The systematic uncertainty of the DAQ efficiency for the complete DAQ system is small.

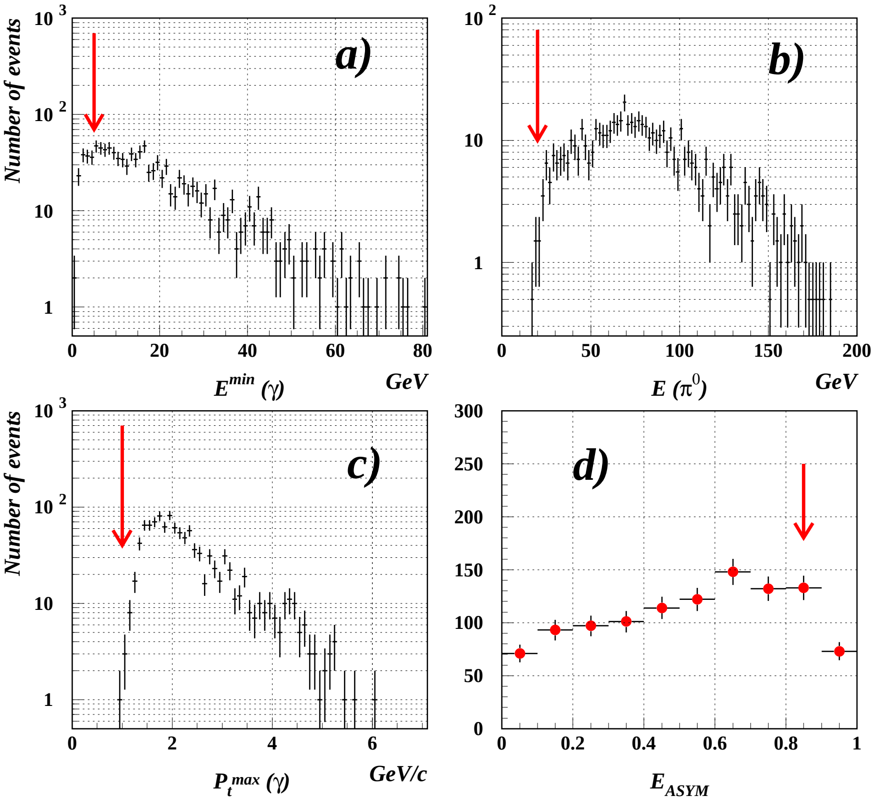

Figure 4.8: *The kinematic distributions of the reconstructed* π^0 *mesons and their decay products. Applied cuts are marked with arrows. a) Energy distribution of the low energy photons. b)* π^0 *energy distribution. c) The* p_T^{max} *distribution of photon candidates. d) Distribution of two-photon energy asymmetry,* $A = |E_1^\gamma - E_2^\gamma|/(E_1^\gamma + E_2^\gamma)$.

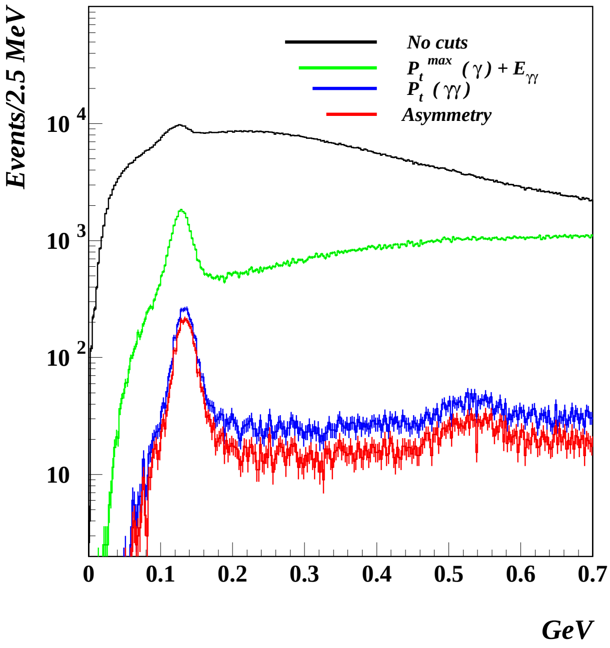

Figure 4.9: *Run 4434. Invariant mass distribution for various kinematic cuts.*

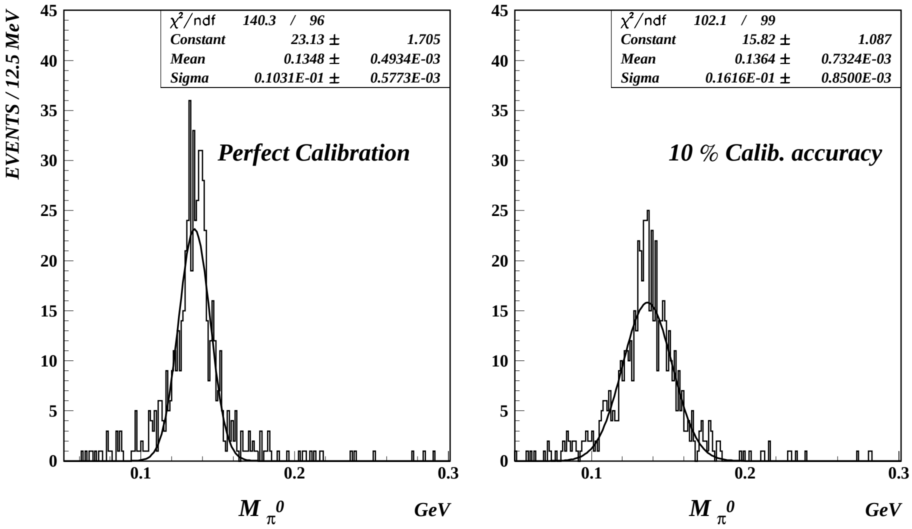

Figure 4.10: *Monte Carlo simulation. Invariant mass distribution for reconstructed* π^0 *mesons for perfect ECAL calibration and 10 % calibration accuracy.*

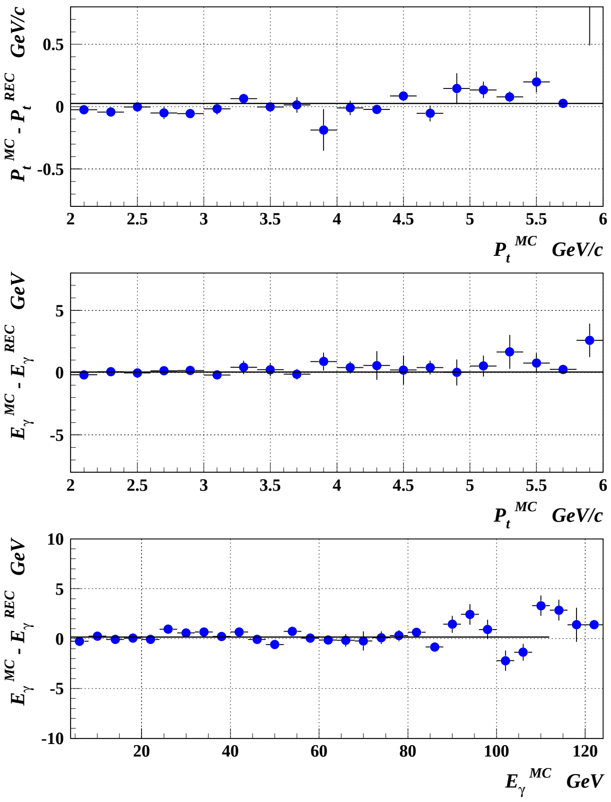

Figure 4.11: *Top: Mean difference between the generated and reconstructed transverse momentum of* π^0 *mesons as function of the generated* p_T^{MC}*. Middle and Bottom: Mean residuals of the energy determination of photons from* π^0 *decays,* $E_\gamma^{MC} - E_\gamma^{REC}$*, as function of the generated* π^0 *transverse momentum and of the photon energy.*

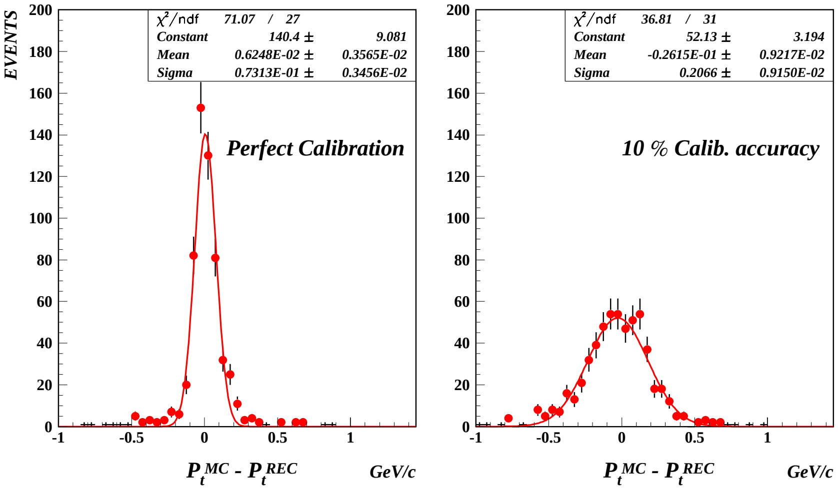

Figure 4.12: *Residual distribution for the transverse momenta of π^0 mesons for all generated π^0 mesons in the range $p_T^{MC} \in [2.5 - 6]$ GeV/c, assuming perfect ECAL calibration (left) and calibration accuracy at a level of 10 % (right).*

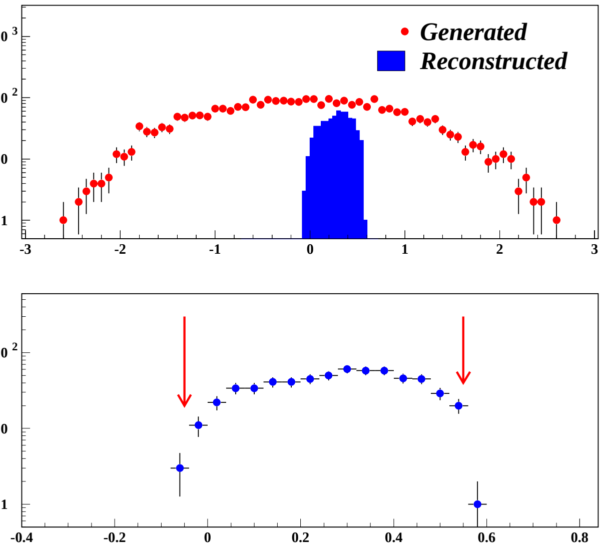

Figure 4.13: *Rapidity distribution for* π^0 *mesons on the generator level and after reconstruction. The distributions are arbitrary normalized (top). The lower plot shows a blow-up of the rapidity distribution for the reconstructed pions. Arrows indicate the range used for the cross section calculation.*

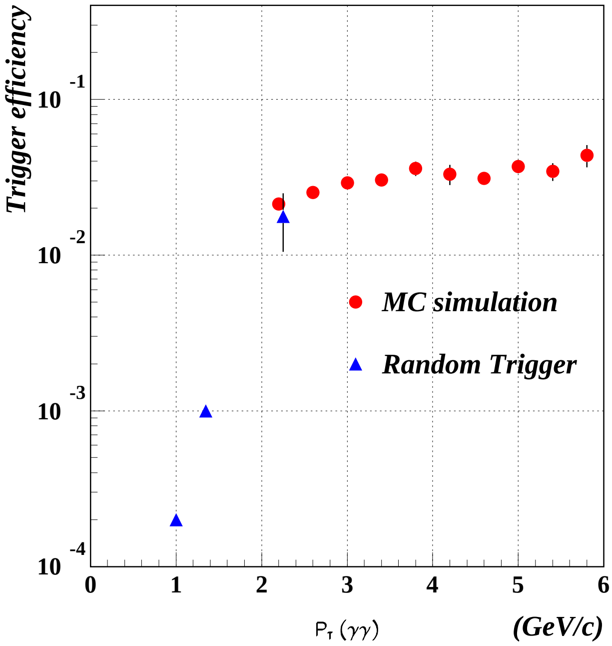

Figure 4.14: π^0 *trigger efficiency calculated from Monte Carlo simulation (circle) and measured using the random trigger (triangle) as function of the* π^0 *transverse momentum.*

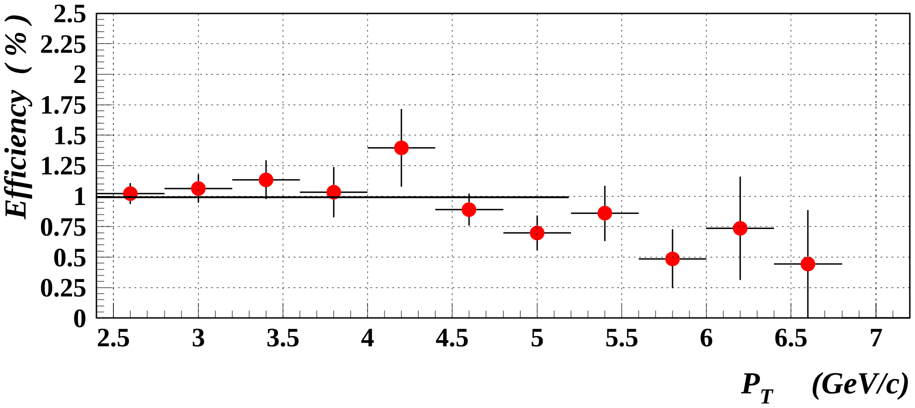

Figure 4.15: *Overall trigger and reconstruction efficiency as function of the transverse momentum of the* π^0 *mesons.*

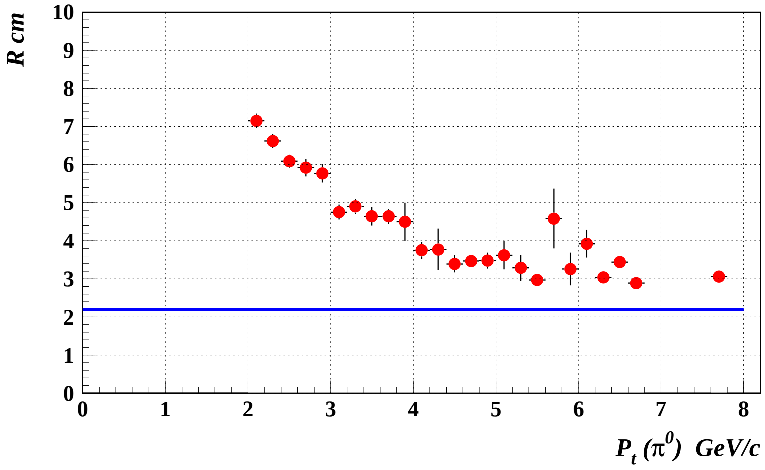

Figure 4.16: *Average distance between two ECAL clusters from photons originating from $\pi^0 \rightarrow \gamma\gamma$ decays as function of the transverse momentum of the π^0 meson. The solid line indicates the cell size.*

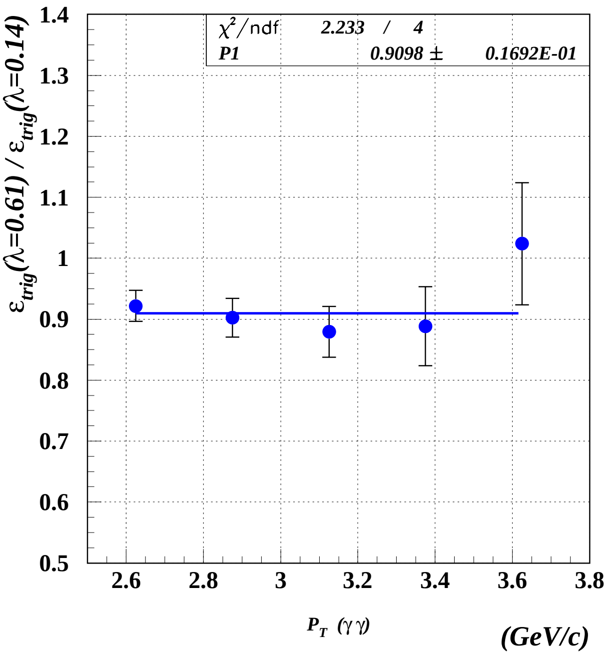

Figure 4.17: *Ratio of the reconstruction efficiencies for runs acquired with the interaction rates corresponding to* $\lambda = 0.61$ *and* $\lambda = 0.14$*, as function of the transverse momentum of the reconstructed* π^0 *mesons.*

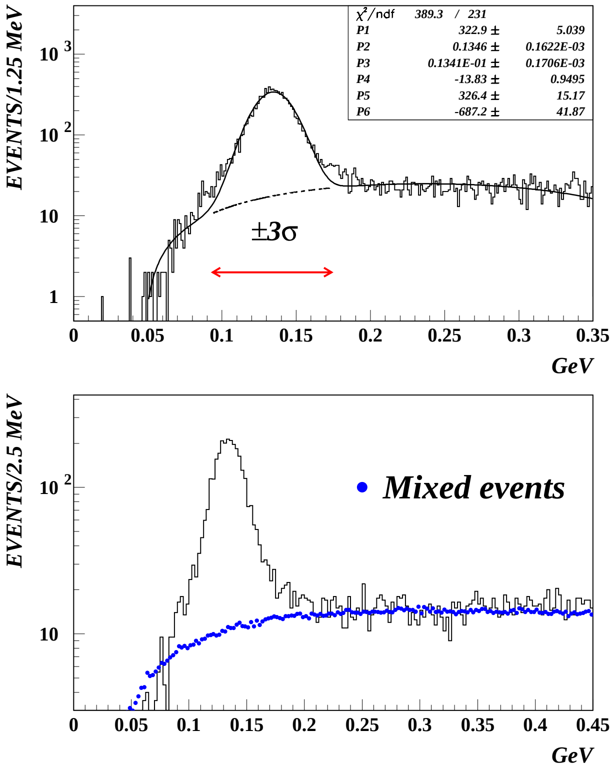

Figure 4.18: *Two-photon invariant mass spectra of all runs with a carbon wire for the transverse momentum range [3.0 - 3.25] GeV/c. The fit of the mass spectrum with the sum of a Gaussian and a third order polynomial function is superimposed in the upper plot. The invariant mass distribution together with a spectrum from mixed events for run 4434 is shown in the lower plot.*

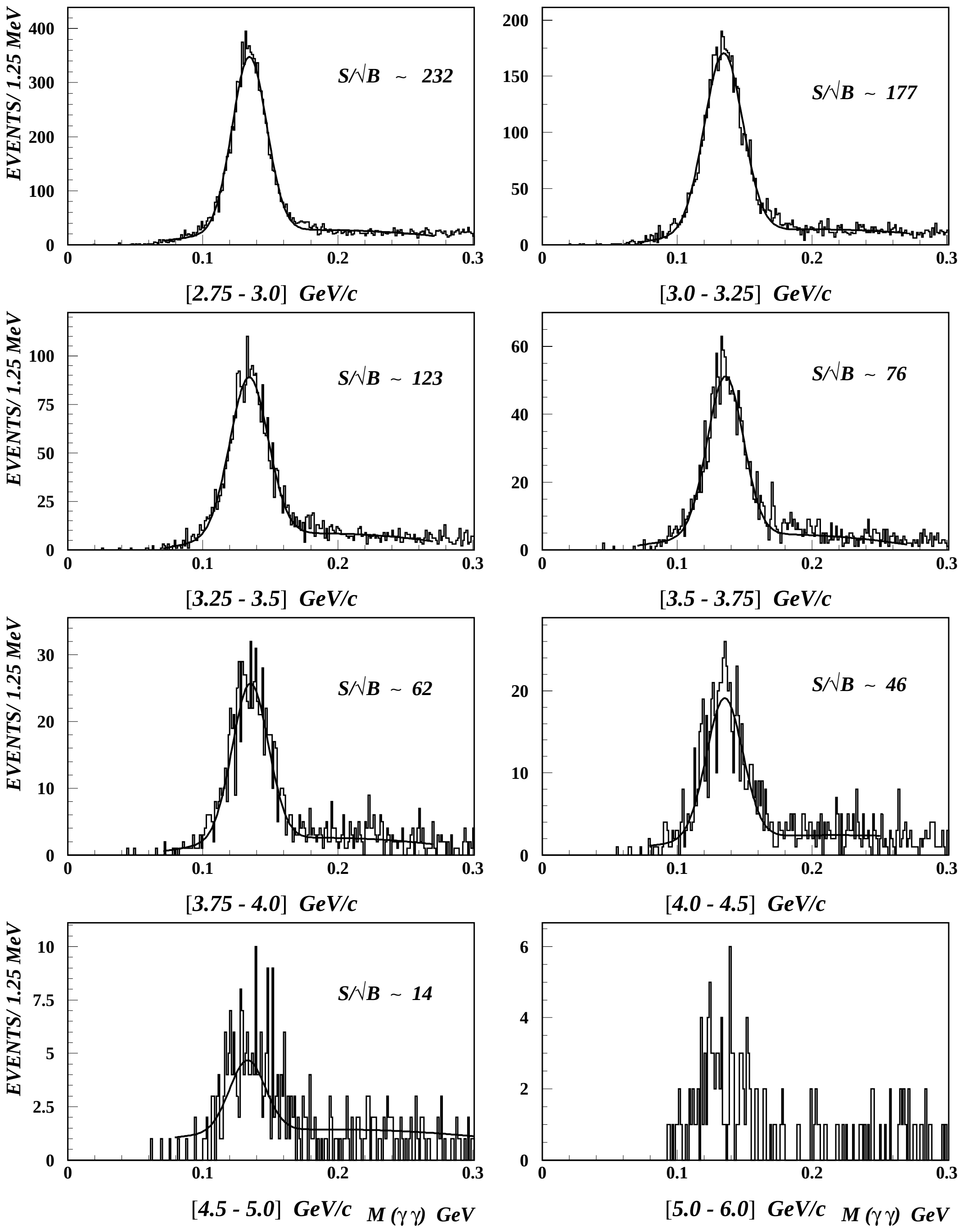

Figure 4.19: *Two-photon effective mass spectra summed in various bins of transverse momentum for the reconstructed photon pair for all runs using the carbon wire.*

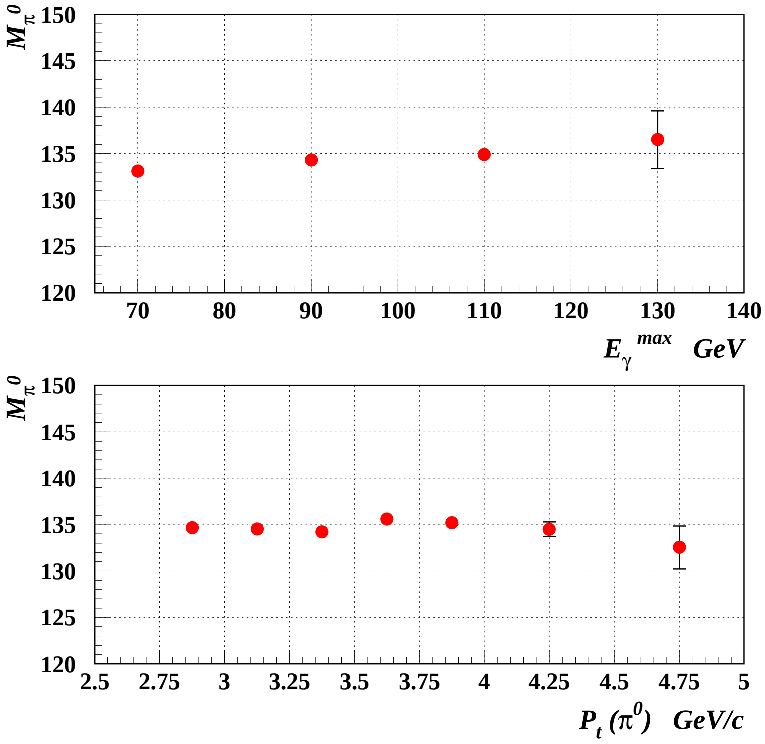

Figure 4.20: *Mean value of the reconstructed π^0 mass as function of the energy of the high energetic photon from the pion decay (top) and the transverse momentum of the π^0 mesons (bottom) for runs with the carbon wire.*

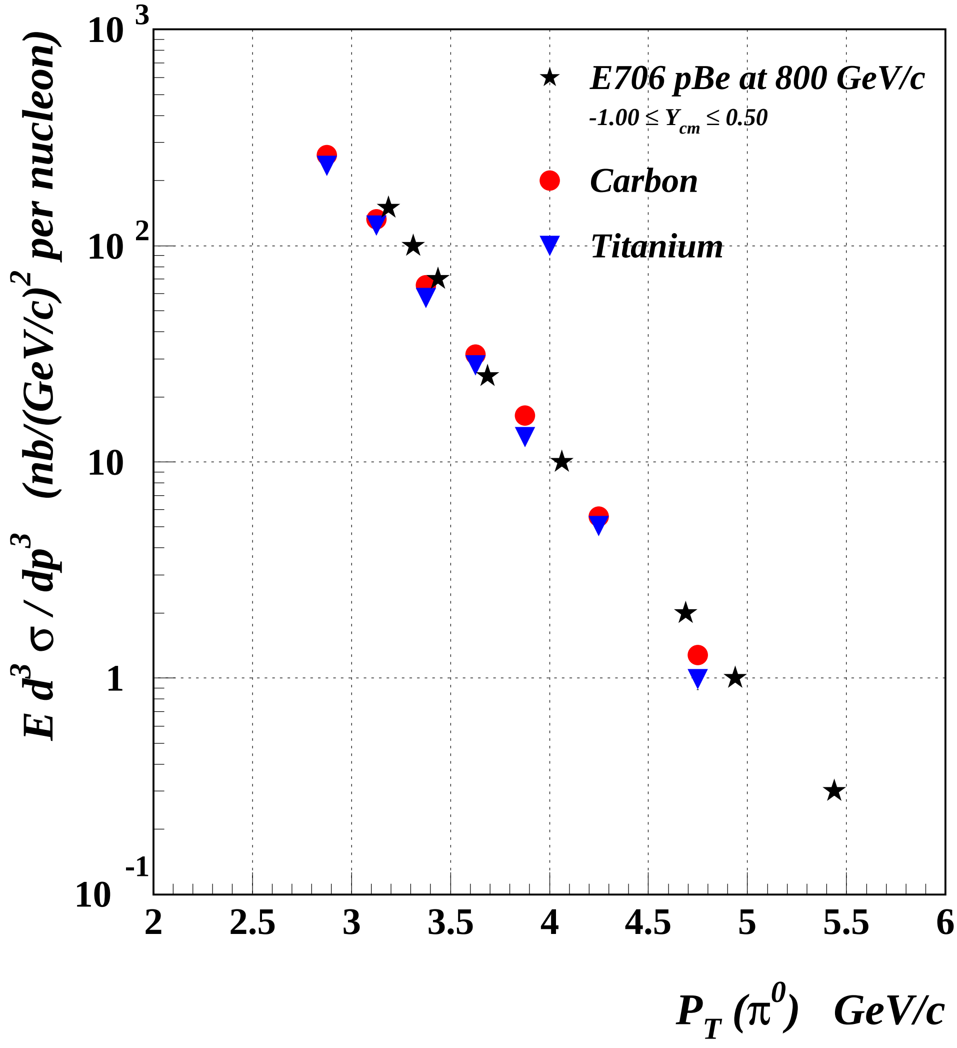

Figure 4.21: *Invariant cross sections per nucleon for inclusive* π^0 *meson production on carbon and titanium. The cross sections are shown versus* p_T *averaged over the rapidity range* $-0.05 < y_{C.M.} < 0.55$. *The invariant cross section measured by the Fermilab experiment E706 at 800 GeV pBe interactions averaged over the rapidity range* $-1 < y_{C.M.} < 0.5$ *is shown for comparison.*

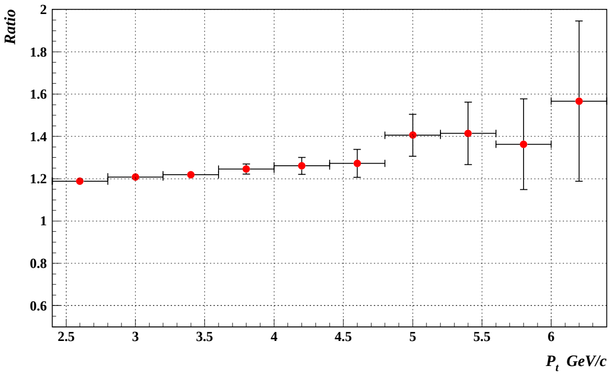

Figure 4.22: *Ratio of the invariant cross sections for two proton beam energies 920 and 800 GeV. Cross sections are calculated on the basis of the PYTHIA generator using the CTEQ parton distribution functions [5].*

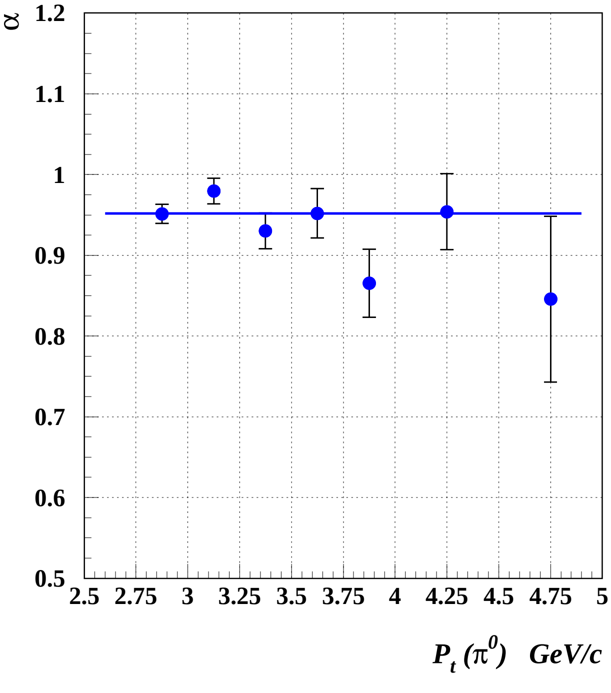

Figure 4.23: *Nuclear dependence exponent α obtained from the measured inclusive π^0 cross section for pC and pTi interactions, averaged over $-0.05 < y_{C.M} < 0.55$.*

Chapter 5

Expectations for HERA-B

Among the physics goals of Hera-B the study of hadronic production of dileptons in the high-mass region seems to be one of the most interesting topics to be explored, since it is a sensitive probe to test the internal structure of hadrons with heavy quarks. As was described in Chapter 1, the investigation of the production of Υ mesons is of particular interest because the measurement of Υ polarization allows to distinguish between different mechanisms of heavy quarkonium production.

The aim of this analysis is to evaluate the observability of Υ resonances in the dilepton final state and to demonstrate the feasibility to perform accurate measurements of Υ polarization. In this chapter the emphasis will be put on the muon channel. The analysis of the electron channel has been performed in reference [66].

The feasibility to measure the rate of Υ production for various detector configurations has been studied by the author in reference [67][1].

5.1 Υ reconstruction

The acceptance for Υ production and the mass resolution in the Υ mass region are determined using a detailed HERA-B detector simulation [51]. The production of Υ resonances has been implemented in PYTHIA in analogy to the J/ψ production algorithm provided by the standard version of PYTHIA by simply replacing the charm quark mass by the b quark mass at

---

[1] At the time when this work has been done the HERA-B detector design allowed for some modifications.

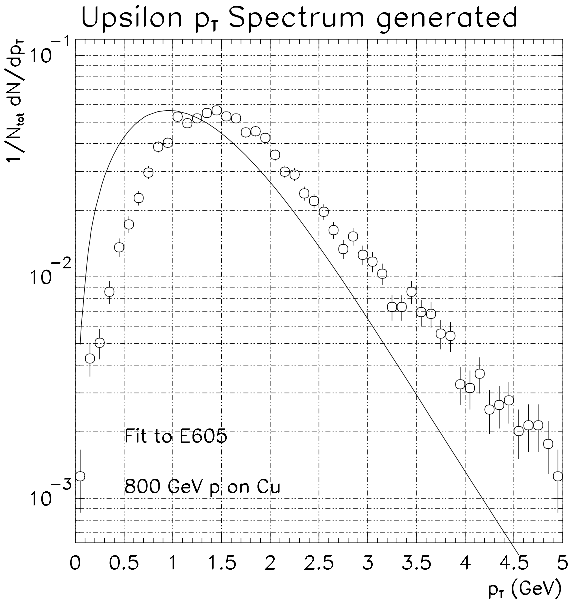

Figure 5.1: *Transverse momentum spectra of* Υ *mesons from the HERA-B implementation of* Υ *production in PYTHIA for 800 GeV protons. Superimposed is the fit to the data of the E605 experiment. This plot is taken from [6].*

the subprocess level. Fig. 5.1 represents the spectrum of Υ resonances as was implemented in HERA-*B* event generator together with the fit to the E605 data [6]. As can be seen, the Monte Carlo predictions are below the fit to the experimental data for small transverse momenta. A small difference in slope at large p_T is also visible. In this analysis we concentrate on the study of the reconstruction efficiency and the acceptance of Υ mesons. It will be shown, that the reconstruction efficiency for Υ mesons is almost constant in the whole range of the transverse momentum of the Υ mesons (see Fig.5.3). Therefore, corrections for the reconstruction efficiency and the acceptance related with subtleties in the event generations are expected to be small[2]

Generated events were processed through the simulation of the full detector. The events were passed through the trigger simulation and then were

---

[2] In the present version of event generators for HERA-*B* [6] there is a possibility to weight p_T and x_F inclusive spectra generated by PYTHIA according to, for instance, measured spectra of p_T and x_F.

reconstructed with the HERA-B standard reconstruction program [68]. The reconstruction included pattern recognition in the outer tracker and the VDS, the track segment matching, and the fit of Υ decay vertices. In the trigger simulation and the reconstruction phases, the following kinematic cuts have been applied:

• Trigger:	$p_T(\mu) > 0.5$ GeV/c.
• Trigger:	$p(\mu) > 5$ GeV/c.
• Geometry:	$dp/p^2 < 0.01$/GeV/c.
• Reconstruction of Υ :	$\chi^2(vertex) < 10$.
• Reconstruction of Υ :	$\lvert m(\mu^+\mu^-) - m(\Upsilon)\rvert < 400$ MeV.

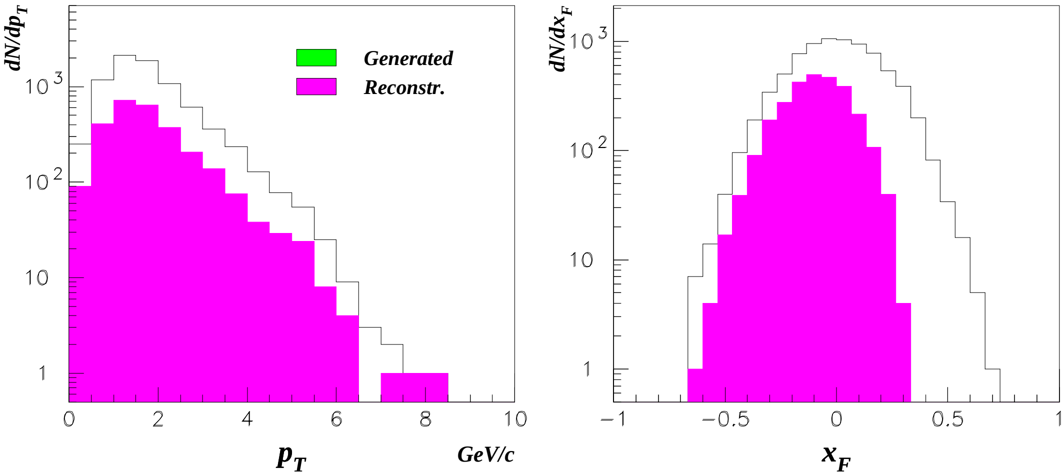

Figure 5.2: *Transverse momentum and x_F distribution for Υ mesons decaying into muon pairs. Generated events are represented as open histograms, accepted by the outer tracker reconstruction by shaded histograms.*

The phase space distributions for Υ mesons on the generator level and after being reconstructed in the outer tracker [67] are presented in Fig. 5.2. The asymmetric acceptance in x_F can be explained by the absence of inner tracker in this simulation. The acceptance (the number of reconstructed Υ mesons divided by the number of generated Υ mesons) as a function of the transverse momentum of the Υ mesons is shown in Fig. 5.3. As can be seen, the acceptance varies slowly over the entire spectrum of p_T, covering most of the highly populated dynamic range. The invariant mass distribution of the reconstructed Υ mesons is shown in Fig. 5.4. The relative mass resolution of

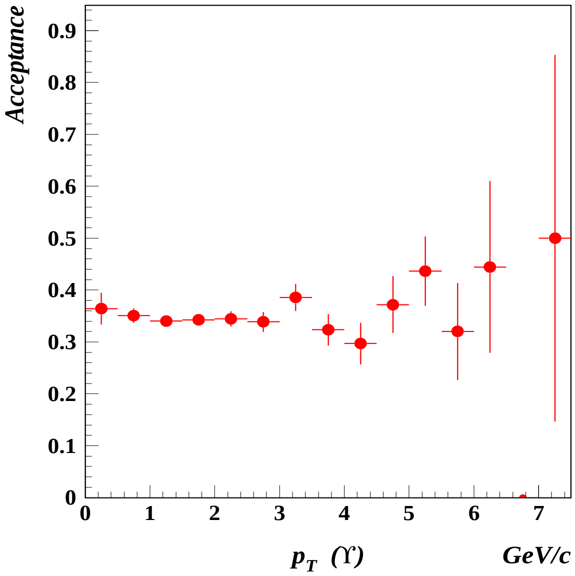

Figure 5.3: *Acceptance for* Υ *mesons decaying into muon pairs as a function of the* Υ *transverse momentum, when reconstructed in the outer tracker (inner tracker missing).*

the reconstructed $\Upsilon(1S)$ resonance is about 1.1%.

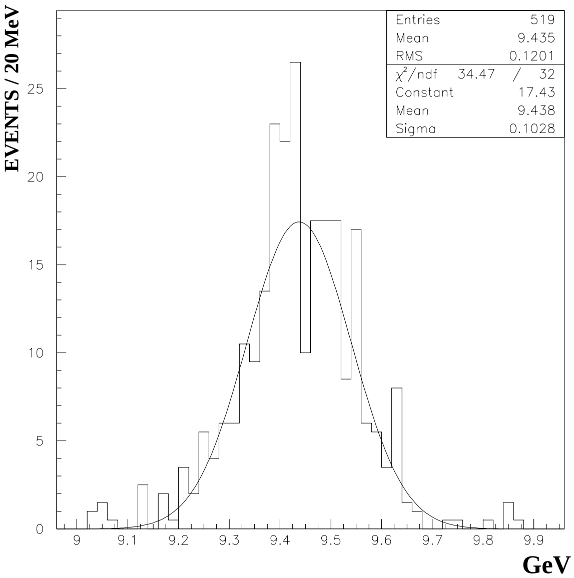

Figure 5.4: *Invariant mass distribution of reconstructed muon pairs from* Υ *decays.*

The cross sections for Υ production are taken from the measurements of the E605 experiment ($\sqrt{s} \simeq 38.8$ GeV) [37]:

$$\begin{gathered}
\mathrm{Br}\left.\frac{d\sigma}{dy}\right|_{y=0}(\Upsilon(1S)+\Upsilon(2S)+\Upsilon(3S)) = 2.31 \text{ pb/nucleon}; \\
\frac{\mathrm{Br}\frac{d\sigma}{dy}(\Upsilon(2S))}{\mathrm{Br}\frac{d\sigma}{dy}(\Upsilon(1S))} = 0.31; \qquad \frac{\mathrm{Br}\frac{d\sigma}{dy}(\Upsilon(3S))}{\mathrm{Br}\frac{d\sigma}{dy}(\Upsilon(1S))} = 0.09.
\end{gathered} \tag{5.1}$$

This experiment gives the lowest lying value for the Υ production cross section, about 130 pb/nucleon for $\sigma(\Upsilon(1S)+\Upsilon(2S)+\Upsilon(3S))$.

Figure 5.5 shows the $\Upsilon \to \mu^+\mu^-$ mass distributions on top of the background spectrum due to Drell-Yan pair production expected in one year (10^7sec) of HERA-B running at 40 MHz interaction rate. About 10000 fully reconstructed Υ decays are expected per year. The background is largely dominated by the Drell-Yan process. It is simulated by the PYTHIA generator based on the leading order cross section and scaled by a K factor of 2.3 [37]. As can be seen from Fig. 5.5, the predicted mass resolution of about 1% and a signal to background ratio $S/B \simeq 1.3$ (in a $\pm 2\sigma$ mass window

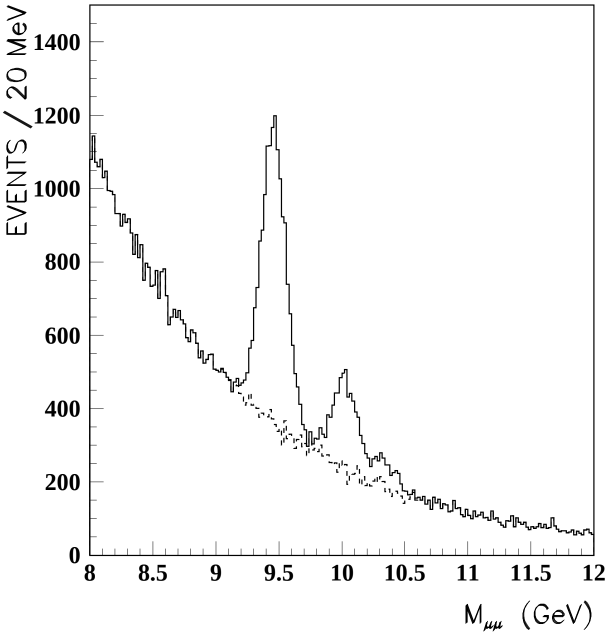

Figure 5.5: *$\mu^+\mu^-$ mass distribution in one year of nominal running of HERA-B.*

around the $\Upsilon(1S)$ peak) allow to observe clearly the Υ mass peaks above the background and to separate the $\Upsilon(1S)$ and $\Upsilon(2S)$ contributions.

5.2 Υ polarization

Apart from the study of the cross section, the polarization of the Υ provides an important test of the dynamics of the production process (see Section 1.2). The HERA-*B* detector is well suited to perform accurate Υ polarization measurements for the following reasons:

- HERA-*B* has a large acceptance (polar angle coverage in the laboratory frame from 10 mrad up to 250 mrad), corresponding to about 90% of the full solid angle in the CMS frame.
- The tracking system provides good momentum and mass resolution which allows to separate the $\Upsilon(nS)$ states.
- The experiment can accumulate high statistics due to the steady running at high interaction rates.

The polarization can be measured through the distribution of the decay angle θ in the Υ rest frame with respect to the boost direction (see Eq.(5.2)). Therefore, the Υ reconstruction efficiency as a function of decay angle has been studied. Figure 5.6 shows the acceptance for Υ events as a function of the cosine of the polar angle between the momentum of the positive muon and the beam direction in the rest frame of the Υ meson. The acceptance is constant and close to unity almost in the full range of $\cos\theta$. Large acceptance corrections are expected only for $|\cos\theta| > 0.8$.

The accuracy of the polarization measurement is estimated by simulating various initial polarizations for Υ mesons and Drell-Yan pairs with various signal to background ratios. After corrections for the acceptance the resulting angular distributions are fit with the function

$$\frac{dN}{d\cos\theta} = S(1 + \eta\cos^2\theta) + B(1 + \eta'\cos^2\theta). \tag{5.2}$$

Here S and B are signal and background normalization factors and η and η' determine the angular distributions, hence the polarizations, for signal and background. This procedure allows to extract the polarization not only for Υ mesons but also for the Drell-Yan pair continuum, an interesting issue by itself. Assuming that Drell-Yan polarization and signal to background ratio can be precisely measured in the HERA-*B* experiment, the number of free

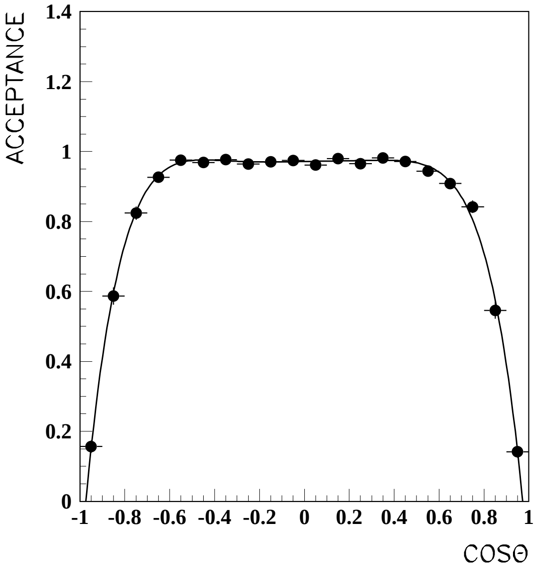

Figure 5.6: *Acceptance for the* $\Upsilon \to \mu^+\mu^-$ *decays as function of the cosine of the CMS polar angle.*

parameters in the fit function is reduced to 2. Results on the parameter η obtained from the fit to different simulated data samples of 10000 reconstructed Υ events are shown in Table 5.1.

Input polarization	S/B=1.3		S/B=1	S/B=2
η	$\eta' = 0$	$\eta' = 1$	$\eta' = 1$	
$\eta = 0.25$	0.21 ± 0.08	0.21 ± 0.08	0.22 ± 0.09	0.23 ± 0.08
$\eta = 0.5$	0.52 ± 0.10	0.48 ± 0.09	0.51 ± 0.09	0.54 ± 0.09
$\eta = 1$	0.91 ± 0.12	0.96 ± 0.11	0.96 ± 0.12	0.98 ± 0.10

Table 5.1: *Parameter* η *obtained from the fit for different input polarizations used in the simulation.*

As can be seen, the expected statistical error in η is largely dominated by the Υ statistics rather than by the value of the background polarization and the signal to background ratio. Figure 5.7 illustrates the statistical error $\delta\eta$ as a function of the number of reconstructed Υ events for various polarization parameters.. As can be seen, an accuracy $\delta\eta \simeq 0.08$ for $\eta = 0.25$ can be achieved for one year of HERA-*B* running. The expected error will allow to

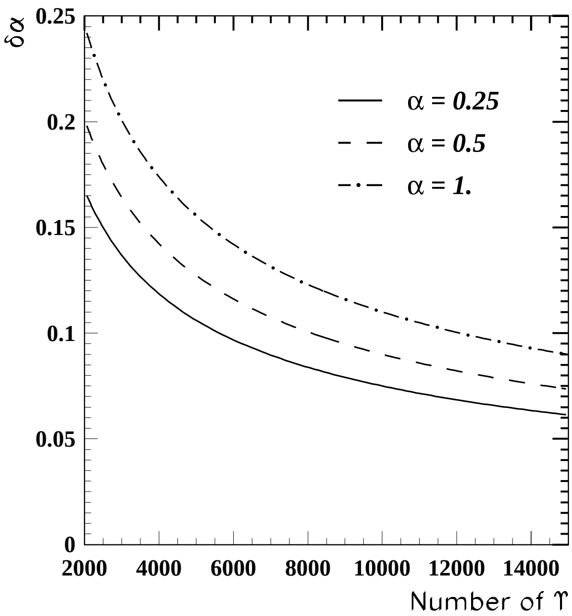

Figure 5.7: *Attainable accuracy in η for η =0.25, 0.5 and 1 as function of the number of reconstructed Υ decays.*

distinguish between $\eta = 0$ (CEM) and $\eta \simeq 0.24 - 0.3$ (NRQCD FA) with a significance of three standard deviations.

5.3 Conclusion

The Monte Carlo simulation shows that the Υ meson analysis is a viable physics topic for the early running phase of HERA-B. The predicted Υ mass resolution will allow to observe clearly the Υ mass peak above the background and to separate the $\Upsilon(1S)$ and $\Upsilon(2S)$ states. The expected statistical error for the measurement of the polarization parameter η is about 0.08 for $\eta \simeq 0.25$ for one year of running of the HERA-B experiment. The simulation was performed for the $\mu^+\mu^-$ decay channel which expected to be clearer than the e^+e^- decay channel. Nevertheless, a gain in statistics of $1.5 - 2$ is expected if the e^+e^- channel is included. The simulation conservatively assumed the lowest value for the Υ production cross section measured in different experiments [36, 37, 39] at $\sqrt{s} \simeq 38.8$ GeV which corresponds to a proton beam momentum of 800 GeV/c.

Conclusion

The aim of this thesis was to demonstrate the possibility to investigate hard proton-nucleus interactions and heavy flavour production at HERA-B. Two problems were considered:

1. Measurement of the inclusive π^0 production cross section.
2. Study of hadronic production of dileptons in the high-mass region and the prospects of Υ polarization measurements at HERA-B.

In this thesis, special emphasis was put on the study of various approaches for the luminosity determination, which is essential for the cross section measurements.

For the interaction rate determination the ECAL Energy Sum method was proposed. It was shown that this method provides a high accuracy in the luminosity determination and, at the same time, is easy to operate. For calibration of this method, only one constant, the average energy deposition in single interactions, is needed. Due to the large acceptance of the calorimeter, only a small correction of reconstruction efficiency has to be obtained from Monte Carlo simulations. All other ingredients are determined from tha data itself.

In an alternative approach, the interaction rate measurement was performed by counting reconstructed tracks in the Vertex Detector System. The interaction rate obtained from this method confirmed the results obtained by the ECAL method. However, the requirements on the determination of the track reconstruction efficiency makes the interaction rate measurement with the help of the VDS tracks a rather complex task.

For the determination of the interaction rate sharing among simultaneously inserted wires, counting of reconstructed primary vertices was studied. It was demonstrated that this method can serve as a direct check of the measurements provided by charge integrators.

It was shown that in the early phase of the HERA-B detector commissioning, using a limited part of its potential capabilities, the investigation of the production of inclusive high-p_T π^0 mesons could be successfully carried out. Such measurements provide important QCD tests. The inclusive π^0 production cross section was determined using the information from the inner part of the electromagnetic calorimeter for two types of target material, carbon and titanium, in the transverse momentum range of $2.75 < p_T < 5.0$ GeV/c and the center of mass rapidity range of $-0.05 < y_{C.M.} < 0.55$. The obtained value for the cross section agrees within errors with the cross section measured by the Fermilab E706 experiment for 800 GeV proton-beryllium interactions.

Comparing carbon and titanium cross sections, the nuclear mass number dependence could be determined, assuming a power law dependence $\sim A^\alpha$. The exponent α was measured to be $0.95 \pm 0.01 \pm 0.14$ for the transverse momentum range of the π^0 mesons of $2.75 < p_T < 5.0$ GeV/c.

The second part of this thesis concentrated on the study of physics prospects for heavy quarkonium production at HERA-B.

The feasibility to study hadronic production of dileptons in the high-mass region was investigated with a Monte Carlo simulation. It was shown that the predicted Υ mass resolution will allow the clear observation of the Υ mass peak above the background, and to separate the $\Upsilon(1S)$ and $\Upsilon(2S)$ states.

Special attention was paid to the investigation of the possibility to perform an accurate measurement of Υ polarization. This measurement provides an excellent opportunity to test different mechanisms of heavy quarkonium production. It was shown that the expected statistical error for the measurement of the polarization parameter α in one year of running at the HERA-B experiment will allow to distinguish between the color evaporation model ($\alpha = 0$) and the non-relativistic QCD factorization approach ($\alpha \simeq 0.24 - 0.3$) with a 3σ significance. The simulation was done only for the $\mu^+\mu^-$ decay channel. A gain in statistics of a factor of $1.5 - 2$ is expected if the e^+e^- channel is included.

Bibliography

[1] L. Apanasevich et al., Phys. Rev. D59 (1999)

[2] M. Beneke and I.Z. Rothstein, Phys. Rev. D54 (1996) 2005.

[3] M. Beneke, (1997), hep-ph/9703429.

[4] E. Braaten, B.A. Kniehl and J. Lee, Phys. Rev. D62 (2000)

[5] H.L. Lai et al., Phys. Rev. D51 (1995) 4763.

[6] J. Ivarsson, P. Kreuzer and T. Lohse, HERA-*B* Note 99-067 (1999).

[7] FERMILAB-E706, G. Alverson et al., Phys. Rev. D48 (1993) 5.

[8] A. Kharchilava, T. Lohse, A. Somov and A. Tkabladze, Phys. Rev. D59 (1999)

[9] R.P. Feynman, Phys. Rev. Lett. 23 (1969) 1415.

[10] R.P. Feynman, Usp. Fiz. Nauk 119 (1976) 689.

[11] J.D. Bjorken and E.A. Paschos, Phys. Rev. 185 (1969) 1975.

[12] E.L. Berger and D. Jones, Phys. Rev. D23 (1981) 1521.

[13] R. Baier and R. Ruckl, Phys. Lett. B102 (1981) 364.

[14] CDF, F. Abe et al., Phys. Rev. Lett. 69 (1992) 3704.

[15] CDF, F. Abe et al., Phys. Rev. Lett. 71 (1993) 2537.

[16] M. Beneke and M. Kramer, Phys. Rev. D55 (1997) 5269.

[17] G.T. Bodwin, E. Braaten and G.P. Lepage, Phys. Rev. D51 (1995) 1125.

[18] G.P. Lepage, L. Magnea, C. Nakhleh, U. Magnea and K. Hornbostel, Phys. Rev. D46 (1992) 4052.

[19] M.L. Mangano and A. Petrelli, Int. J. Mod. Phys. A12 (1997) 3887.

[20] M. Beneke, (1996), hep-ph/9605462.

[21] P. Ernstrom, L. Lonnblad and M. Vanttinen, Z. Phys. C76 (1997) 515.

[22] M. Beneke, I. Rothstein and M.B. Wise, Phys. Lett. B408 (1997) 373.

[23] M. Vanttinen, P. Hoyer, S.J. Brodsky and W.K. Tang, Phys. Rev. D51 (1995) 3332.

[24] E. Braaten and S. Fleming, Phys. Rev. Lett. 74 (1995) 3327.

[25] P. Cho and A.K. Leibovich, Phys. Rev. D53 (1996) 6203.

[26] P. Cho and A.K. Leibovich, Phys. Rev. D53 (1996) 150.

[27] S. Gupta and K. Sridhar, Phys. Rev. D54 (1996) 5545.

[28] W.K. Tang and M. Vanttinen, Phys. Rev. D54 (1996) 4349.

[29] L. Slepchenko and A. Tkabladze, (1996), hep-ph/9608296.

[30] M. Cacciari and M. Kramer, Phys. Rev. Lett. 76 (1996) 4128.

[31] A. Edin, G. Ingelman and J. Rathsman, Phys. Rev. D56 (1997) 7317.

[32] H. Fritzsch, Phys. Lett. B67 (1977) 217.

[33] F. Halzen, Phys. Lett. B69 (1977) 105.

[34] E.J. Eichten and C. Quigg, Phys. Rev. D52 (1995) 1726.

[35] M. Gluck, E. Reya and A. Vogt, Z. Phys. C67 (1995) 433.

[36] D.M. Alde et al., Phys. Rev. Lett. 66 (1991) 2285.

[37] T. Yoshida et al., Phys. Rev. D39 (1989) 3516.

[38] G. Moreno et al., Phys. Rev. D43 (1991) 2815.

[39] E771, T. Alexopoulos et al., Phys. Lett. B374 (1996) 271.

[40] M. Beneke and I.Z. Rothstein, Phys. Lett. B372 (1996) 157.

[41] W.K. Tang and M. Vanttinen, Phys. Rev. D54 (1996) 4349.

[42] E. Braaten and Y.Q. Chen, Phys. Rev. D54 (1996) 3216.

[43] S. Gupta, Phys. Rev. D58 (1998) 034006.

[44] A. Tkabladze, Phys. Lett. B462 (1999) 319.

[45] R.L. Jaffe and D. Kharzeev, Phys. Lett. B455 (1999) 306.

[46] T. Lohse et al., DESY-PRC 94/02 (1994).

[47] R. Mankel, HERA-*B* Note 98-079 (1998).

[48] T. Fuljahn et al., IEEE Trans. Nucl. Sci. 45 (1998) 1782.

[49] T. Sjostrand, Comput. Phys. Commun. 82 (1994) 74.

[50] H. Pi, Comput. Phys. Commun. 71 (1992) 173.

[51] S. Nowak, HERA-*B* Note 94-123 (1994).

[52] A.S. Carroll et al., Phys. Lett. B80 (1979) 319.

[53] M. Villa, HERA-*B* Note 97-135 (1997).

[54] I. Kisel and S. Masiocchi, HERA-*B* Note 99-242 (1999).

[55] K. Ehret et al., (2000), hep-ex/0002002.

[56] I. Kisel, private communications.

[57] . http://www-hera-b.desy.de/subgroup/detector/target.

[58] D. Emelianov, I. Kisel, S. Masciocchi and Y. Vassiliev, HERA-*B* Note to be published .

[59] S. Shuvalov, private communications.

[60] A. Zoccoli, HERA-*B* Note 00-129 (2000).

[61] E. Gerndt and G. Wagner, private communications.

[62] A. Somov, In: *QCD and early Physics Meeting* Apr 30th (1999) Part 1.

[63] M. Villa, private communications.

[64] Fermilab E706, L. Apanasevich et al., Phys. Rev. Lett. 81 (1998) 2642.

[65] L. Kluberg et al., Phys. Rev. Lett. 38 (1977) 670.

[66] I. Arinyo, R. Mankel and A. Somov, HERA-B Note 98-132 (1998).

[67] J. Ivarsson and A. Somov, HERA-B Note 97-166 (1997).

[68] H. Albrecht, HERA-B Note 95-065 (1995).

Lebenslauf

Somov Alexandre

Geburtsdatum:	17.06.1969
Geburtsort:	Moskau

Ausbildung

1986 - 1994 – Physikalisch Technisches Institut in Moskau,Russland. Fachbereich für allgemeine und angewandte Physik. Diplomarbeit über das Thema : ”Aufbau und Erprobung des Lambda-3 zentralen Spurdetektors”(Abschluss mit Auszeichnung).

(1987 - 1989) – Wehrdienst.

1994 - – Wissenschaftlicher Mitarbeiter am Institut für Theoretische und Experimentelle Physik (ITEP), Moskau.

1993 - 1995 – Teilnahme am “Lambda-3” Experiment (ITEP). Untersuchung der Hyperon Produktion in Proton-Nukleon Wechselwirkung.

1995 - 1997 – Teilnahme am FOPI Experiment (GSI, Darmstadt)

1997 - 2000 – Graduiertenkolleg ”Strukturuntersuchungen, Präzisionstests und Erweiterungen des Standardmodells der Elementarteilchenphysik ”an der Humboldt universität zu Berlin.
Doktorandenstipendiat am Experiment HERA-B, DESY.

Selbständigkeitserklärung

Hiermit erkläre ich, daß ich diese Arbeit selbständig verfaßt habe und keine anderen als die angegebenen Quellen und Hilfsmittel benutzt habe.

Alexandre Somov
26. Juli 2000